Department of Precision and Microsystems Engineering

Fabrication of Flexible 3D Printed Vascular Phantoms: Investigating the Impact of Variable Stiffness for Diameter Change under Flow Conditions

Lucas Zijlstra

Report no.	: 2026.047
Supervisor 1	: Paola Fanzio
Supervisor 2	: Marcel Tichem
Specialisation	: High-Tech Engineering
Type of report	: Master Thesis
Date	: June 2026

TU Delft Delft University of Technology

Challenge the future

Fabrication of Flexible 3D Printed Vascular Phantoms

Investigating the Impact of Variable Stiffness for Diameter Change under Flow Conditions

by

Lucas Zijlstra

Supervisor 1:	P. Fanzio
Supervisor 2:	M. Tichem
Faculty:	Faculty of Mechanical Engineering
Department:	Precision and Microsystems Engineering

Delft University of Technology
June 2026

Acknowledgements

This thesis marks the end of an important and rewarding year. Looking back, I am grateful that this project allowed me to combine research with practical work in the lab. The project was not only theoretical, but also involved designing, fabricating, testing, and improving physical samples. This practical aspect suited me well and made the thesis both challenging and enjoyable.

First, I would like to thank my supervisor Paola Fanzio for her guidance throughout the entire project. Even though I did not have a daily supervisor, I always felt that I could ask for help when needed. Each meeting helped me to take the next step, whether that was by discussing experimental problems, improving the structure of the research, or deciding how to continue after unexpected results. I am very grateful for the freedom I received during the project, while still having support whenever it was necessary.

I would also like to thank Marcel Tichem for his involvement as second professor. Although his schedule was often busy, his feedback helped me to look at the project from a broader perspective. His questions and suggestions helped me to keep the overall direction of the thesis clear and prevented the work from becoming too scattered. The combination of Paola and Marcel as supervisors created a very pleasant and open atmosphere during the meetings, which made the process more enjoyable.

Furthermore, I would like to thank Stavros and Ahmed for their help with the 3D printer and the practical aspects of the fabrication process. I also want to thank Zhilin for helping me with the pressure-flow experiments and for thinking along when experimental challenges appeared. I am grateful to Selene and Pritesh for sharing their knowledge on vascular networks, vessel behaviour, and analytical modelling. Their insights helped me to better understand how the experimental work could be connected to the underlying vascular mechanics. I would also like to thank the lab technicians for their support and advice while working in the lab.

Finally, I want to thank my friends and fellow students for the many conversations, discussions, and moments of support throughout the year. Being able to talk about the project, exchange ideas, and sometimes simply take a break was very valuable. I am especially grateful to my family and girlfriend for their continuous support and encouragement during the entire thesis period.

Abstract

Vascular phantoms are artificial vessel models that provide controlled and repeatable environments for medical research, imaging validation, device testing, surgical planning, and training. To improve their physiological relevance, these phantoms should not only reproduce vascular geometry, but also show mechanical behaviour that is representative of blood vessels. In particular, small-scale compliant vascular phantoms should be able to deform under pressure-driven flow. However, fabricating small open channels from soft materials while maintaining geometrical accuracy, tunable stiffness, and measurable compliance remains challenging.

This thesis investigates the fabrication and experimental characterization of small-scale flexible vascular phantoms created using masked stereolithography 3D printing. Straight cylindrical channels were printed using Elastomer-X resin with different lumen diameters and wall thicknesses to determine a printable geometry range. The geometrical accuracy of the printed channels was evaluated using microscopy, while the internal lumen geometry was further inspected using ink-filled channels. Tensile tests were performed to determine the Young's modulus of the printed material under different exposure and post-curing conditions. By varying the printer exposure time and UV post-curing duration, different stiffness configurations were obtained.

The pressure-flow behaviour of the printed channels was investigated using water as the working fluid. Baseline measurements were used to correct for pressure losses in the setup, after which the channel-only hydraulic resistance was calculated. The effective diameter was then estimated from the hydraulic resistance using the Hagen–Poiseuille relation. The results showed that a lumen diameter of 0.7 mm with a wall thickness of 0.25 mm could be printed as the smallest consistently open channel suitable for flow experiments. Tensile testing showed that the Young's modulus could be tuned between approximately 1.05 and 1.25 MPa by changing the fabrication conditions. Pressure-flow measurements showed a decrease in hydraulic resistance with increasing mean pressure for several channels, corresponding to an increase in effective diameter. The softer channels generally showed a larger relative effective diameter increase than the slightly stiffer channels.

These results demonstrate that masked stereolithography can be used to fabricate small-scale flexible vascular phantoms with tunable stiffness and measurable pressure-dependent behaviour. Although the effective diameter was determined indirectly and uncertainties remain due to local lumen narrowing, measurement noise, and baseline correction, the study provides an important experimental validation step towards compliant 3D printed vascular phantoms for pressure-flow applications.

Contents

Introduction

In recent years, medical phantoms have become increasingly important in biomedical engineering and medical research. These artificial models are designed to mimic the geometry and properties of human tissues or organs. They provide a controlled and repeatable environment for medical imaging validation, treatment planning, surgical training, device testing, and experimental research. An important advantage is that phantoms can reduce the reliance on animal models and in vivo experiments, while still providing realistic and repeatable conditions for research and clinical training [1, 2].

The importance of phantoms spans multiple areas of modern healthcare. They are especially relevant in fields where accurate diagnosis, treatment planning, and device validation are essential [3, 4]. In oncology, phantoms are used for radiotherapy dose verification and treatment planning [1]. In neurology, they support imaging validation and quality assurance across imaging techniques such as CT, MRI, ultrasound, PET, and SPECT [5]. In cardiology and vascular medicine, vascular phantoms can be used to study blood-flow behaviour, test medical devices, and train procedures such as catheter navigation and stent placement [2, 6]. By replicating anatomical structures and functional behaviour, phantoms help to improve the reliability of imaging, the safety of interventions, and the development of new medical devices.

Traditional phantom manufacturing methods, such as moulding and casting, have been used for many years, but these methods can be limited in terms of geometric complexity, cost, repeatability, and patient-specific design [5]. Additive Manufacturing (AM), better known as three-dimensional (3D) printing, offers an attractive alternative because it enables the fabrication of complex and customized geometries with relatively short production times. This is particularly useful for vascular applications, where small channels, branching structures, and local changes in vessel diameter are important [2, 3, 4]. Recent studies have shown that 3D printing can be used to fabricate vascular phantoms for applications such as imaging, surgical planning, device testing, and endovascular training [7, 6].

Vascular phantoms are a specific class of medical phantoms that aim to replicate blood vessels. These models are especially valuable because cardiovascular diseases are the leading cause of death globally, making realistic vascular models important for research, training, and device development [8, 9]. Blood vessels are not rigid tubes; they expand and deform under pressure. Therefore, a realistic vascular phantom should not only reproduce the vessel geometry, but should also have relevant mechanical properties. For pressure-flow applications, this means that the channel should be compliant enough to show a measurable diameter change under internal pressure [10, 11].

This thesis report is structured as follows. First, the literature review gives a broad overview of different medical phantoms, with a focus on vascular phantoms, their requirements, anatomical accuracy, mechanical properties, functional validation, and manufacturing techniques. Based on this review, the research gap and research question are defined. After this, the research paper presents the experimental work of this thesis, including the approach, theoretical background, materials and methods, results and discussion, and conclusion. Finally, the appendices provide additional experimental data, validation figures, and MATLAB code used for the analysis.

Literature Review

1. Overview of Organ-Specific Medical Phantoms

Phantoms are developed to replicate various aspects of the human body, ranging from individual tissues to complex organ systems. In medical research and training, organ-specific phantoms are particularly interesting because organs often present unique anatomical, mechanical, and imaging characteristics that are essential for accurate mimicking. Focusing on organs rather than more generic body parts is valuable, since they are often the sites of diagnosis, intervention, and therapy, and therefore require realistic surrogates for planning, validation, and training.

The main applications of organ-specific phantoms can be summarized as follows:

- **Radiation dosimetry for specific organs**: enabling dose verification and calibration for radiotherapy [1, 2].
- **Development and optimization of medical imaging systems** (CT, MRI, PET, SPECT, ultrasound): supporting Quality Assurance (QA) and scanner calibration [5, 12].
- **Verification of treatment planning**: patient-specific phantoms allow testing of radiotherapy planning systems under realistic conditions [2].
- **Fundamental studies of organ behavior**: for example, investigating lung motion effects or simulating pathological conditions such as tumors and lesions [13, 14].
- **Training and education**: providing safe platforms for students, clinicians, and surgeons to practice procedures [15].
- **Development and testing of medical devices**: phantoms are used for implantable or invasive devices, such as stents, catheters, or biopsy needles [6, 16].

This section first discusses several types of organ phantoms and highlights their main advantages and challenges. This is followed by a comparison table that provides a clear overview of their characteristics. After this general overview, a dedicated subsection focuses on vascular phantoms, discussing their challenges and requirements as well as their geometry, mechanical properties, and validation.

(a) Brain phantom (b) Lung phantom (c) Breast phantom

(d) Liver phantom (e) Vascular phantom (f) Cardiac phantom

Figure 1: Examples of some organ phantoms used in medicine: (a) Brain phantom [17], (b) Lung phantom [13], (c) Breast phantom [18], (d) Liver phantom [14], (e) Vascular phantoms [15], (f) Cardiac phantom [16].

1.1. Organ-Specific Phantoms

A wide variety of organ-specific phantoms have been developed to replicate the anatomical complexity and functional behavior of critical human organs. Organs such as the brain, lungs, breast, liver, vascular system, and heart have received particular attention,

since they are frequent targets of diagnostic imaging and interventional procedures and therefore require highly realistic surrogates [4, 16, 13, 18, 14, 15]. Each organ presents distinct challenges, for example, the brain with its layered gray and white matter [17] and the lungs with their porous structure and breathing motion [13]. Illustrative examples of representative organ phantoms are provided in Figure 1, which summarizes the diversity of designs.

1.1.1. Brain Phantoms

Brain phantoms are widely used in MRI, ultrasound, and PET to evaluate imaging sequences, study tumor detection, and test neurovascular interventions. A recent prototype, developed by Altermatt et al. [17], reproduced the complex folding of white matter (WM), the main bundles of nerve fibers responsible for brain communication, and gray matter (GM), which contains most neuron cell bodies, using 3D printed molds in combination with manganese chloride-doped agar gels ($MnCl_2$), successfully replicating T1 relaxation times, which is an MRI property that determines image contrast between tissues, observed in vivo. The layered casting method also preserved the characteristic folds of the brain surface, the ridges (gyri) and grooves (sulci), resulting in anatomically accurate phantoms with WM/GM contrast similar to healthy controls. An example of such a model is shown in Figure 1a, where WM and GM gels were assembled and scanned to replicate realistic brain tissue contrast.

Advantages: Brain phantoms enable safe and reproducible validation of MRI pulse sequences, image processing algorithms, and surgical approaches for tumor removal or electrode placement. They are particularly useful in training neurosurgeons where direct patient practice is not feasible.

Challenges: Despite advances, it remains difficult to reproduce the viscoelastic (exhibit both viscous (fluid-like) and elastic (solid-like) properties when deformed) and anisotropic (having a different value when measured in different directions) mechanical properties of brain tissue. Most models degrade within days or weeks due to diffusion of contrast agents, and mechanical properties such as compliance and softness do not fully match real brain tissue [17].

1.1.2. Lung Phantoms

Lung phantoms have been developed primarily for CT and radiotherapy applications, where anthropomorphic thoracic models can mimic lung parenchyma (the functional tissue of the lung), pulmonary nodules (small abnormal growths), and surrounding vessels. For example, Kinnard et al. showed that an anthropomorphic phantom was used to assess the accuracy of CT volume measurements of lung nodules, showing that nodules attached to blood vessels often lead to underestimation of volume in clinical workflows [13]. Variable-density 3D printing and tissue-mimicking polymers have been used to replicate the heterogeneous structure of lung tissue, enabling better calibration of imaging systems. Figure 1b shows a CT image of a lung phantom, illustrating how such models can reproduce anatomical detail and imaging contrast comparable to human lung tissue.

Advantages: Such phantoms allow precise testing of imaging algorithms, dose verification in radiotherapy, and CT calibration. They are also essential for evaluating detection limits of nodules and ground-glass opacities, which are hazy spots on CT scans that indicate partial filling of air spaces and may signal early disease.

Challenges: A major limitation is the difficulty of reproducing the dynamic breathing motion of lungs. Current static phantoms cannot fully replicate breathing mechanics, which reduces their clinical realism for interventional training.

1.1.3. Breast Phantoms

Breast phantoms are primarily developed for mammography, MRI, and ultrasound in the context of breast cancer detection and screening. A recent approach matched physical breast phantoms with virtual models derived from human subject data, reproducing both glandular tissues (which produce milk and appear dense on imaging) and adipose tissues (fatty tissues that appear less dense) in realistic proportions [18]. These phantoms enable standardized evaluation of imaging modalities and support the development of advanced detection algorithms. An example is shown in Figure 1c, where a breast phantom mold was filled with transparent resin to replicate heterogeneous internal structures for imaging validation.

Advantages: Breast phantoms provide reproducible platforms for comparing imaging modalities, evaluating radiation dose in mammography, and training radiologists in lesion detection.

Challenges: The main challenge is reproducing the highly heterogeneous and deformable nature of breast tissue. Most phantoms use uniform materials and cannot fully mimic compressibility or density variations across the breast.

1.1.4. Liver Phantoms

Liver phantoms are widely used in ultrasound-guided interventions, biopsy training (the removal of tissue from a living body), and thermal ablation tests. Mechanical property studies of liver tissues have shown that realistic replication requires mimicking the nonlinear elastic behavior of the liver and the heterogeneous stiffness in the lobes [14]. Materials such as silicone, polyvinyl alcohol (PVA), and hydrogels have been used to manufacture liver-mimicking phantoms with acoustic properties suitable for ultrasound

imaging. As shown in Figure 1d, liver phantoms can reproduce the external morphology of the organ, here represented by the front surface of a silicone-based model.

Advantages: They provide realistic ultrasound imaging feedback, allow training for needle insertions, and are valuable for training interventional radiologists.

Challenges: Many phantoms fail to achieve the precise viscoelastic response of liver tissue, leading to inaccurate feedback on the forces experienced during biopsy needle insertion. Durability is also limited, as repeated punctures degrade the material structure [14].

1.1.5. Vascular Phantoms

Vascular phantoms are among the most widely used phantoms due to their importance in imaging (CT angiography (CTA), Doppler ultrasound) and in interventional training. Coles-Black et al. demonstrated that 3D-printed patient-specific phantoms (3DPSP) of abdominal aortic aneurysms (AAA) allow simulation of fenestrated endovascular aneurysm repair (FEVAR), device deployment, and surgical planning under fluoroscopy [15]. These phantoms were fabricated using 3D printing or casting, with flexible materials that enable realistic flow simulation. Figure 1e shows a flexible, hollow, translucent AAA phantom.

Advantages: Vascular phantoms enable preoperative simulation of complex interventions, flow visualization, and training in stent and catheter placement. They also improve patient education and surgical team preparedness.

Challenges: Reproducing the compliance, anisotropy, and nonlinear elastic properties of vessel walls remains a challenge. Many phantoms exhibit unrealistic stiffness, limiting their ability to replicate physiological hemodynamics.

1.1.6. Cardiac Phantoms

Cardiac phantoms replicate the heart chambers, valves, and coronary arteries for imaging validation and procedural planning. A systematic review showed that 3D-printed cardiovascular phantoms are highly accurate for CT and MRI, and increasingly applied to simulate valve replacement, left atrial appendage (LAA) occlusion, and congenital defect repair (structural abnormalities present at birth) [16]. With the use of 3D printing, multimaterial models with elastic regions for valve mechanics are enabled. As illustrated in Figure 1f, a cardiac phantom can reproduce structures such as the left atrium and aortic root, including mitral annular calcification (disease that can cause heart failure).

Advantages: These phantoms enable realistic simulation of hemodynamics, provide valuable training for cardiac surgery, and support the development and testing of equipment.

Challenges: Key challenges include replicating myocardial contractility (the active pumping of heart muscle) and dynamic valve motion. Material limitations often lead to static models that cannot reproduce the cyclical beating of the heart.

1.1.7. Comparison of Different Phantoms

Table 1: Comparison of organ phantoms in terms of geometry, materials, resolution, and key properties.

Phantom Type	**Geometry**	**Common Materials**	**Resolution**	**Key Properties**	**Articles**
Brain	Complex folds, layered WM/GM structures	Hydrogels, silicone, agar gels	0.5–1 mm	MRI relaxation accuracy, limited mechanical realism	[17], [4]
Lung	Large volume, porous parenchyma, nodules	Thermoplastics (PLA, ABS), foamed polymers	Sub-mm to 1 mm; nodules 3–10 mm	HU accuracy, density gradients, limited breathing motion replication	[13], [3]
Breast	Heterogeneous glandular /adipose mix; simple outer shape	Silicone, polyurethane, gels	0.2–0.5 mm	X-ray attenuation, compressibility, ultrasound visibility	[18], [4]
Liver	Solid organ, smooth surface	Hydrogels (PVA, gelatin), silicone	~1 mm	Ultrasound echogenicity, biopsy needle feedback, elastic mismatch	[14], [19]
Vascular	Hollow thin-walled tubes, bifurcations, aneurysms	Silicone, hydrogels, elastic resins, PVA (sacrificial)	Wall thickness 50–300 μm; lumen mm-scale	Compliance, flow fidelity, multimodal imaging compatibility	[15], [20], [21]
Cardiac	Chambers, valves, coronaries	Silicone, elastic resins, multi-material blends	50–500 μm	Coronary fidelity, hemodynamics, lacks contractility	[16], [2], [22]

Table 1 provides an overview of the main organ-specific phantoms reported in the literature, highlighting their geometry, commonly used materials, achievable resolution, and key properties or requirements. This comparison illustrates how the design of phantoms strongly depends on the anatomical and functional characteristics of each organ system.

It becomes clear that vascular and cardiac phantoms demand the highest spatial accuracy and mechanical fidelity, particularly to replicate thin vessel walls and dynamic hemodynamics. Vascular phantoms are especially interesting because they combine the need for compliant, thin walls with complex branching networks, where fabricating hollow, tortuous structures without introducing surface roughness at high resolution remains particularly challenging, making them one of the most difficult phantom types to produce compared to the more uniform structures of solid organs such as the liver or heart [15].

1.2. Vascular Phantoms

Building on this importance, vascular phantoms, also mentioned as vascular models, require high manufacturing resolution and realistic mechanical properties to reproduce flow and wall behavior.

In addition, vascular pathologies such as stenosis or aneurysms are among the most common targets for interventional radiology and surgical procedures [23]. Cardiovascular diseases affect over 600 million people worldwide and cause close to 20 million deaths annually, approximately one third of all global deaths a year, with the majority occurring in low- and middle-income countries [8, 9].

Beyond their devastating health impact, they also impose a massive economic burden, costing the European Union approximately €282 billion annually, with healthcare services and productivity losses being the largest contributors [24]. By improving clinician training, enabling safer device testing, and supporting patient-specific preoperative planning, vascular phantoms can reduce procedural complications, shorten surgery times, and accelerate medical innovation, thereby helping to lower both direct healthcare expenses and indirect societal costs.

This combination of technical challenges and health and economic relevance, makes vascular phantoms a particularly valuable and active research area [6, 20, 15, 16].

1.2.1. Challenges and Requirements

Effective vascular phantoms must balance several key requirements, each of which is associated with specific challenges [7]:

- **Anatomical accuracy:** Patient-specific phantoms must be anatomically accurate, to achieve this, segmentation from CTA or Magnetic Resonance Angiography (MRA) is required, which introduces challenges in image quality, resolution, and post-processing. Capturing the geometry of small vessels, bifurcations, and tortuous structures is particularly difficult under these conditions [16].
- **Mechanical realism:** Materials must provide sufficient elasticity to mimic arterial compliance and remain durable under repeated pulsatile flow. However, most available materials fail to replicate the nonlinear, viscoelastic response of arteries, limiting the physiological accuracy of wall deformation [25].
- **Perfusability:** A functional fluid circuit (with proper flow rates, resistance, and possibly pulsatility) is needed to replicate flow dynamics such as contrast filling or Doppler waveforms realistically. Achieving physiological pulsatile flow patterns, pressure levels, and fluid properties is complex, and mismatches can compromise both mechanical and imaging validation [26].
- **Imaging compatibility:** Since phantoms are often tested across CT, ultrasound, and MRI, materials should reproduce tissue-equivalent contrast (e.g., HU values in CT or acoustic impedance in ultrasound). In practice, no single material reproduces realistic contrast across all modalities, often resulting in image distortions or inaccurate parameter replication [5].
- **Durability and reproducibility:** Phantoms must withstand repeated testing and long exposure to flow while maintaining consistent performances, as mechanical degradation can alter flow conditions and reduce the reliability of the experimental data. In reality, many degrade over time, and the absence of standardized validation protocols further limits reproducibility and comparability [27].

In particular, the anatomical accuracy and mechanical properties of vascular phantoms are key aspects of their design and functionality. These will be explored further in the following subsections: Section 1.2.2 discusses the complexity of vascular phantom geometry, providing examples to highlight its significance for both experimental and clinical applications. Section 1.2.3 focuses on the key mechanical properties that make vascular phantoms effective in simulating real arterial behavior.

1.2.2. Anatomical accuracy

The anatomical accuracy, or in other words the geometry, of vascular phantoms plays an important role in their functionality. Figure 2 shows an example of a 3D printed patient-specific neurovascular phantom used to investigate mechanical thrombectomy procedures, in which a blood clot is physically removed from a blood vessel to restore blood flow. The figure highlights the complex arterial branching and tortuous vessel pathways, emphasizing the geometric challenges in replicating such anatomies for experimental validation of vascular techniques [7].

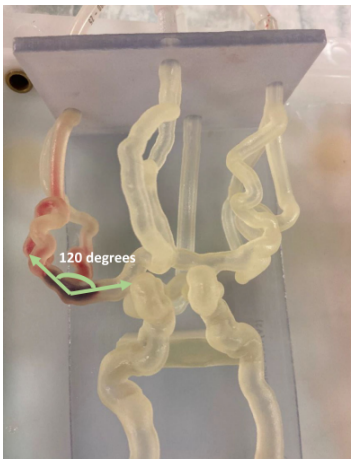

Figure 2: Patient-specific 3D printed neurovascular phantom illustrating complex arterial geometry for thrombectomy simulation [7].

Incorporating branching angles such as the 120° bifurcation shown in Figure 2 enhances the physiological relevance of vascular phantoms. Real vessels rarely follow straight paths, their curvature and bifurcations strongly influence flow behavior, shear stress distribution, and clot–device interaction during thrombectomy [7, 5]. Sommer et al. showed that branching angle was the only geometric feature that significantly affected thrombectomy outcome: sharper vessel angles made it more difficult for devices to capture and remove clots effectively [7]. Printing such geometries enables more realistic evaluation of medical devices, disease progression, and hemodynamic conditions compared to simple straight-tube models [20]. However, complex bifurcations also present manufacturing challenges, including surface roughness, removal of residual material, and preventing structural deformation, particularly at small diameters and sharp angles [5, 15]. Despite these limitations, angled vessel models are essential for replicating clinical scenarios and improving the translational value of in vitro experiments.

Capturing and replicating patient-specific vascular geometries, including those altered by conditions such as carotid stenosis, coronary artery disease, or aneurysms, enables the fabrication of phantoms that accurately model these pathologies, which are essential for studying disease mechanisms [20]. Key aspects of vascular geometries include lumen diameter, wall thickness, and bifurcations, which have a strong influence on hemodynamics. For example, Biglino et al. demonstrated that even small variations in lumen diameter and wall thickness significantly affect pressure and flow waveforms in aortic phantoms, directly impacting the physiological relevance of in-vitro experiments [28]. Similarly, Filippou et al. showed that accurate replication of bifurcation geometry was crucial for capturing realistic flow patterns in cerebral artery models, which in turn influenced clot migration and thrombectomy outcomes [5]. These studies highlight that high geometric accuracy, beyond overall shape, is critical for building phantoms that not only resemble real vasculature but also reproduce the mechanical and fluid dynamic conditions necessary for clinically meaningful research.

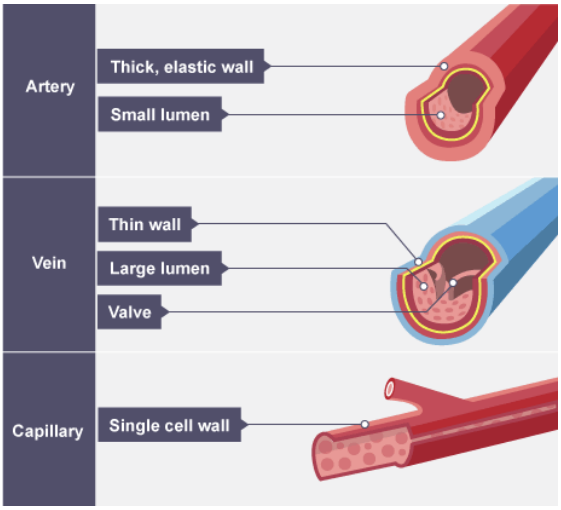

Figure 3: Blood is carried through three different types of blood vessels in the body: arteries, veins and capillaries [29].

Figure 3 illustrates that there are three different types of blood vessels in the human body, which are arteries, veins and capillaries. Capillaries are microscopically thin to allow gases and nutrients to exchange, the arteries are tough and flexible to cope with high pressure blood flow and the veins contain valves to prevent the blood from travelling backwards when at low pressure [29].

In this literature review, the focus is on arteries (and their smaller branches, arterioles), because (1) most vascular phantom studies emphasize arterial models (e.g. endovascular procedures, aneurysms, stents) rather than veins or capillaries [15, 30, 5, 6], (2) capillaries are extremely small (typically 5–10 μm in diameter), making them very challenging to fabricate in phantom form with current technologies [31, 32], and (3) arterial geometries and flows have direct relevance for cardiovascular disease and interventions, giving them greater clinical and research precedence [33, 34].

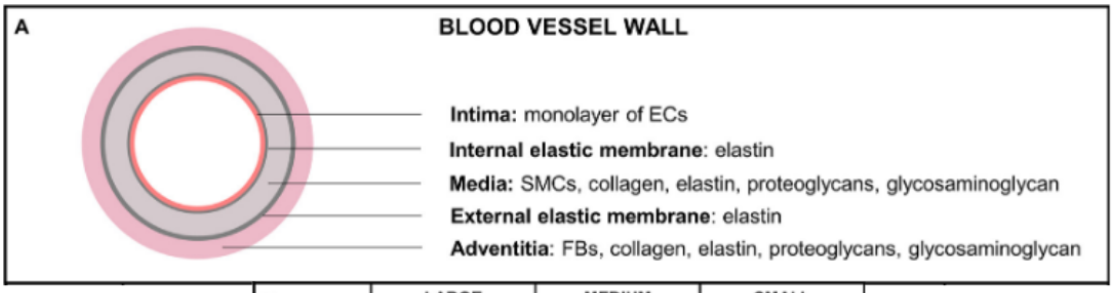

B	LARGE ARTERIES	MEDIUM ARTERIES	SMALL ARTERIES
			
Diameter (mm)	> 10	6 - 10	1 – 6
Wall Thickness (μm)	1500	1000	125 – 800
Total Length (mm)	400	8000	160000
Pressure (mmHg)*	100	100	90 – 95

Figure 4: Camasao et al. provide an overview of the structure and composition of blood vessel walls. A) The blood vessel wall is composed of three main layers: tunica intima (inner layer), tunica media (middle layer), and tunica adventitia (outer layer). Elastic membranes are found in their interfaces. B) The thickness and the composition of each layer vary according to the artery size and diameter [11]. *Normal pressure values for the systemic vascular system.

The classification of blood vessels into small, medium, and large categories is primarily based on their diameter, as illustrated in Figure 4. Large arteries typically have diameters greater than 10 mm, medium arteries range from 6–10 mm, and small arteries measure between 1–6 mm. However, when considering physiological vessel sizes in more detail, the smaller arteries in the human body, the arterioles, which control blood pressure and flow, are often significantly smaller, frequently falling into the submillimeter range, as low as 10–300 μm [35, 36]. Medium-sized arteries generally range from a few millimeters up to around 5 mm in diameter, while the largest arteries, such as the aorta, can reach diameters of 10–25 mm [35, 36].

The figure also highlights important structural differences between vessel types. Large arteries contain a thick middle layer rich in elastin, which provides elasticity to withstand pulsatile pressure. As vessel size decreases, the elastin content is reduced and the proportion of smooth muscle cells increases, enhancing the vessel's capacity to regulate blood flow [11].

1.2.3. Mechanical Properties

Unlike rigid organs, arteries exhibit complex mechanical behavior that must be replicated in vascular phantoms. They are anisotropic and viscoelastic, meaning that their response depends on direction, time, and loading history [11]. Key properties include:

- **Compliance:** The ability of the vessel wall to expand and recoil under pressure, which is essential for reproducing physiological flow and pressure waveforms [28]. Healthy arteries expand slightly each time the heart pumps blood. For every 100 mmHg increase in pressure, they grow about 1.5–2 % in size. Older or diseased arteries stretch less, meaning they are less compliant (stiffer) [11].
- **Elastic modulus and strain-stiffening:** Arteries show a nonlinear stress–strain response, with low stiffness at small deformations and progressive stiffening at higher strains. Healthy arteries typically exhibit a Young's modulus of ~0.2–1.0 MPa [11], increasing to ~1.5 MPa in atherosclerotic (a disease where plaque buildup on the inner walls of arteries) and up to

~3.8 MPa in severely diseased vessels [6]. This strain-stiffening behavior ensures flexibility at physiological pressures while preventing rupture under high loads.

- **Anisotropy:** The arterial wall is reinforced by collagen and elastin fibers that are directionally aligned, leading to different mechanical responses circumferentially and longitudinally [11, 37]. Circumferential tensile strength is typically higher, with reported values ranging from ~1.2–2.3 MPa for human carotid and femoral arteries [11].
- **Viscoelasticity:** Arterial tissue exhibits both elastic and time-dependent (viscous) behavior, which contributes to energy dissipation and damping of pressure waves [11, 37]. This viscoelastic nature results in hysteresis during loading–unloading cycles and supports the Windkessel effect, which smooths pulsatile flow into continuous perfusion [38].
- **Strength and durability (overall reliability):** Burst pressure and fatigue resistance define the vessel's ability to withstand repeated pulsatile loading without failure [6, 11].

Mechanical characterization of vascular phantoms should therefore focus on reproducing these physiological properties, typically measured through tests such as uniaxial or biaxial tension, pressure–diameter compliance curves, and burst pressure analysis [6]. Systematic protocols for comparing phantom mechanics with native arterial behavior are still lacking, representing an important gap in standardization [11].

1.2.4. Functional validation

Validation is crucial for vascular phantoms to ensure that both their geometry and mechanical properties translate into physiologically realistic flow behavior. Instead of relying on a single test, comprehensive validation can be divided into two complementary levels: (i) functional validation, which is directly linked to the intended use of vascular phantoms (Chapter 2), and (ii) manufacturing validation, which is rooted in the chosen fabrication methods and materials (Chapter 3). This division makes explicit how the application and the construction of vascular phantoms each demand their own assessment.

Functional validation focuses on whether the phantom performs as a physiological surrogate in flow experiments. Because vascular phantoms are primarily used to study hemodynamics and device interactions, flow testing is essential. Techniques such as particle image velocimetry (PIV) and ultrasound-based echoPIV allow visualization of velocity fields, flow separation, and vortex structures in aneurysm or stenosis models [39, 20]. For example, Mirgolbabaee et al. demonstrated that their abdominal aortic aneurysm phantom reproduced intraluminal velocity distributions consistent with in vivo data when tested with echoPIV [20]. Simplified fluidic circuits, such as Windkessel analogues and wall-less flow loops, further enable controlled assessment of pressure–flow relationships [38, 25]. These methods confirm whether the phantom can replicate the functional role for which it was designed: to provide realistic hemodynamic conditions for research, training, and device testing.

2. Manufacturing Vascular Phantoms

Vascular phantoms require fabrication strategies that achieve both high geometric precision and realistic wall properties. In this section, the most relevant techniques for vascular phantom research are described, focusing on their working principles, achievable resolution, most suitable materials, and advantages and limitations. Two main routes are commonly used: (1) direct 3D printing methods (PolyJet, Stereolithography, Fused Deposition Modeling (FDM), and micro-Digital Light Processing (mDLP)) and (2) sacrificial mold casting approaches (lost-core casting, dip-spin coating, and sacrificial templates), followed by a comparative overview that highlights the trade-offs between these strategies.

2.1. Direct 3D Printing Techniques

Direct 3D printing refers to the fabrication of vascular phantoms by printing the final geometry of the vessel itself, rather than creating a mold or core that will later be removed (as in indirect printing). This approach has become a prominent strategy for fabricating vascular phantoms because it combines high geometric precision with the possibility of tailoring wall thickness and lumen complexity. Among the wide range of additive manufacturing technologies, PolyJet, SLA, and FDM are the most frequently applied in vascular phantom research due to their balance of resolution, material compatibility, and clinical relevance [16]. In addition, mDLP, though less commonly used, has recently been explored for producing very thin-walled structures and complex branching networks at high resolution [40]. All of these techniques are based on one of two main material classes: a liquid polymer solution that hardens under a specific condition, known as thermosetting polymers (PolyJet, SLA, DLP), or solid thermoplastic polymers that can be melted (FDM) [16].

2.1.1. *PolyJet (Material Jetting)*

Material jetting (PolyJet) printing is the most common direct printing technique for printing vascular phantoms [16]. It works by jetting microscopic droplets of liquid photopolymer onto a building platform, which are immediately cured by ultraviolet (UV) light, as can be seen in Figure 5. This process is repeated layer by layer until the complete structure is formed. PolyJet can combine multiple materials in a single print, which allows the simultaneous fabrication of rigid and flexible regions. This is particularly useful for vascular models, where stiff vessel segments can be integrated with compliant regions to better mimic mechanical behavior.

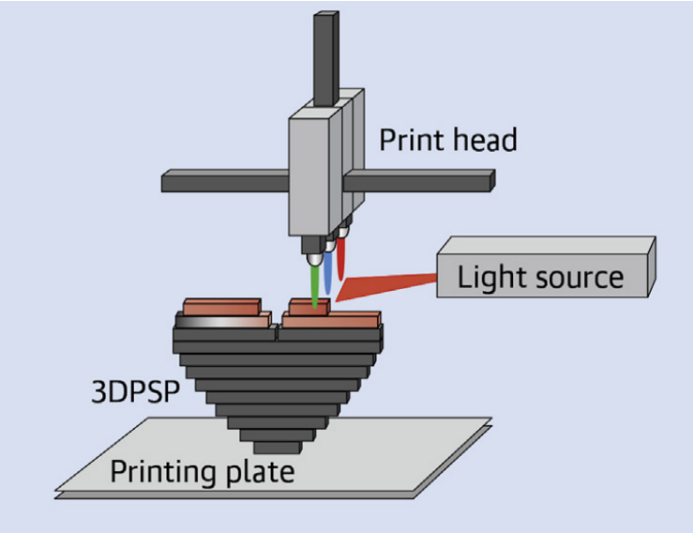

Figure 5: Schematic overview of PolyJet printing [16]

PolyJet printers typically achieve resolutions of 16–30 μm in layer thickness and lateral accuracy of about 50 μm, enabling high anatomical fidelity [28]. In practice, lumen geometries down to about 1–2 mm have been fabricated, with deviations of ~120 μm compared to patient imaging data [31]. Support material is often required to print hollow lumens and must be carefully removed after printing, which can be particularly challenging in tortuous or very small vessels. Despite this, PolyJet has been successfully applied to patient-specific models of the aortic root and carotid arteries, where fine anatomical details were reproduced with sub-millimeter accuracy [16].

The most commonly used materials in PolyJet 3D printing for vascular phantom fabrication are photocurable thermoset resins, typically acrylic- or methacrylate-based photopolymers. Among these, the two most widely employed are MED610 and VeroClear (RGD810), both developed by Stratasys, one of the world's leading companies in industrial 3D printing technology, for multi-material PolyJet systems [31, 15, 41]. MED610 is a transparent, biocompatible methacrylate photopolymer commonly used for anatomical modeling and device testing due to its high tensile strength of approximately ~40–55 MPa and Young's modulus, also called elastic/tensile modulus, of ~2.2–3.0 GPa [42], which provide mechanical robustness and dimensional stability during repeated handling and flow experiments [41, 15]. VeroClear (RGD810), an acrylic-like rigid photopolymer, exhibits a similar Young's modulus of ~2.0–3.0 GPa and tensile strength of ~50–65 MPa [43] and offers excellent optical transparency, making it particularly suited for phantoms requiring detailed visualization of internal flow structures under CT or fluoroscopy [31, 15]. Despite these advantages, when one of both materials is used to form a phantom, it is significantly stiffer and lack the anisotropic fiber structure of native arteries, which typically show nonlinear viscoelastic behaviour and an elastic modulus of only ~0.2–1.0 MPa [11].

Overall, PolyJet is highly suitable for vascular phantoms requiring complex branching networks, optical accessibility, and multi-material regions, though difficulties in support removal, high printer and material cost, and long-term durability of the resins remain important disadvantages [44, 41, 15]. Besides that, they are less suited for studies that require physiologically accurate wall compliance or strain-stiffening simulations.

2.1.2. *Stereolithography*

Stereolithography (SLA) is, alongside PolyJet, one of the most widely used additive manufacturing techniques for vascular phantoms. It relies on photopolymerization, where a liquid resin is selectively cured by ultraviolet (UV) light to form solid structures layer by layer (Figure 6). In a typical SLA setup, a build platform is submerged in a vat of resin, and a focused UV laser scans across the resin surface to trace the cross-sectional pattern of the phantom, curing only the exposed regions. After each layer, the platform shifts, allowing the next layer to be built until the full geometry is complete [16]. In addition to conventional SLA, two important variants are discussed in this section: multi-material stereolithography (MMSL) and masked stereolithography (mSLA), both of which expand the capabilities of standard SLA in terms of material properties, build complexity, and printing speed.

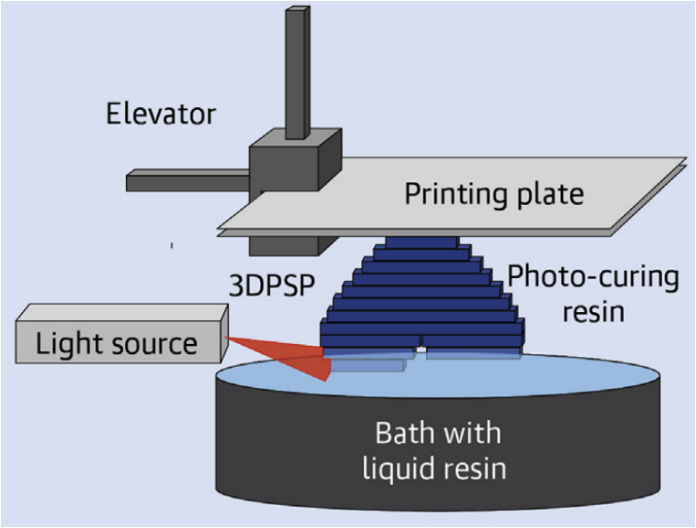

Figure 6: Conventional SLA [16]

SLA printers can achieve very high resolution, up to 5 μm, but typically achieve resolutions around 25–100 μm, which is sufficient to reproduce vessel walls, bifurcations, and aneurysms at physiologically relevant scales [16]. Although SLA enables millimeter-scale and sub-millimeter features, fabricating very fine microvascular structures (<200 μm) remains challenging in practice due to resin overcuring and reduced precision in reproducing small, complex details [5, 15]. The smooth surface finish reduces internal wall roughness, which is advantageous for flow experiments where turbulence and boundary conditions matter [5].

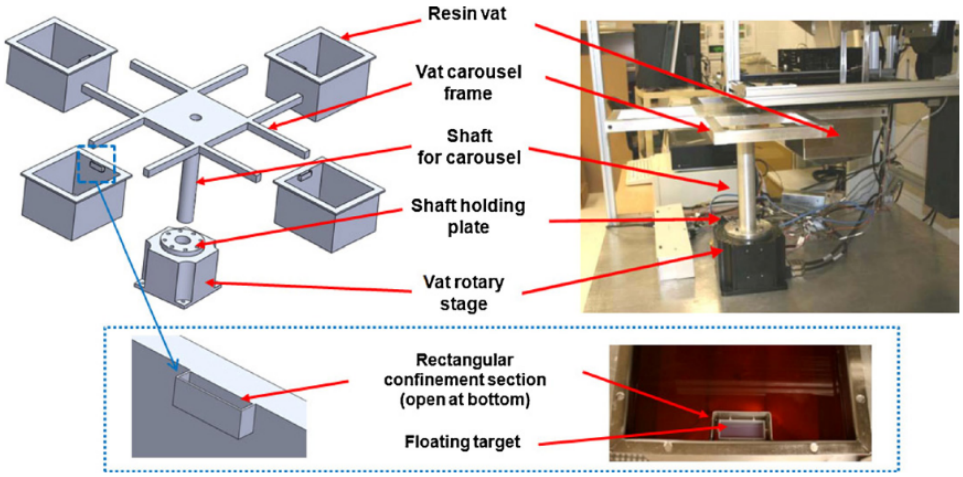

Figure 7: Example of a MMSL system [45]

Multi-material stereolithography (MMSL) extends conventional SLA by enabling the use of multiple resins within a single build. For example, Choi et al. demonstrated a custom-built MMSL system (Figure 7) by retrofitting a commercial SLA printer with a rotating vat carousel and control system, allowing seamless switching between resins during printing [45]. Other approaches rely on wavelength-programmable curing, selectively activating different photoinitiators within the same vat to achieve spatially varied properties [46]. Resolutions remain comparable to conventional SLA (25–100 μm), but MMSL offers the ability to produce regions

with distinct stiffness, transparency, or radiopacity within one vascular phantom [47]. For vascular applications, conventional single-material SLA already provides sufficient resolution and smooth walls for most models; MMSL may offer added value if regional variation in stiffness or optical properties is required (e.g., mimicking softer aneurysm domes or embedding radiopaque features), though with greater technical complexity than single-material SLA.

Figure 8: Masked stereolithography (mSLA) [48]

Masked SLA (mSLA, also called LCD-based photopolymerization) is a variant of vat curing where each layer is exposed using a masked light pattern (e.g., via a liquid crystal display (LCD) screen) rather than a scanning laser [49]. As shown in Figure 8, the build platform approaches from above, while the light source is positioned below the resin vat. A UV Light Emitting Diodes (LED) array projects light upward through an LCD digital mask placed directly under the transparent bottom of the resin tank, where each pixel of the screen either blocks or transmits light, enabling layer-by-layer curing of the photopolymer resin. This approach increases printing speed while maintaining relatively high resolution [50, 51]. mSLA is increasingly adopted in consumer and biomedical printing contexts [50].

In the context of vascular phantoms, Ngatane et al. used mSLA to reproduce soft printable phantoms for flow simulation, achieving ~22 μm pixel resolution and functional lumens down to ~200 μm, with tunable elasticity via resin blends (tensile strength ~1.1–6.0 MPa) suitable for vascular tissue modeling [51]. Milovanovic et al. also explored the mechanical performance of mSLA prints (e.g., compressive and flexural responses) in general 3D printing materials (several rigid, acrylate-based mSLA resins), providing mechanical data that can inform material selection and modification for vascular phantom fabrication [52]. Because mSLA uses a mask, it can potentially produce features faster and more uniformly than laser SLA, but its practical resolution and material performance are still bounded by optics, resin chemistry, and layer adhesion. Many of the same photopolymer materials used in SLA can also be adapted to mSLA, so the mechanical and optical properties tend to overlap [53].

The materials used for both SLA and mSLA are mainly photopolymerizable acrylate- or methacrylate-based liquid resins, which form crosslinked thermoset polymers after curing [46, 47]. These materials are widely used in vascular phantom fabrication due to their high optical clarity, smooth surface finish, and ability to reproduce fine anatomical features [15, 16]. Among commercially available options, two frequently employed materials are Formlabs Clear Resin (FLGPCL04) and Formlabs Flexible 80A Resin (FLFL8001). Formlabs Clear is a rigid, transparent photopolymer designed for anatomical modeling, with a reported tensile strength of 65 MPa and a Young's modulus of approximately 2.8 GPa [54, 15]. These properties make it particularly suitable for phantoms requiring high geometric fidelity and excellent visualization under imaging modalities such as CT and fluoroscopy [15].

In contrast, Formlabs Flexible 80A Resin exhibits a significantly lower tensile strength of around ~8.9 MPa; although the datasheet for Formlabs Flexible 80A does not report a Young's modulus explicitly, the measured tensile strength (~8.9 MPa) and stress at 100% elongation (~6.3 MPa) suggest its small-strain modulus is likely in the single-digit MPa range (e.g., ~5–10 MPa) [55]. This is consistent with its Shore hardness (80A, a material's resistance to indentation) and rubbery character, allowing for the fabrication of more compliant, deformable models that better mimic arterial nonlinear elasticity and strain-dependent deformation, though much stiffer than many hydrogel materials [15]. While both materials are used to create phantoms that remain more isotropic and

less viscoelastic than native arteries, their combination of optical transparency, surface smoothness, and dimensional precision has made SLA-based resins a standard choice for patient-specific vascular phantom fabrication. Another line of work in multi-resin mSLA has shown that combining poly(ethylene glycol) diacrylate (PEGDA) and ethylene glycol phenyl ether acrylate (EGPEA) monomers can produce microfluidic features with spatial stiffness control, making parts of the phantom stiffer in some areas and more flexible in others, which is promising for vascular modelling [50].

The main advantages of SLA and its variants are high geometric fidelity, reproducible thin-walled structures, smooth internal surfaces, and a relatively large build volume. Limitations include resin cost, post-processing requirements, and the brittleness of many commercial resins [16, 15]. Overall, conventional SLA already provides sufficient resolution and surface quality for most vascular models. MMSL or mSLA can add value when regional variation in stiffness, transparency, or radiopacity is required, although MMSL is currently limited to custom-built, non-commercial systems, which increases process complexity and limits its widespread adoption.

2.1.3. Fused Deposition Modeling (FDM)

Fused Deposition Modeling (FDM) fabricates models by extruding thermoplastic filaments through a heated nozzle and depositing them layer by layer, which can be seen in Figure 9.

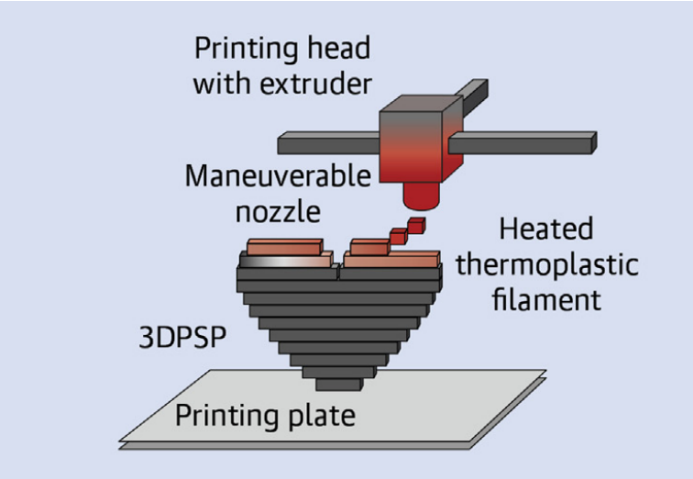

Figure 9: Schematic overview of FDM [16]

Common materials include Polylactic Acid (PLA), Acrylonitrile Butadiene Styrene (ABS), and Thermoplastic Polyurethane (TPU), which are mostly stiff materials (thermoplastics) [16, 56]. For example, PLA can have a Young's modulus of ~2.6–3.0 GPa and tensile strength ~46–50 MPa (for XY orientation) in commercial PLA filaments [57]. Another example, TPU 92A, a flexible thermoplastic, can have a Young's modulus of ~15.3 MPa and tensile strength ~16.8 MPa (for XY orientation), which offers elasticity but is more challenging to print accurately at thin walls [58]. Although the resolution of an FDM printer is generally lower compared to SLA or PolyJet, under optimized conditions FDM can produce microchannels as small as 70 μm in width [59], though reliably printing thin wall structures below 200 μm in all dimensions remains challenging for FDM printers.

For vascular phantoms, FDM is often used to create rigid models for imaging studies. Examples include AAA phantoms and simplified vascular geometries with lumen diameters in the range of several millimeters reproduced accurately enough for flow visualization and device testing [15]. Besides their relatively low resolution, FDM remains a popular choice due to its low cost and widespread availability.

Thus, FDM is not well-suited for phantoms requiring compliant thin walls or very small/tortuous vessels. The lines of each printed layer are visible, which affects the internal surface and leads to roughness. However, it is highly practical for low-cost prototyping and large-scale models [60].

2.1.4. *micro-Digital Light Processing (mDLP)*

Digital Light Processing (DLP) is a vat-photopolymerization technique that uses a digital micromirror device (DMD) to project an entire layer of light patterns onto a photosensitive resin, curing one full cross-section at a time [61], see Figure 10. Unlike conventional SLA, which employs a laser beam to trace each voxel individually, DLP can cure a whole layer simultaneously with the help of a lens that spreads the light over the entire surface of the resin. This significantly improving printing speed while maintaining high resolution [40]. The clear film located at the bottom of the vat acts as a separation layer between the printed part and the vat, ensuring that the cured layers can detach smoothly as the build platform (stage) moves upward. This prevents the cured material from sticking to the vat and maintains the quality of the printed structure.

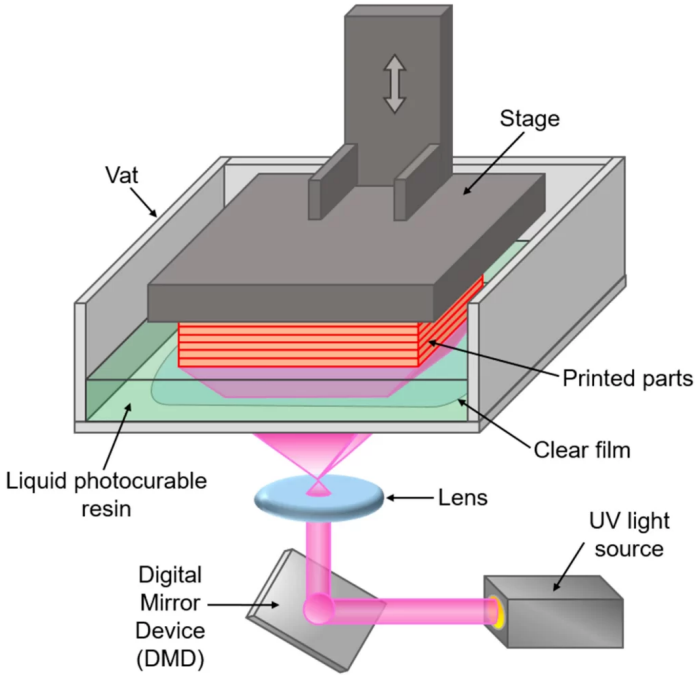

Figure 10: Conventional DLP [61]

Printer resolutions down to 18×20 μm can be achieved, for which resolutions below 100 μm have been demonstrated for microfluidic channels, making this technique especially suitable for vascular phantoms that require thin-walled, hollow structures and complex branching networks [40, 62, 63].

The projection system consists of a UV or visible light source (300–405 nm), a DMD chip with thousands of movable micromirrors, and focusing optics. Each micromirror tilts to direct or block light, creating a pixelated projection pattern that defines the cured resin areas. The achievable resolution depends on the DMD pixel pitch and the optical system used to scale the image, typically ranging from a few micrometers to tens of micrometers [40]. This trade-off reflects the balance between field-of-view and minimum feature size. In other words, higher resolution results in a smaller field-of-view, which indicates a smaller building platform; therefore, the phantom size is limited.

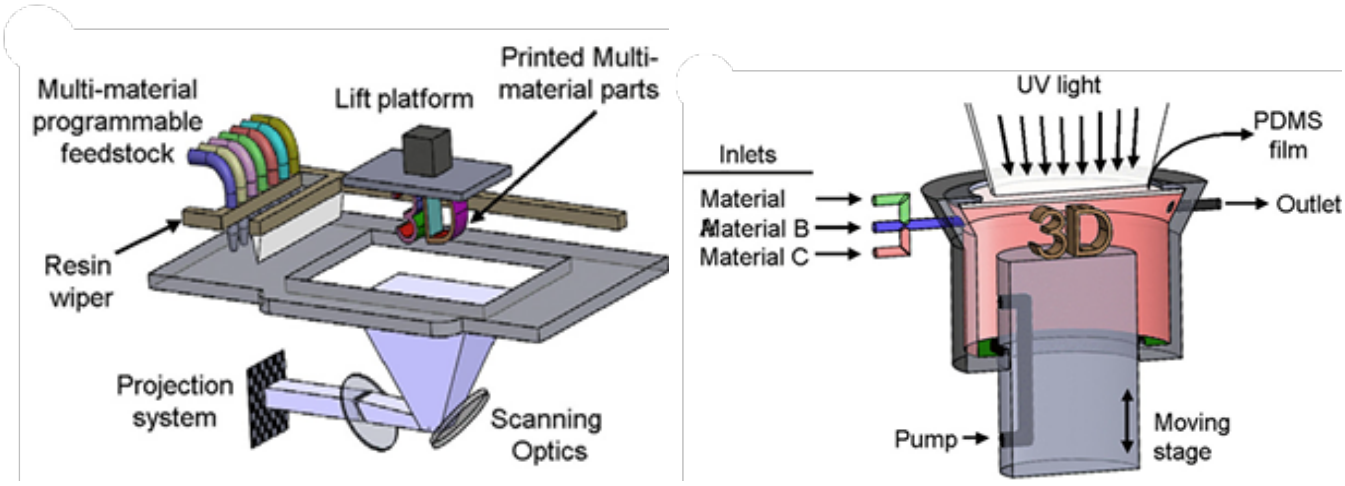

Figure 11: Examples of DLP setups: (left) open-vat system and (right) closed-vat system, both enabling high-resolution fabrication of microvascular geometries [40].

Different system configurations exist to implement DLP printing, most notably the two main approaches shown in Figure 11: open-vat systems, which allow easier resin exchange, and closed-vat systems, which offer more controlled curing environments [40]. The open-vat system is particularly useful for multi-material printing, as it allows for easy switching between different resins, enabling the creation of complex structures with varying material properties. On the other hand, closed-vat systems provide a more controlled curing process, improving print accuracy and quality, which is especially important for high-resolution vascular phantoms with precise material requirements.

Recent developments have led to so-called micro-DLP (mDLP), also referred to as projection micro-stereolithography (PμSL). These systems use modified optics to shrink the projection area, reducing the effective pixel size of the DMD and thereby reaching much finer resolutions than conventional DLP. For example, resolutions as low as ∼2–5 μm have been demonstrated, enabling the fabrication of very thin walls and highly curved geometries that are difficult to achieve with standard DLP setups [62, 40]. This resolution improvement is particularly beneficial for vascular phantoms, where lumen diameters in the sub-millimeter range and wall thicknesses below 100 μm are critical for replicating physiological compliance and flow dynamics.

In addition, commercially available mDLP systems have also introduced specialized resin formulations optimized for vascular or microfluidic applications. For instance, MicroSLA (modified high-resolution SLA printer which acts as an mDLP printer) offers two standard photopolymers specifically designed for high-resolution printing: FLEX, a flexible material with resolutions between 15–37 μm that is suited for fabricating compliant vascular structures, and CLEAR, a transparent resin with resolutions between 25–37 μm particularly useful for microfluidic channels and optical access [64]. According to their technical datasheets, FLEX resin exhibits a tensile strength of 5.4 MPa [65], while CLEAR resin reaches a tensile strength of 24.5 MPa and a Young's modulus of 1190 MPa [66].

Across the (micro)DLP literature on vascular phantoms (or vessel-like constructs), the two most frequently used flexible material systems are PEGDA hydrogels and gelatin methacrylate (GelMA) –based hydrogels, often used in combination (GelMA/PEGDA) to tune mechanics and printability [40, 63, 4]. PEGDA's crosslink density (determined by its concentration) allows Young's modulus to be tuned broadly, from $\sim$ 10–10^3 kPa up to the low-MPa range, supporting thin, compliant walls for flow studies [67, 68]. GelMA provides a bio-derived viscoelastic behavior and nonlinear response when used in models, with Young's moduli typically in the $\sim$ 1–100 kPa range (increasing with degree of methacrylation and GelMA concentration). When blended with PEGDA, the composite retains DLP printability while improving the robustness of hollow microchannels [69, 70]. Recent DLP/mDLP works explicitly bioprint GelMA/PEGDA vascular geometries (sub-mm channels) and report that these hydrogels deliver the needed compliance and viscoelastic response in the final model, allowing vessel-like behavior, though at stiffnesses still below native arterial strain-stiffening and anisotropy [71, 40].

Besides all the advantages, DLP systems face considerable limitations when fabricating vascular geometries. Curved, thin-walled, or hollow structures are particularly sensitive to printing defects, where excessive light exposure may cause unintended curing of surrounding regions, while insufficient adhesion between layers can lead to weak interfaces. These issues contribute to dimensional inaccuracies, feature merging, or reduced mechanical strength of the printed phantom [62]. Another disadvantage is the small build area, which limits the phantom size.

2.2. *Sacrificial Mold Casting*

In addition to direct 3D printing, sacrificial mold casting (indirect printing), where a temporary, dissolvable, or removable mold is created, filled with the target material, and then removed to leave behind the intended geometry, remains the most widely used approach for vascular phantom fabrication. This dominance reflects its ability to produce compliant and transparent models at relatively low cost, while direct 3D printing is still limited by material stiffness and durability [4, 72]. This strategy enables the use of compliant elastomers and hydrogels that better replicate the mechanical properties of vessel walls, while still capturing complex lumen geometries. Sacrificial molds are first fabricated, typically by 3D printing (mostly FDM) a soluble or removable core, which is then coated or embedded in a casting material. After curing, the core is removed to leave behind a hollow structure [4]. Several casting approaches have been developed for vascular applications, with the most prominent being lost-core casting, lost-mould casting (also spelled as lost-mold casting), and dip-spin coating. Each method offers specific advantages and challenges, depending on the required geometry, wall thickness, and optical clarity, as discussed in the following subsections.

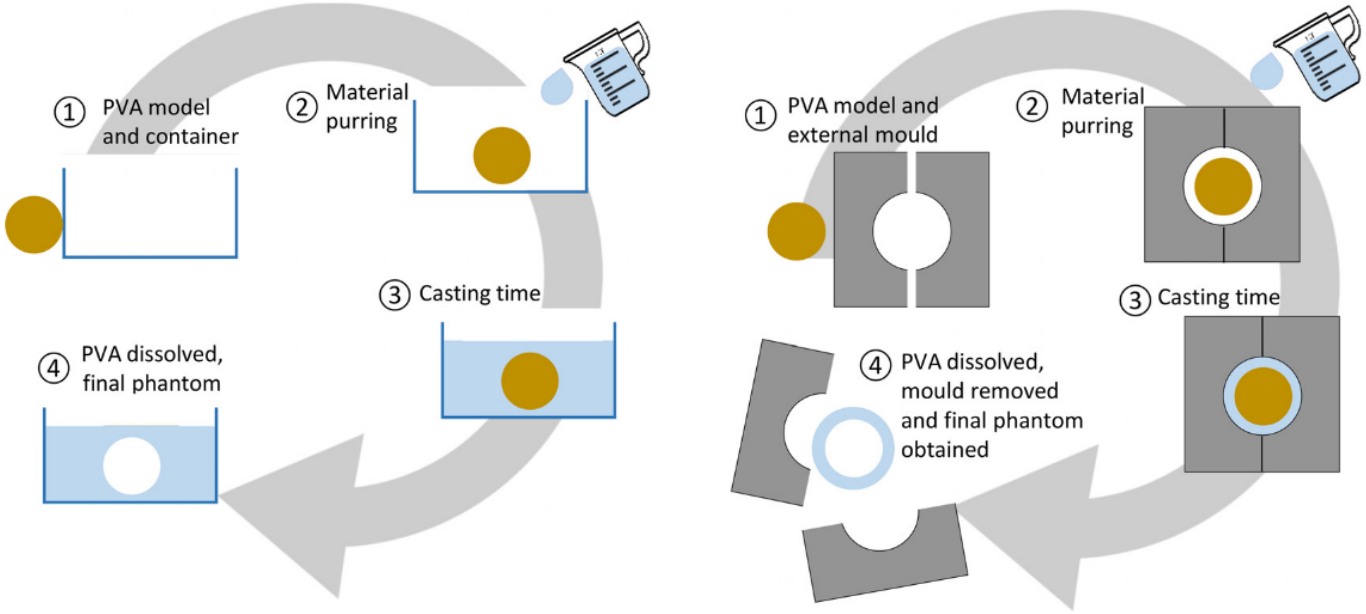

(a) Lost-core casting

(b) Lost-mould casting

Figure 12: Schematics of the two casting options: (a) lost-core casting, where a model is enclosed and the casting material poured around it, resulting in a hollow structure once the core is dissolved; and (b) lost-mould casting, where a positive mould is included to control the wall thickness of the phantom, resulting in a physical model with the shape of the vessel of interest [60].

2.2.1. *Lost-Core Casting*

Lost-core casting is the most commonly reported sacrificial method for vascular phantoms [72]. A soluble core of the vessel geometry is 3D printed and embedded in vascular phantom material. After curing, the core is dissolved in water, leaving behind a hollow, compliant vascular structure, see Figure 12a. This method enables the fabrication of complex vascular geometries, such as aneurysms or bifurcations, with smooth lumens suitable for flow experiments [60, 72]. Typical lumen diameters fabricated with lost-core techniques are in the 0.8–2 mm range, but features down to ~500 µm have been reported with higher-resolution core printing (e.g., SLA) [60]. Key advantages include low cost and the ability to produce patient-specific phantoms, while limitations involve incomplete core dissolution and variable wall thickness.

The most widely used materials in lost-core casting are polyvinyl alcohol (PVA) and polydimethylsiloxane (PDMS). The inner core is made from PVA, which is water-soluble and ideal for creating complex internal geometries that can be dissolved post-casting, leaving behind the vascular lumen. PDMS is widely used as a casting material for vascular phantoms, as the resulting models exhibit viscoelasticity, compliance, and a tunable elastic modulus (0.6–1.3 MPa), enabling them to replicate the mechanical behavior of blood vessels. [34, 72, 73, 33].

2.2.2. Lost-Mould Casting

Lost-mould casting relies on rigid external moulds (male/female halves) that define the vessel geometry. PDMS or epoxy resins are injected between the moulds, cured, and then the mould is removed, as can be seen in Figure 12b. Compared to lost-core methods, lost-mould casting provides excellent surface smoothness and reproducibility of wall thickness, but it is less suited for highly tortuous geometries [72, 33]. Achievable lumen sizes are usually 1–5 mm, with sub-millimeter features (~700 μm) possible using high-resolution SLA moulds [60]. This approach is often applied for larger vessels, such as the aorta, where smooth lumens and uniform walls are critical.

The most common sacrificial or removable mould materials are PVA and acrylonitrile butadiene styrene (ABS) [72]. Where PVA can be easily dissolved after curing, while ABS offers mechanical strength and dimensional stability but requires mechanical removal. As final vascular phantom material, PDMS and epoxy resins are frequently employed. As mentioned before, models created from PDMS offer transparency, nonlinearity, and vessel-like compliance, making it suitable for dynamic flow studies, while epoxy resins are used for rigid phantoms due to their high stiffness and optical clarity [60, 33, 72].

2.2.3. Dip-Spin Coating

Dip-spin coating is a hybrid approach that uses a 3D-printed soluble core as a temporary mould, which is repeatedly dipped into a silicone or elastomer solution and rotated to ensure a uniform coating. After curing, the core is dissolved, leaving behind a transparent, hollow phantom with thin and uniform walls. This method is particularly attractive for cerebral aneurysm phantoms, where very thin walls (<300 μm) and optical access are required for flow visualization [74, 34]. However, the lumen size is again dictated by the soluble core (often printed with FDM/SLA), so typical vessel diameters remain in the 0.5–2 mm range [60]. Its advantages are optical clarity and thin, reproducible walls, while its drawbacks include limited applicability to complex vascular networks and a work-intensive fabrication process.

In dip-spin coating approaches, a pre-fabricated core (often 3D-printed from PVA) is coated with the final phantom material rather than being embedded in a casting mould. The coating is typically composed of silicone elastomers (e.g., HY_E620, SL_5200) and PDMS. The phantoms made from these materials offer viscoelasticity, flexibility, and compliance similar to arterial tissue. The controllable wall thickness achieved with this method is ideal for studying hemodynamic parameters such as vessel wall strain and pulsatile response [73, 33, 74].

2.3. Comparison between techniques

A comprehensive comparison of fabrication methods is key to choosing an appropriate technique for vascular phantoms. Below are two tables: Table 2 compares resolution and vessel size applicability, and Table 3 contrasts materials and mechanical properties, including real artery values for reference.

Table 2: Resolution vs vessel scale for different techniques

Technique	Layer / printer resolution (μm)	Phantom resolution (μm)	Vessel scale category	Sources
Micro-DLP	2–5	<50	Small arteries / arterioles (10–300 μm)	[40, 62, 63]
DLP	18–20	<100	Small arteries (0.1–1 mm)	[40, 62, 63]
PolyJet	16–30	<200	0.5–3 mm arteries	[15, 31, 28]
SLA (MMSL, mSLA)	25–100	~100–300	Medium arteries (1–4 mm)	[16, 5, 15]
FDM	100–200 (Z) / 200–400 (XY)	~1–2 mm	Large arteries (5–10 mm)	[15, 60, 59]
Sacrificial Mold Casting	300–700	~0.5–5 mm	Medium to large arteries	[16, 60, 34, 74]

Table 2 shows that micro-DLP is the only technique capable of reliably achieving sub-50 μm features, making it suitable for the smallest arteries and arterioles. SLA and PolyJet form the mid-range, enabling bifurcations and aneurysms in medium-sized arteries. FDM and sacrificial casting are primarily suitable for large vessels due to their lower resolution. In practice, printed phantoms often deviate from nominal resolution: Nguyen et al. reported dimensional errors up to ±2–3% in vascular models fabricated by FDM, SLA, and PolyJet [75]. This means that a safety factor must be considered in design (e.g., slightly larger target dimensions) to ensure reliable fabrication.

Table 3: Material & mechanical properties comparison (with native artery as reference)

Technique	Common Materials	Young's Modulus	Tensile Strength	Compliance / Viscoelasticity	Transparency	Sources
Native artery	Collagen–elastin composite	0.2–1.0 MPa (healthy), up to ~3.8 MPa (diseased)	1.2–2.3 MPa	High compliance, nonlinear, viscoelastic	Opaque / semi-translucent	[11, 6]
(Micro-) DLP	PEGDA / GelMA	0.01–1.0 MPa	~1.5 MPa	High compliance, tunable viscoelastic behavior	Moderate	[40, 4, 63, 67, 76, 69, 70]
PolyJet	MED610, VeroClear	2.0–3.0 GPa	40–65 MPa	Very low compliance (stiff)	High	[15, 31, 42, 43, 41]
SLA (mSLA)	Clear Resin, Flexible 80A	~2.8 GPa/5–10 MPa	~8.9 MPA/~65 MPa	Low to moderate compliance	High	[15, 47, 54, 55]
FDM	TPU, PLA, ABS	~15.3 MPa/2.6–3.0 GPa	~16.8 MPa/46–50 MPa	Low compliance, TPU has flexibility	Low	[16, 56, 57, 58]
Sacrificial Casting	PDMS, silicone elastomers/epoxy resins	0.6–1.3 MPa	~2.24 MPa	High compliance and viscoelasticity	Low to moderate	[72, 34, 73, 77, 33]

Table 3 shows clear differences between fabrication methods in terms of mechanical performance. Most vat photopolymer techniques (in this case PolyJet and SLA) generally produce models with significantly higher stiffness compared to native arteries. PolyJet, in particular, relies on acrylate-based thermosets that form highly cross-linked networks, resulting in moduli in the GPa range. SLA is more versatile: rigid resins (e.g., Clear Resin) are very stiff, while flexible resins (e.g., Flexible 80A) achieve moduli in the MPa range. In practice, SLA phantoms often use blends of rigid and flexible resins to balance stiffness and geometry [78, 47], while different resin selections are applied depending on the vascular application [15]. This means that reported values in the table may vary in real applications, as blends and additives can all shift the final mechanical behavior. The same goes for FDM materials, which show a wide range: rigid PLA/ABS are far too stiff, while TPU offers some flexibility but remains above arterial values.

Vascular phantoms created from casting materials (PDMS, silicone) and hydrogel-based DLP approaches are closest to physiological mechanics but are often limited by geometry. This mechanical mismatch is why one must trade off between structural precision and realistic vascular behavior.

From this comparison, SLA and micro-DLP emerge as the most balanced choices: SLA is well suited for medium-sized arteries (1-4 mm), particularly where a blend of rigid and flexible materials is used, and micro-DLP offers unmatched resolution for small arteries and arterioles (10–300 μm). FDM and sacrificial casting, while valuable for large-scale or cost-effective models, remain unsuitable for fine, compliant, small-diameter phantoms. The combination of SLA and micro-DLP thus provides the most effective route to multiscale, anatomically realistic, and mechanically relevant vascular phantom fabrication.

2.4. Manufacturing validation

Manufacturing validation assesses whether the phantom has been fabricated according to the required specifications and whether the chosen materials reproduce anatomical and mechanical targets. Since fabrication methods and material choices are central to Chapter 3, this type of validation provides a direct measure of manufacturing success. Imaging-based comparisons test whether the phantom's contrast and signal properties align with clinical data, for instance, CT studies assess whether the Hounsfield Unit distribution of phantom materials falls within physiological ranges [79, 80], while Doppler ultrasound evaluates whether flow signals correspond to those observed in patients. Geometry is verified through high-resolution imaging (e.g., CT or micro-CT) to check wall thickness and lumen dimensions against segmented anatomy [81], and in some cases, physical measurements such as microscopy of cut sections are used [82]. Mechanical validation complements this by pressure–diameter tests, for example, which allow researchers to calculate compliance values (typically 0.1–0.2 mmHg^{-1} for carotid arteries), while tensile experiments determine burst pressure and fatigue resistance [6]. These measurements are critical to verify that the phantom walls deform under load in a manner similar to native arteries, ensuring that devices tested in the phantom experience clinically relevant forces.

Together, functional and manufacturing validation underline that phantom fidelity is not a single property but the outcome of multi-level testing. Functional validation ensures that the vascular phantom serves its purpose in replicating physiological flow, while manufacturing validation verifies that the chosen fabrication technique and material provide the correct anatomical, mechanical, and imaging properties. Despite progress in both areas, many studies still emphasize imaging outcomes while neglecting systematic mechanical benchmarking, underscoring the need for standardized, multi-parametric validation frameworks [11, 16].

3. Conclusion

This review provides a comprehensive overview of the current state of vascular phantom fabrication by addressing five central questions: (i) the current capabilities of the field, (ii) the main fabrication techniques and materials, (iii) the differences in resolution, mechanics, and geometry between these methods, (iv) the extent to which physiological conditions can be replicated across different vessel scales, and (v) the key limitations and challenges that remain.

Current capabilities. The field of vascular phantom fabrication has advanced significantly, moving beyond simple straight tubes toward complex, patient-specific geometries that replicate real vascular networks. Modern techniques allow for high geometric fidelity, thin-walled hollow structures, and bifurcations with sub-millimeter precision. Additionally, functional validation, such as flow visualization, hemodynamic assessment, and device testing, is now widely incorporated. These developments have transformed vascular phantoms into powerful tools for pre-clinical research, surgical training, medical device evaluation, and imaging calibration.

Fabrication techniques and materials. Two fabrication strategies dominate: direct 3D printing and sacrificial mold casting. Direct methods, including PolyJet, SLA (and its variants MMSL and mSLA), and (micro)DLP, enable highly detailed, transparent phantoms with excellent geometric accuracy. Among these, micro-DLP pushes resolution to the single-micron scale, enabling small-vessel replication, while SLA and PolyJet excel in producing smooth, optically clear models suitable for imaging studies. Sacrificial mold casting remains the most widely used approach due to its ability to incorporate compliant elastomers and hydrogels that more closely mimic the mechanical behavior of blood vessels. Material selection depends strongly on the intended application: photopolymers are ideal for precision and clarity, silicones and elastomers, such as PDMS, for mechanical compliance, and hydrogels (such as PEGDA and GelMA) for tunable mechanical properties and biocompatibility.

Resolution, mechanics, and geometric complexity. Each fabrication technique offers different advantages and limitations. Micro-DLP achieves the highest resolutions (2–5 μm), which is crucial for replicating microvasculature and lumens below 200 μm. SLA and PolyJet provide excellent surface quality and are ideal for medium-scale vessels, while casting methods are better suited for compliant large-vessel phantoms. Mechanical properties vary widely: photopolymers are typically orders of magnitude stiffer than native arteries, while elastomers and hydrogels can produce phantoms with elastic moduli and viscoelastic behavior closer to physiological ranges. Direct 3D printing enables the fabrication of complex geometries but is often limited by support removal and overcuring. Casting, while simpler and more cost-effective, struggles with complex branching and uniform wall thickness control.

Physiological replication. Current vascular phantoms successfully reproduce anatomical structures with high fidelity, enabling accurate simulation of blood flow dynamics and pressure–flow relationships in large and medium vessels. Optical clarity allows visualization under modalities such as CT, fluoroscopy, and ultrasound, while tailored resin formulations enable localized tuning of properties (e.g., stiffness or radiopacity). At smaller scales, advances in hydrogel materials and micro-DLP fabrication improve mechanical compliance and flow conditions, though fully replicating arterial anisotropy, viscoelasticity, and strain-stiffening remains an ongoing challenge. Additionally, no single material matches the combined acoustic, radiological, and mechanical properties of native tissue, forcing researchers to prioritize one property over others, depending on the intended application.

Limitations and challenges. Despite these advances, several critical limitations continue to shape the field and define future research priorities:

- *Mechanical mismatch:* Most printable materials remain significantly stiffer than real vascular tissue, lacking the nonlinear, viscoelastic, and anisotropic characteristic of real vascular tissue within vascular phantoms [28].
- *Resolution versus scalability:* Achieving ultra-high resolution (e.g., sub-5 μm features) with micro-DLP often comes at the expense of build volume and fabrication speed. This trade-off complicates the production of large, anatomically relevant phantoms while maintaining fine microvascular detail [40].
- *Surface quality and post-processing:* Support removal, incomplete resin curing, and surface roughness can distort lumen geometry or affect flow. In casting methods, incomplete core removal can lead to wall irregularities [31]. Improving surface smoothness and internal cleaning processes is essential for accurate flow simulation and reproducibility.
- *Multimodal imaging compatibility:* Materials optimized for one imaging modality (such as CT or MRI) often perform poorly in others [39]. Adding contrast-enhancing agents or fillers to the base material to make vascular phantoms visible under different imaging modalities may also compromise mechanical properties or printability, posing a challenge for phantoms intended for multi-imaging validation.
- *Durability and standardization:* Long-term performance under pulsatile flow is not well characterized, and the lack of standardized testing protocols for geometry, compliance, and imaging metrics limits cross-study comparisons [83, 16]. Establishing shared benchmarks and clear validation frameworks is necessary to ensure reproducibility and comparability across studies.

- *Multi-material integration:* Combining materials with different properties to mimic heterogeneous vessel structures or to include special functional features remains technically difficult. Reliable interfacial bonding and precise control over multi-material transitions are key challenges that must be addressed to advance the realism of vascular phantoms [84].

These limitations mark the current challenges in vascular phantom research. Addressing them requires collaboration between tailored material selection, high-resolution fabrication, computational modeling, and experimental validation. Future research should focus on the development of complete phantom systems that combine mechanical durability, anatomical accuracy, and consistent flow performance across different vessel scales. Additionally, creating shared testing methods and clear evaluation standards will make it easier to compare results between studies and speed up the process of using vascular phantoms in real medical applications.

In conclusion, vascular phantom fabrication has evolved into a versatile and impactful field, capable of producing anatomically accurate, functionally relevant, and application-specific models. However, its full potential has not yet been realised. Addressing the remaining challenges, including mechanical realism, multimodal imaging compatibility, scalability, and material integration, will be important for the next generation of vascular phantoms. By bridging these gaps, future phantoms could more accurately replicate the structure and behaviour of real vascular systems and support clinical innovation, device testing, and personalised treatment planning.

4. Research gap

Despite the progress described in the literature review, an important challenge remains for small-scale flexible vascular phantoms. The lumen must remain open after printing and post-processing, while the channel wall must remain soft enough to deform under pressure. Achieving both requirements simultaneously is difficult because the final channel geometry is influenced by printer resolution, material properties, and post-processing conditions [5, 4]. At the same time, flexible channels can change their cross-section under pressure-driven flow, which means that geometrical accuracy alone is not sufficient to evaluate their functional behaviour [85].

A second challenge is the experimental assessment of pressure-induced diameter change. For vascular phantoms, compliance can be described as the increase in vessel diameter for a given increase in pressure, and pressure-based testing can be used to evaluate this behaviour in cylindrical channel samples [11]. Since deformation of the channel wall can influence the pressure-flow response, both the material stiffness and the hydraulic behaviour must be measured to obtain an indication of channel expansion [85].

Therefore, there is a need for a fabrication and characterisation approach that combines printability assessment, geometrical accuracy measurements, mechanical testing, and pressure-flow experiments. Such an approach can help determine whether small-scale flexible vascular phantoms can be fabricated with adjustable stiffness and whether their pressure-dependent behaviour can be measured experimentally.

4.1. Research question

Based on this research gap, the main research question of this thesis is:

> *How can small-scale, compliant vascular phantoms with tunable stiffness be fabricated using 3D printing and experimentally characterized under pressure-driven flow?*

To answer this question, the thesis focuses on four main objectives. First, the printability of small straight channels is investigated by varying the lumen diameter and wall thickness. Second, the geometrical accuracy of the printed channels is evaluated and compared with the nominal CAD geometry. Third, the stiffness of the printed Elastomer-X material is characterized using tensile tests and adjusted by varying the printing and post-curing conditions. Finally, pressure-flow experiments are performed to determine whether the printed flexible channels show a measurable pressure-dependent change in effective diameter.

Research Paper

Fabrication of flexible 3D printed vascular phantoms: Investigating the impact of variable stiffness for diameter change under flow conditions

Lucas J. Zijlstra[a]

[a]*Department of Precision and Microsystems Engineering, Delft University of Technology, Mekelweg 2, 2628 CD Delft, The Netherlands,*

1. Introduction

In recent years, vascular phantoms have become an important tool in biomedical engineering and medical research [15, 81]. These artificial models are used to replicate the geometry and mechanical behaviour of blood vessels [7]. They bridge the gap between virtual planning and real clinical practice, offering a controlled and safe environment for medical imaging validation, radiotherapy, surgical training, and equipment testing [1, 86, 81]. An important advantage is that they reduce reliance on animal models and in vivo experiments, providing ethically acceptable and repeatable conditions for research and clinical training [1, 2]. The importance of phantoms spans multiple areas of modern healthcare, especially in fields where accurate diagnosis, treatment planning, and device validation are essential [3].

Traditional phantom manufacturing methods, such as moulding and casting, are often limited in terms of geometric complexity and cost [5]. In addition, each mould is typically designed for one specific geometry, which makes it unsuitable for reuse in other patient-specific applications. Additive Manufacturing (AM), better known as three-dimensional (3D) printing, has therefore become an attractive alternative. 3D printing enables the fabrication of complex and patient-specific geometries with relatively short production times. This makes it especially useful for vascular applications, where small channels, branching geometries, and local changes in vessel size are important [2, 3, 4].

Despite these advantages, several challenges remain. One important challenge is the combination of small-scale geometry and soft mechanical behaviour. The resolution of the printer, the printing technology, and the properties of the material limit the minimum vessel diameter and wall thickness that can be fabricated reliably [31, 5, 4]. At the same time, vascular phantoms should not only reproduce the vessel geometry, but also have mechanical properties that are relevant for blood vessels [7, 87]. This is important because vessels deform under pressure, and this compliance influences the relation between pressure, flow rate, and vessel diameter [10]. The mechanical behaviour of real vessels is complex and depends on elasticity, non-linearity, viscoelasticity, and vessel structure [11].

A second challenge is the experimental validation of flexible printed channels under flow conditions. Many studies on 3D printed cardiovascular phantoms focus on imaging, fabrication, material choice, and geometrical validation [16]. However, for compliant vascular phantoms, it is also important to test how the channel behaves under pressure and flow, because wall compliance can influence the pressure-flow response [33, 88]. Since the hydraulic resistance depends strongly on the channel diameter, pressure-flow measurements can be used to estimate changes in the effective diameter of flexible channels. Therefore, measuring the pressure-flow behaviour provides an indirect way to evaluate pressure-induced channel expansion.

Based on these challenges, the research gap addressed in this work is the need for a fabrication and validation method for small-scale flexible vascular phantoms that can be printed with controlled geometry and stiffness, and experimentally tested for diameter change under pressure-flow conditions.

The aim of this paper is therefore to develop a fabrication method for small-scale flexible vascular phantoms using masked stereolithography (mSLA), a resin-based 3D printing technique, and to experimentally investigate their diameter change under controlled pressure-flow conditions.

2. Approach

The approach of this study is based on the identified research gap: small flexible vascular phantoms with sub-millimeter lumens must be fabricated with a geometrical deviation below 10%, material stiffness within the relevant vascular range of 0.2–3.8 MPa [11, 6], and pressure-flow behaviour evaluated through a decrease in hydraulic resistance and an increase in effective diameter. A schematic overview of this approach is shown in Figure 13.

First, the manufacturing limits of the mSLA printer and elastomeric resin were investigated by printing straight channels with different lumen diameters and wall thicknesses. This step was used to determine which small flexible channels could be fabricated while remaining open and suitable for flow experiments. Secondly, the material stiffness was characterized using tensile tests. By changing the printing and post-curing parameters, slightly different Young's moduli were obtained. The configurations with the lowest and highest measured Young's modulus were selected for the pressure-flow experiments and are referred to as the E_- and E_+ configurations, respectively, although both remain within a relatively soft material range.

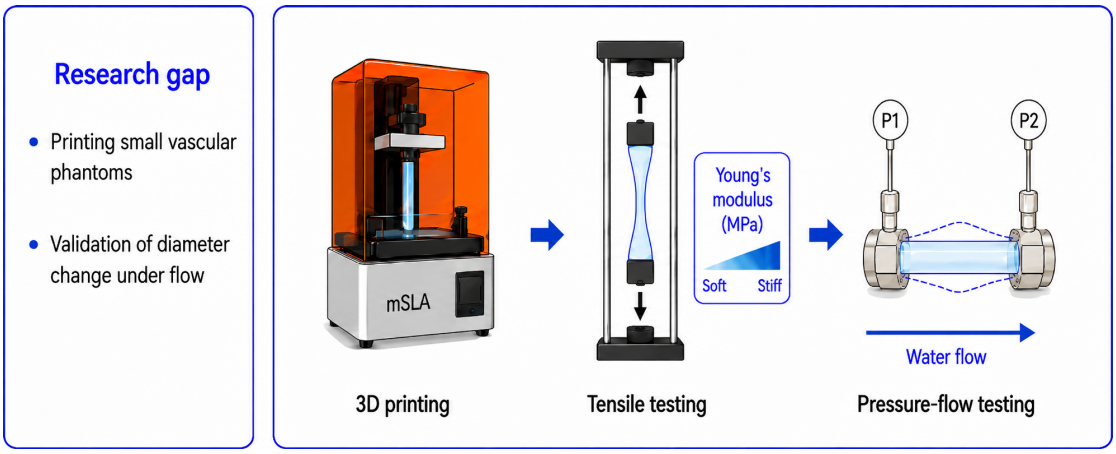

Figure 13: Schematic overview of the approach used to address the research gap. The workflow includes (1) mSLA 3D printing of small channels, (2) tensile testing to measure different Young's moduli and (3) pressure-flow testing to evaluate diameter change

Finally, the printed channels were tested in pressure-flow experiments to determine their hydraulic resistance and estimate the resulting effective diameter change. In this way, the fabrication method, mechanical properties, and functional compliance behaviour were linked together.

3. Theory

The pressure-flow experiments in this study are based on flow through a small flexible cylindrical channel. The main geometrical parameters are the inner diameter D, wall thickness t, and channel length L, as shown in Fig. 14a. During the experiment, water flows through the channel with volumetric flow rate Q, while the pressure is measured upstream and downstream of the test section as P_1 and P_2, respectively.

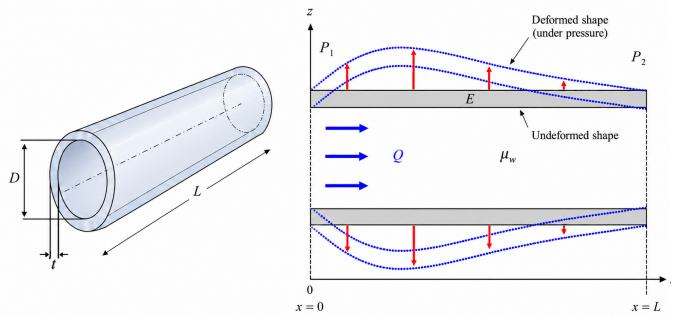

(a) 3D cylindrical channel (undeformed geometry) **(b)** 2D longitudinal xz–plane sketch of a flexible channel

Figure 14: Schematic representation of the flexible cylindrical channel used in the pressure-flow analysis. (a) Undeformed channel geometry with diameter D, wall thickness t, and length L. (b) Longitudinal xz-plane sketch showing the undeformed wall in grey and the deformed shape under pressure as blue dotted lines. The flow rate Q, water viscosity μ_w, pressures P_1 and P_2, and Young's modulus E are indicated.

The pressure drop across the channel, see Figure 14b, is defined as

$$\Delta P = P_1 - P_2. \tag{1}$$

The hydraulic resistance is defined as the ratio between the pressure drop and the volumetric flow rate:

$$R_\mathrm{h} = \frac{\Delta P}{Q}. \tag{2}$$

For a rigid cylindrical channel with diameter D, length L, and dynamic viscosity μ_w, the theoretical hydraulic resistance is given by the Hagen–Poiseuille relation [89]:

$$R_\mathrm{h} = \frac{128\mu_w L}{\pi D^4}. \tag{3}$$

This relation shows that the hydraulic resistance is highly sensitive to the channel diameter, since R_h scales with D^{-4}. Therefore, even a small pressure-induced diameter change can have a clear effect on the measured resistance.

The Hagen–Poiseuille relation assumes steady, laminar, incompressible, and fully developed flow. In this study, steady conditions were approached by applying pressure steps and using the averaged pressure and flow values after the initial transient response. The flow regime can be checked using the Reynolds number,

$$Re = \frac{\rho U D}{\mu_w}, \tag{4}$$

where ρ is the density of water and U is the mean flow velocity. Using $U = 4Q/(\pi D^2)$, this can also be written as

$$Re = \frac{4\rho Q}{\pi \mu_w D}. \tag{5}$$

For low Reynolds numbers, below approximately 2300, viscous forces dominate over inertial forces and the flow remains laminar, which supports the use of Hagen–Poiseuille theory as a first approximation [90].

For a flexible channel, the hydraulic resistance is not only determined by the initial geometry and fluid viscosity. The internal pressure can deform the channel wall and increase the effective lumen diameter, as shown in Figure 14b, thereby reducing the hydraulic resistance [85]. This means that the pressure-flow relation may become nonlinear: increasing pressure increases

the driving force for flow, but may also increases the channel diameter.

A decrease in R_h with increasing mean pressure would therefore indicate expansion of the flexible channel. In this study, this principle is used to estimate the diameter change of the printed channels from the measured pressure drop and flow rate.

The pressure-induced diameter change is directly related to the compliance of the channel. In general, compliance describes the change in internal volume resulting from a change in pressure [28]:

$$C_V = \frac{\Delta V}{\Delta P}, \tag{6}$$

where C_V is the volumetric compliance, ΔV is the change in internal volume, and ΔP is the corresponding pressure change. For a cylindrical channel, an increase in diameter also corresponds to an increase in internal volume. For blood vessels, compliance is commonly characterized using the relative diameter change [11]:

$$C_D = \left(\frac{D_H - D_L}{D_L}\right) \frac{1}{P_H - P_L}, \tag{7}$$

where C_D is the diameter-based compliance, and D_H and D_L are the internal diameters corresponding to the higher and lower pressure levels P_H and P_L, respectively. A more compliant channel therefore shows a larger relative diameter increase for the same pressure increase. In this study, this behaviour is evaluated indirectly from the pressure-dependent effective diameter, rather than as a direct dynamic compliance measurement.

4. Materials and methods

4.1. Materials

Flexible channels were fabricated using Elastomer-X resin (Liqcreate, The Netherlands) [91]. This resin was selected because it is a commercially available elastomeric resin with a wavelength of 385 to 420 nm, making it compatible with a range of affordable printers such as the Elegoo Mars 5 ultra which is used for this research.

Water was used as the working fluid during the pressure-flow experiments.

4.2. Channel design and fabrication

The channel geometries were designed in SolidWorks. The channels consisted of straight cylindrical lumens with a constant wall thickness. The main design parameters were the lumen diameter, wall thickness, and channel length.

To investigate the printability limits, channels were designed with lumen diameters of 0.5, 0.7, 1.0, 2.0, 3.0, and 5.0 mm. Wall thicknesses of 0.15, 0.25, 0.50, 1.00, 1.50, and 2.50 mm were evaluated, depending on the lumen diameter. Channels with lengths of 20 mm and 30 mm were printed to evaluate the influence of channel length on fabrication and handling.

The CAD models, see Appendix A, were exported as STL files and imported into Chitubox, a slicer program for resin-based 3D printers. In Chitubox, the models were oriented vertically and support structures were added before printing. An example of the supported channel models in Chitubox is shown in Appendix B. The channels were printed using an Elegoo Mars 5 Ultra mSLA printer. This printer uses a 7-inch 9K monochrome liquid crystal display (LCD) with an XY pixel size of approximately 18 µm and a build volume of $153.36 \times 77.76 \times 165$ mm^3 [92]. Printing with high resolution (small XY pixel size) is important for this study because the channels contain small lumen diameters and thin walls, where geometrical accuracy strongly affects the final pressure-flow behaviour.

The working principle of mSLA relies on photopolymerization, where a liquid resin is selectively cured by ultraviolet (UV) light to form solid structures layer by layer [49]. A build platform is submerged from above in a vat of resin, while the light source is positioned below the resin vat. A UV Light Emitting Diodes (LED) array projects light upward through an LCD digital mask placed directly under the transparent bottom of the resin tank, where each pixel of the screen either blocks or transmits light, enabling layer-by-layer curing of the photopolymer resin. After each layer, the platform moves up vertically, allowing the next layer to be built until the full geometry is complete [16].

The layer height was set to 0.10 mm, and the standard exposure time for the main printability tests was 15 s per layer. These settings served as the baseline printing parameters for channel fabrication and were based on the Liqcreate recommendations for Elastomer-X, with small adjustments to improve the printability of small open channels [93]. The bottom layer exposure time was set to 80 s with five bottom layers to improve adhesion of the first layers to the build platform.

The channels were printed vertically, corresponding to a print orientation of 90 degrees, so that the lumen was aligned with the build direction. This orientation was chosen to reduce the need for support material inside the channel and to improve resin drainage from the lumen, since holes are generally easier to print when they are aligned with the printer's z-direction [94]. Printing the flexible channels vertically also provided a more stable configuration for these long, soft structures, while horizontal or strongly angled orientations were avoided because they could increase the risk of movement, deformation, or lumen closure during printing. In resin-based printing, the orientation of a part also influences support placement, peeling forces, and the risk of trapped resin inside hollow regions [95].

The relevant printing settings are summarized in Table 4.

4.3. Post-processing

After printing, the channels were removed manually from the build plate using a sharp blade and cleaned to remove uncured resin from both the outside and inside of the channels. The post-processing procedure is shown schematically in Figure 15, which consists of two main steps: cleaning and UV post-curing.

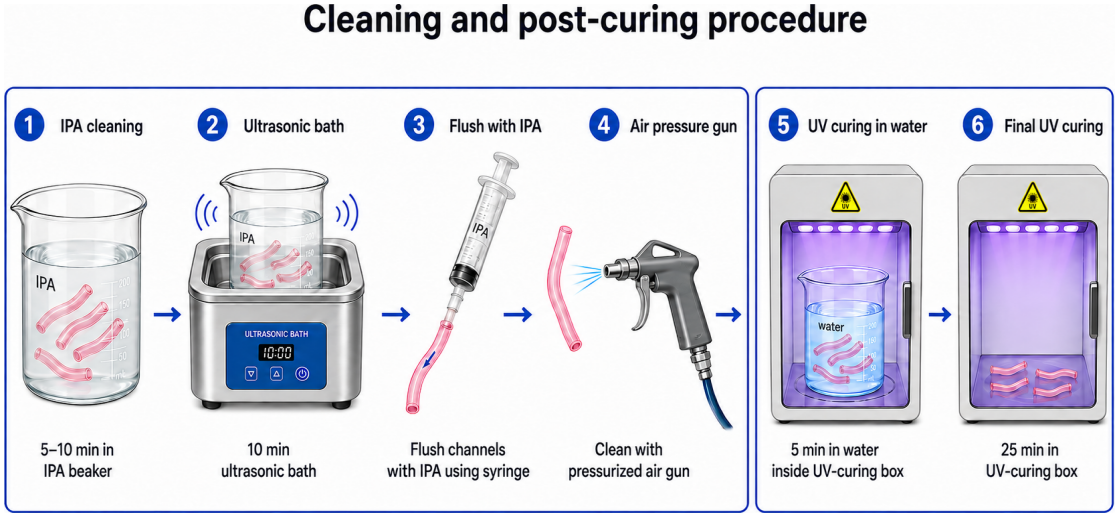

Figure 15: Schematic overview of the cleaning and post-curing procedure used after printing.

Table 4: Printing settings used for the fabrication of the flexible channels.

Parameter	Value
Printer	Elegoo Mars 5 Ultra
Resin	Liqcreate Elastomer-X
Layer height	0.10 mm
Bottom layer exposure time	80 s
Normal layer exposure time	15 s
Number of bottom layers	5
Print orientation	90 degrees (vertical)

First, the channels were placed in a beaker with isopropyl alcohol (IPA) for 5–10 min (1). IPA was used to dissolve and remove residual uncured resin from the printed surface and internal features [96]. The beaker was then placed in an ultrasonic bath for 10 min to improve cleaning of the small lumen (2). Since Liqcreate Elastomer-X can absorb IPA and temporarily swell during prolonged exposure [97], the cleaning time was kept limited. After cleaning, the supports were removed manually, taking care not to damage the flexible channels. The channels were then flushed with IPA using a syringe (3), followed by a pressurized air gun to remove residual IPA and uncured resin (4).

The channels were subsequently post-cured in a UV-curing box. First, the channels were cured for 5 min while submerged in water (5). This step was used to reduce oxygen inhibition at the surface, since oxygen can react with free radicals and inhibit the formation of polymer chains and crosslinks, resulting in a sticky or under-cured surface [98]. Afterwards, the channels were placed separately on the bottom of the UV-curing box and cured in air for an additional 25 min (6). The temperature setting of the UV-curing box was turned off, so curing was performed at room temperature. This was done to avoid an additional thermal effect during post-curing, since higher temperatures can influence the final stiffness and dimensional recovery of Elastomer-X after IPA exposure [97].

4.4. Printability and geometrical accuracy

The printability of the channels was evaluated by visually inspecting whether the lumen remained open after printing and post-processing. For each combination of lumen diameter and wall thickness, the channel was classified as open, partially open, or closed. An open channel was defined as a channel with a continuous lumen along the full length. A partially open channel was defined as a channel where the lumen was open, but showed narrowing or local irregularities. A closed channel was defined as a channel where the lumen was blocked and could not be used for flow experiments.

Based on the printability, a subset of channel geometries was selected for geometrical accuracy measurements. Three lumen diameters were selected: 0.7, 1.0, and 2.0 mm. For all three geometries, the wall thickness was kept constant at 0.25 mm. For each nominal lumen diameter, at least six channels were measured.

To evaluate the geometrical accuracy, microscopic images were taken of the printed channels using a Keyence Digital Microscope VHX-6000. For each channel, the inner diameter D, width W, and wall thickness t were measured, as shown in Figure 16. Figure 16a shows how the outer width was measured along the channel length, while Figure 16b shows how the lumen diameter and wall thickness were measured at the channel opening.

The width W, also referred to as the outer diameter, was measured at three locations along the channel length: near the inlet, near the middle, and near the outlet. This resulted in at least 18 measurement points per nominal lumen diameter for the width measurements, since at least six channels were measured for each geometry.

The inner diameter D and wall thickness t were measured at the channel openings, corresponding to $x = 0$ and $x = L$. These

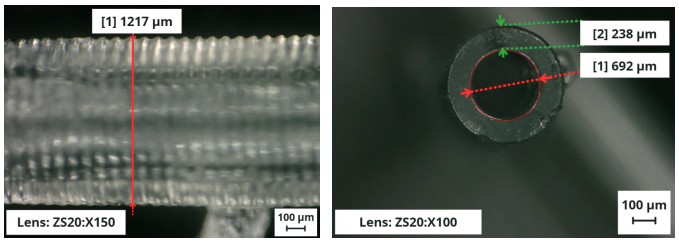

(a) (b)

Figure 16: Example microscopic images used for the geometrical accuracy measurements of the printed channels. (a) Side view of the channel, where the full width W was measured. (b) Channel opening, where the inner diameter D [1] and wall thickness t [2] were measured. Both images show a channel with a length of 20 mm, nominal inner diameter of 0.7 mm, and nominal wall thickness of 0.25 mm.

locations were selected because the inner lumen and wall thickness were directly accessible at the channel ends, while the internal geometry along the middle part of the channel could not be measured directly using microscopy. For the inner diameter, one or two measurements were taken per channel, resulting in approximately 6–9 measurement points per nominal lumen diameter. The same approach was used for the wall thickness, where one or two measurements were taken per channel, also resulting in approximately 6–9 measurement points per nominal lumen diameter.

The measured dimensions were compared with the corresponding nominal CAD values. For each measured dimension and nominal lumen diameter, the median value was calculated. The median was used because it is less sensitive to individual measurement outliers than the mean. The geometrical deviation was calculated as:

$$\delta_{\text{geom}} = \frac{|x_{\text{median}} - x_{\text{CAD}}|}{x_{\text{CAD}}} \times 100\%, \tag{8}$$

where x_{median} is the median measured dimension and x_{CAD} is the corresponding nominal CAD value. The spread of the measurements was visualized using boxplots.

In addition to the end-point measurements, the internal geometry of the channels was inspected using green ink diluted in water. The accuracy measurements described above were mainly taken at the channel openings, where the lumen boundary was directly visible. However, these measurements did not provide information about possible variations in the lumen diameter along the full channel length. Therefore, green ink was manually injected into the channels using a syringe to improve the visibility of the internal lumen under the microscope. Microscopic images were taken along the entire channel length, and several local diameter measurements were performed for each channel.

Since the channel wall was rounded and semi-transparent, the boundary between the ink-filled lumen and the surrounding channel wall was not always sharply visible. The local measurements were therefore treated as estimates rather than exact geometrical measurements. The ink-filled images were used to estimate a representative initial diameter D_{ink} for each channel. These values were used as reference values when comparing the geometrical observations with the effective diameters obtained from the pressure-flow measurements. When selecting this value, local narrowing was taken into account because the hydraulic resistance depends strongly on the lumen diameter through $R_h \propto D^{-4}$. The representative initial diameter was therefore not based only on the nominal CAD diameter or the diameter measured at the channel openings. The ink-filled-channel images and the corresponding local measurements are presented in Appendix D.

For the pressure-flow experiments, three channels were selected for each of the E_- and E_+ configurations. The selected channels were chosen from multiple printed samples based on their practical usability: they were open across their entire length and showed the least internal narrowing. Testing three channels per configuration allowed channel-to-channel variation to be evaluated for samples produced using the same fabrication and post-processing procedure. Since only the most suitable open channels were selected, this comparison evaluates the reproducibility among usable samples rather than the overall fabrication success rate.

4.5. Mechanical characterization

To characterize the stiffness of the channels, the Young's modulus of the printed material was determined using tensile tests. For these tests, strip specimens were designed in SolidWorks and printed using the same resin and printer as the channels. The printing orientation of the strips was chosen to represent the loading direction expected in the channels, as illustrated in Figure 17.

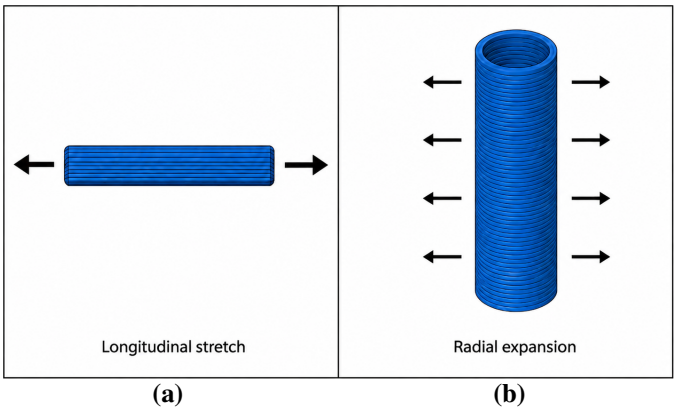

(a) **(b)**

Figure 17: Schematic representation of the loading directions relative to the printed layer structure. (a) Longitudinal stretching of the tensile-test strip. (b) Radial expansion of the vertically printed channel under internal pressure.

Figure 17(a) shows the tensile-test strip. During the tensile test, the strip was stretched along its longitudinal direction, as indicated by the arrows. The strip was printed on its side so that the tensile loading direction remained aligned with the plane of the printed layers.

Figure 17(b) shows the vertically printed channel. Because the channel was printed vertically, each printed layer formed a thin

circular cross-section around the lumen. When internal pressure was applied, the channel expanded in the radial direction. This caused the channel wall to stretch mainly in the circumferential direction, within the plane of the circular printed layers.

To represent this loading direction in the tensile tests, the strips were printed on their side, with the strip width oriented vertically during printing. In this orientation, the strip was stretched along its length during the tensile test, while the loading direction remained aligned with the plane of the printed layers, similar to the circumferential stretching of the channel wall during pressure-induced expansion. The specimen dimensions were 20 mm in length, 8 mm in width, and 2 mm in thickness.

The stiffness of the material can be adjusted by changing the amount of UV exposure. In the fabrication process used in this study, UV exposure occurs at two stages. The first stage is during printing, where each layer is exposed for a defined exposure time. The second stage is during post-curing, where the printed samples are exposed to UV light in the UV-curing box. Longer UV exposure is expected to increase the stiffness of the material due to further polymerization and crosslinking of the resin structure.

Initial tensile tests were performed to determine which processing parameter had the strongest influence on the final stiffness of the printed material. In these tests, the printer exposure time and the post-curing duration were varied separately. The tested conditions and results of these initial experiments are described in Appendix C.1.

Based on these initial tests, three representative processing conditions were selected for further comparison: E_-, E_{mid}, and E_+. The E_- configuration resulted in the lowest measured Young's modulus, while the E_+ configuration resulted in the highest measured Young's modulus. The E_{mid} configuration was included as an intermediate condition. The selected processing conditions are summarized in Table 5. The E_- and E_+ configurations were used for the pressure-flow experiments.

Table 5: Selected printing and post-curing conditions used for the tensile-test specimens.

Configuration	Printer exposure [s/layer]	UV curing in water [min]	UV curing in air [min]
E_-	10	5	0
E_{mid}	15	5	25
E_+	20	5	60

Tensile tests were performed using a DMA Q800 V21.2 Build 88 tensile testing machine. The tests were performed using the tension clamp, with the strip specimens classified as film samples. The strips were clamped in the machine and stretched using a force ramp from 2.0000 N/min up to 18.0000 N. An initial static force of 0.0100 N was applied before the force ramp. The test was continued until failure or until the maximum ramp force was reached. Stress and strain were recorded during the test.

The Young's modulus was obtained from the initial linear region of the stress-strain curve. A linear fit was applied to the initial part of the curve, where the material response was assumed to be approximately elastic.

The slope of this fitted region was used to calculate the Young's modulus of each specimen. One representative stress-strain curve with the corresponding linear fit is shown in Figure 18 as an example of the fitting procedure. The remaining tensile-test curves are shown in Appendix C.2.

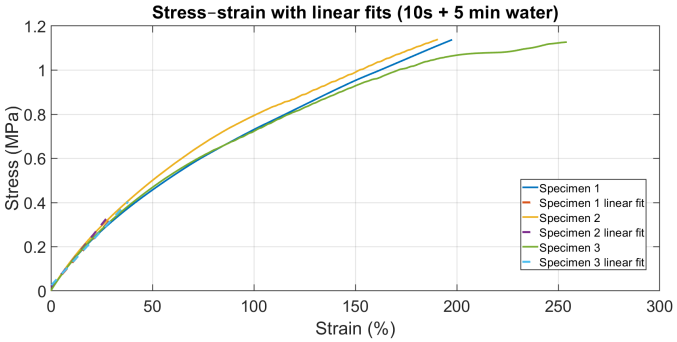

Figure 18: Example stress-strain curve with linear fit used to determine the Young's modulus. The linear fit, shown by the dotted lines, was applied to the initial region of the curves, where the material response was assumed to be approximately elastic.

The coefficient of determination, R^2, was used to evaluate how well the linear fit described the selected data points. A high R^2 value indicates that the selected region was close to linear and therefore suitable for determining the Young's modulus. The individual Young's modulus values were averaged for each processing condition, and the mean value with standard deviation is reported in the results section 5.3.

4.6. Pressure-flow experimental setup

Pressure-flow experiments were performed to investigate the diameter change of the flexible channels under pressurized flow. A schematic overview of the experimental setup is shown in Figure 19. The setup consisted of a pressure controller, pressure sensors, a flow sensor, tubing, two reservoirs, and the flexible channel placed between two connectors. The computer was connected to the pressure controller and was used to apply pressure steps. Pressurized air from the controller was supplied to the first sealed water reservoir. This pressure pushed water from the reservoir through the tubing and through the flexible channel. The second reservoir was open to the atmosphere and was used as the outlet reservoir. The ambient outlet pressure was taken as the zero-pressure reference.

Preliminary pressure-flow experiments were first performed using ElveFlow equipment to develop the experimental procedure and test the baseline-correction method. However, the uncertainty in these measurements was too large to identify a reliable pressure-dependent effective diameter trend. Therefore, the main pressure-flow analysis in this paper is based on the Fluigent measurements, while the ElveFlow setup and results are included in Appendix E.

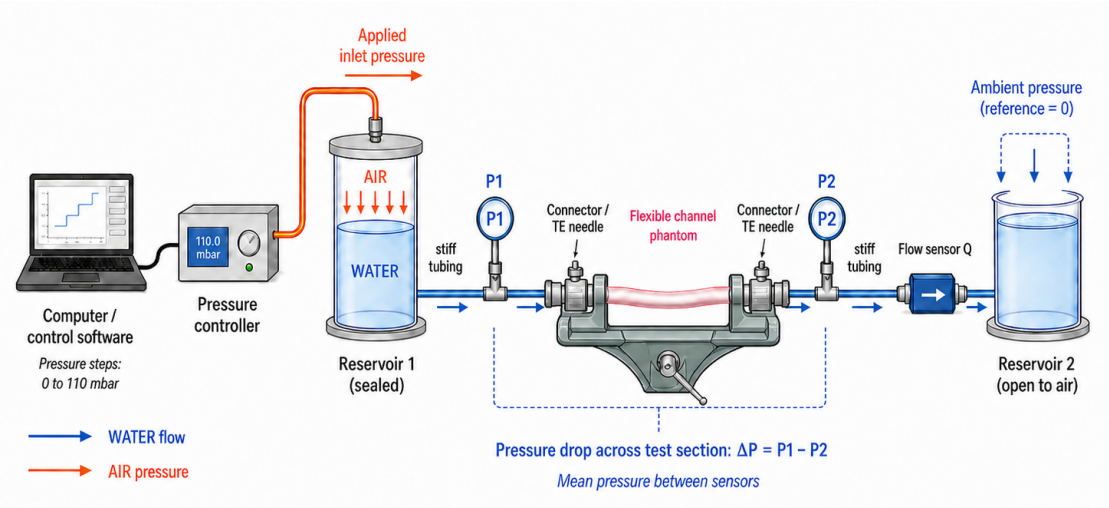

Figure 19: Schematic overview of the pressure-flow experimental setup.

The Fluigent setup was used because it allowed experiments at higher pressures and flow rates [99]. Pressure was supplied using the FLPG+ compressed air pressure source, which supplied air to the Flow-EZ pressure controller. The Flow-EZ controller (LU-FEZ-1000) can control positive pressures up to 1 bar. The pressure was measured using Fluigent pressure sensors M (EIPS1000), which have a pressure range of −1000 to 1000 mbar and an inner diameter of 500 µm. The pressure accuracy is typically 1.0–2.0% in the range of 10–20 mbar, with a zero shift of 10 mbar, corresponding to 1% of the full span. The flow rate was measured using a Fluigent flow sensor L+ (FLU-L+). For water, this sensor has a flow range of 0–40.0 mL/min, with an accuracy of 5% of the measured value above 1 mL/min and 50 µL/min below 1 mL/min. The inner diameter of this flow sensor is 1.4 mm.

The pressure drop was measured over the test section between the two pressure sensors, P_1 and P_2. This section included the stiff tubing, the two rigid connectors, and the flexible channel placed between them. The flow sensor was located after P_2, and was therefore used to measure the flow rate through the system, see Figure 19. The flexible channel was connected to the system using dispensing tips (920100-TE) with a stainless steel nozzle, which served as rigid connectors between the channel and the stiff tubing. The printed channels had a total length of 20 mm. After insertion of the rigid connectors, the effective channel length between the connector tips was approximately 17.5 mm. This effective length was used in the hydraulic-resistance-based diameter calculations. These dispensing tips have a 20 gauge nozzle with a length of 25.4 mm, corresponding to an inner diameter of 0.610 mm [100]. The connectors were fixed in place using a clamp. The clamp held the rigid connectors while leaving the flexible channel itself free to deform under pressure. The pressure sensors, flexible channel, flow sensor, and the water levels in the inlet and outlet reservoirs were positioned at approximately the same height. Therefore, height differences in the setup were considered negligible, and the influence of hydrostatic pressure was assumed to be minimal.

Because the channels were flexible and had thin walls, the connection to the rigid dispensing tips could introduce additional variation between measurements. Slight differences in connector alignment or insertion depth may cause local deformation near the channel ends, while small misalignments may result in bending of the channel between the connectors. These effects may locally influence the lumen geometry and introduce pressure losses that are not fully removed by the baseline correction. Care was therefore taken to align the connectors and handle the channels consistently during each experiment.

The stiff tubing had an inner diameter of 0.800 mm, with a total tubing length of 90 mm between P_1 and P_2. The tested channels had a lumen diameter of 0.7 mm, wall thickness of 0.25 mm, and length of 20 mm. The main components and measurement settings of the Fluigent setup are summarized in Table 6.

Table 6: Main components and settings of the Fluigent pressure-flow setup.

Component	Specification
Pressure source	Fluigent FLPG+
Pressure controller	Flow-EZ (LU-FEZ-1000)
Pressure sensors	Sensor M (EIPS1000)
Flow sensor	Flow sensor L+ (FLU-L+)
Working fluid	Water
Applied pressure range	0–300 mbar
Pressure step size	30 mbar
Step duration	Approximately 10 s

4.7. Pressure-flow measurement protocol

For each experiment, the system was first filled with water and checked for leakage and air bubbles. Special care was taken to remove air bubbles from the tubing, sensors, connectors, and flexible channel, since trapped air could influence the measured pressure-flow response.

For the Fluigent measurements, the applied inlet pressure was increased stepwise from 0 to 300 mbar in steps of 30 mbar. The higher pressure range of the Fluigent setup was used to increase the measurable deformation range of the flexible channels. Each pressure step was applied for approximately 10 s, allowing the pressure and flow signals to reach a steady state before the data were averaged.

At each pressure step, the upstream pressure P_1, downstream pressure P_2, and flow rate Q were recorded. Examples of the raw P_1 and Q signals as functions of time are shown in Figure 20. The graphs illustrate the stepwise pressure protocol used during the Fluigent measurements and the corresponding increase in flow rate.

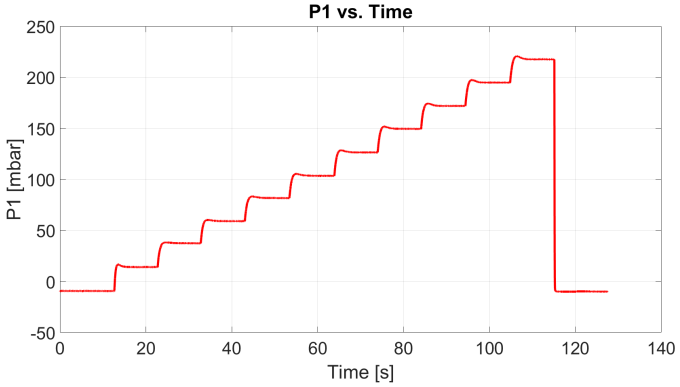

(a) Pressure P_1 as a function of time.

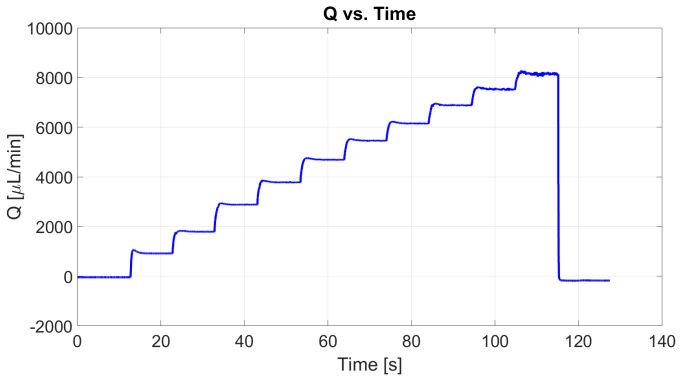

(b) Flow rate Q as a function of time.

Figure 20: Example raw signals measured during a Fluigent pressure-flow experiment. (a) The applied pressure was increased stepwise. (b) The flow rate increased accordingly. Where the stable part of each pressure step was used for data processing

The pressure drop over the test section was calculated using $\Delta P = P_1 - P_2$, as defined in Section 3. The mean pressure between P_1 and P_2, referred to as P_{mean}, was used to approximate the transmural pressure acting on the channel wall. The transmural pressure is the pressure difference between the fluid inside the channel and the pressure outside the channel. Since the outside of the channel was exposed to atmospheric pressure, P_{mean} was used as an estimate of this pressure difference.

Baseline measurements were performed using the same pressure-flow setup configuration, but without the flexible channel connected. For these measurements, the two rigid connectors were connected directly to each other using a short piece of flexible tubing. Both connectors were inserted from opposite sides of this tube until their tips touched, creating a sealed connection and keeping the connectors fixed in place. In this way, the complete setup remained the same, except for the absence of the flexible channel. These baseline measurements were used to quantify the pressure losses caused by the setup itself, including the stiff tubing and connectors. Channel measurements were then performed with the flexible channel connected between the two rigid connectors. By comparing the baseline and channel measurements at corresponding flow rates, the pressure drop contribution of the flexible channel could be isolated.

The same pressure-flow procedure was repeated three times for each channel. A corresponding baseline measurement was used for each run to correct for the pressure losses in the setup. These repeated measurements were used to assess the run-to-run repeatability of the experiment separately from the channel-to-channel variation between fabricated samples.

4.8. Data processing

The raw pressure and flow data were imported and processed in MATLAB. The Fluigent data were exported as CSV files. The pressure steps were detected from the applied pressure signal. For each pressure step, the last 4 s of the step were selected as the stable window. This window was used to exclude the transient response directly after a pressure change and to calculate representative steady-state values. As shown in Figure 20, the pressure and flow signals generally became more stable towards the end of each step. Within this window, the mean values and standard deviations of P_1, P_2, and Q were calculated for each pressure step.

Before further processing, the measured pressure and flow values were shifted by subtracting the first measured value. This removed the initial sensor offset and made the first pressure step start from zero. The pressure drop was then calculated from the shifted pressure values. The standard deviation of the pressure drop was estimated by error propagation:

$$\sigma_{\Delta P} = \sqrt{\sigma_{P_1}^2 + \sigma_{P_2}^2}. \tag{9}$$

The same processing steps were applied to both the baseline measurements and the measurements with the flexible channel. To correct for pressure losses in the setup, the baseline pressure drop was subtracted from the pressure drop measured with the flexible channel. Since the baseline and channel measurements were not always obtained at exactly the same flow rate, a polynomial fit was first applied to the baseline pressure-drop data as a function of flow rate. This fit was then evaluated at the flow rates measured during the channel experiment, so that the baseline correction was performed at matched flow rates. The channel-only pressure drop was calculated as

$$\Delta P_{\text{channel}}(Q) = \Delta P_{\text{total}}(Q) - \Delta P_{\text{baseline}}(Q). \tag{10}$$

The channel-only hydraulic resistance was calculated using the

definition introduced in Section 3:

$$R_{\mathrm{h,channel}} = \frac{\Delta P_{\mathrm{channel}}}{Q}. \tag{11}$$

The uncertainty in hydraulic resistance was estimated using standard uncertainty propagation for a quotient, where the relative uncertainty of the result is calculated from the root-sum-square of the relative uncertainties of the numerator and denominator [101]:

$$\sigma_{R_{\mathrm{h}}} = \left|R_{\mathrm{h,channel}}\right| \sqrt{\left(\frac{\sigma_{\Delta P_{\mathrm{channel}}}}{\Delta P_{\mathrm{channel}}}\right)^2 + \left(\frac{\sigma_Q}{Q}\right)^2}. \tag{12}$$

Only data points with positive flow rate and positive corrected pressure drop were used for the diameter calculation, to avoid division by zero or non-physical diameter values. The effective diameter was then estimated from the channel-only hydraulic resistance using the Hagen–Poiseuille relation described in Section 3. The corresponding standard deviation of the effective diameter was calculated from the relation $D_{\mathrm{eff}} \propto R_{\mathrm{h}}^{-1/4}$:

$$\sigma_{D_{\mathrm{eff}}} = |D_{\mathrm{eff}}| \, \frac{1}{4} \left| \frac{\sigma_{R_{\mathrm{h}}}}{R_{\mathrm{h,channel}}} \right|. \tag{13}$$

The hydraulic resistance and effective diameter were plotted as a function of the P_{mean}. A decrease in hydraulic resistance with increasing mean pressure was interpreted as an indication of pressure-induced channel expansion. Finally, the relative diameter was calculated by normalizing the effective diameter with respect to the first valid diameter value of each channel:

$$\frac{D}{D_0} = \frac{D_{\mathrm{eff}}}{D_{\mathrm{eff},0}}. \tag{14}$$

The mean pressure was shifted in the same way, so that the first valid data point started at zero mean pressure. This relative diameter representation was used to compare the diameter change between different channels and stiffness configurations. The experimental effective diameter was then compared with the initial diameter, referred to as the stiff channel, to evaluate how the channel diameter changed relative to its original state.

5. Results and discussion

5.1. Printability of flexible channels

The printability results show which channel geometries could be fabricated reliably. Table 7 summarizes the printability results for the tested lumen diameters and wall thicknesses. The rows indicate the nominal lumen diameter, while the columns indicate the wall thickness.

The smallest tested lumen diameter of 0.5 mm could not be printed as an open channel for any of the tested wall thicknesses. This indicates that, for this printer-material combination and the selected printing parameters, the lumen became blocked at this scale. For a lumen diameter of 0.7 mm, the channels with a wall thickness of 0.15 mm and 0.50 mm showed local narrowing or irregularities, while the 0.25 mm wall thickness resulted in a consistently open channel with a continuous lumen. For larger lumen diameters, such as 1.0, 2.0, and 3.0 mm, more combinations could be printed successfully. This is expected because a larger lumen is less likely to close during printing, cleaning, and post-curing.

Table 7: Printability overview as function of lumen diameter and wall thickness. O = open and C = closed. Green indicates channels that were consistently open with a continuous lumen, orange indicates channels that were partially open but showed narrowing or local irregularities, and red indicates closed channels.

Diameter (mm) \ Thickness (mm)	0.15	0.25	0.50	1.00	1.50	2.50
0.5	C	C	C	–	–	–
0.7	O	O	O	C	–	–
1.0	O	O	O	C	–	–
2.0	O	O	O	O	–	–
3.0	O	O	O	O	O	–
5.0	–	–	–	–	–	O

Channel length also influenced the practical fabrication and handling of the samples. Channels with a length of 30 mm were more difficult to fabricate reliably than channels with a length of 20 mm. A likely explanation is that longer and more flexible channels are less stable during printing. When the build platform moves between layers, or when the printed layer separates from the film at the bottom of the resin vat, the unsupported part of the channel may slightly deflect. This can disturb the layer alignment and reduce the straightness of the printed channel. Shorter channels with a length of 20 mm were therefore easier to keep straight, open, and suitable for pressure-flow experiments.

Based on the printability results, a lumen diameter of 0.7 mm, a wall thickness of 0.25 mm, and a length of 20 mm were identified as the smallest channel geometry that remained consistently open and could still be handled and connected to the experimental setup. However, printability alone does not show whether the printed dimensions are sufficiently close to the CAD design. Therefore, geometrical accuracy measurements were performed before selecting the final geometry for the pressure-flow experiments. In addition to the 0.7 mm channels, larger open channels were also measured to compare the printing accuracy across different lumen sizes and to provide reference geometries.

5.2. Geometrical accuracy

Based on the printability results, three nominal lumen diameters were selected for geometrical accuracy measurements: 0.7, 1.0, and 2.0 mm. These were chosen as the three smallest lumen diameters that could be printed as open channels, excluding the 0.5 mm channels, which were closed for all tested wall thicknesses. The 0.7 mm channels were measured to determine whether the smallest open geometry was also printed accurately enough for flow experiments, while the 1.0 and 2.0 mm channels were included as larger reference geometries to evaluate how the dimensional accuracy changed with lumen size. For all three selected lumen diameters, the nominal wall thickness was fixed at 0.25 mm, because this wall thickness gave the most

consistent open channels among the tested small-diameter geometries.

The geometrical accuracy was evaluated by comparing the measured lumen diameter, width, and wall thickness with the corresponding nominal CAD values, as shown in Figure 21. In each boxplot, the red line represents the median measured value, while the box and whiskers show the spread of the measurements. The median was used as the central value because it is less sensitive to individual measurement outliers than the mean.

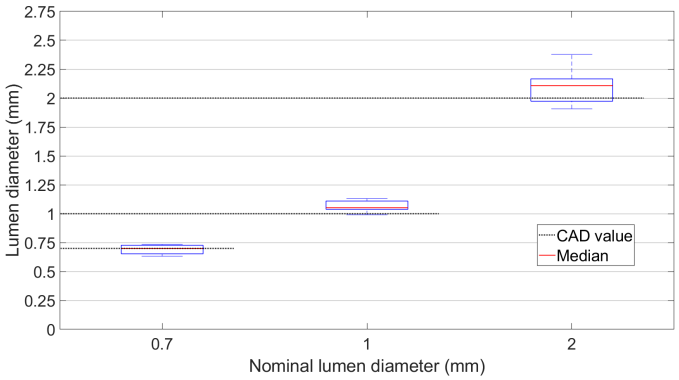

(a) Lumen diameter

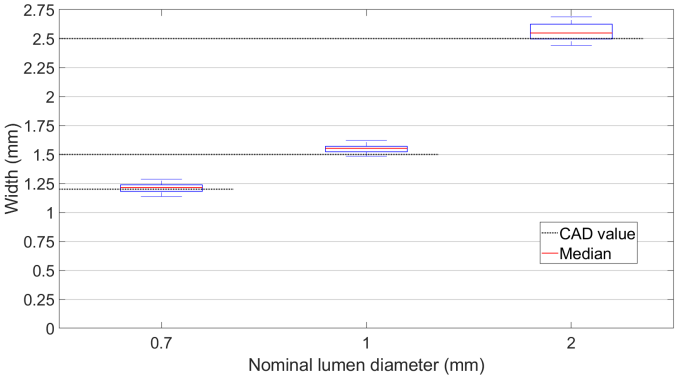

(b) Width

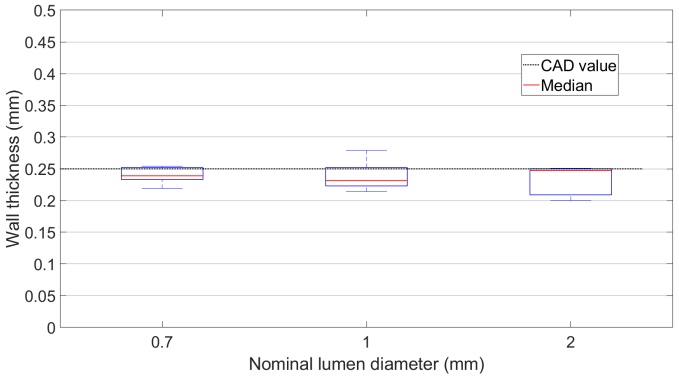

(c) Wall thickness

Figure 21: Geometrical accuracy of the printed channels compared with the nominal CAD values: (a) lumen diameter, (b) width, and (c) wall thickness. The dimensions were measured for channels with nominal lumen diameters of 0.7, 1.0, and 2.0 mm. The dotted black lines indicate the corresponding CAD values, and the red lines indicate the median measured values.

The median measured values and the corresponding deviations from the CAD dimensions are summarized in Table 8. For all investigated geometries and dimensions, the median deviation remained below the target value of 10% defined in the approach.

Table 8: Median measured dimensions and deviations from the corresponding nominal CAD values.

Measurement	Nominal lumen diameter [mm]	CAD value [mm]	Median value [mm]	Deviation [%]
Lumen diameter	0.7	0.700	0.691	1.30
Outer width	0.7	1.200	1.214	1.17
Wall thickness	0.7	0.250	0.239	4.40
Lumen diameter	1.0	1.000	1.052	5.20
Outer width	1.0	1.500	1.553	3.50
Wall thickness	1.0	0.250	0.232	7.40
Lumen diameter	2.0	2.000	2.107	5.35
Outer width	2.0	2.500	2.548	1.92
Wall thickness	2.0	0.250	0.248	1.00

The largest deviation was 7.4%, which was observed for the wall thickness of the channels with a nominal lumen diameter of 1.0 mm. For the smallest printable channels with a nominal lumen diameter of 0.7 mm, the median lumen diameter was 0.691 mm, corresponding to a deviation of 1.30%. The median outer width and wall thickness of these channels deviated by 1.17% and 4.4%, respectively.

Small deviations from the CAD values are expected in resin-based printing. Possible causes include overcuring due to light scattering, resin shrinkage, cleaning, post-curing, and manual measurement uncertainty from the microscope images. In particular, unintended curing of resin inside the lumen may cause local narrowing or partial closure of the channel. A channel may therefore appear open and geometrically accurate at its inlet and outlet while still containing narrower sections along its internal length. This is important for the pressure-flow experiments, since local narrowing strongly affects the hydraulic resistance through the fourth-power dependence $R_h \propto D^{-4}$.

Although the dimensions measured at the channel openings met the geometrical-deviation target, these measurements do not necessarily represent the lumen diameter along the full internal length of the channel. The ink-filled-channel images showed that the lumen diameter was not constant along the full channel length. The E_- configuration channels, channels 1–3, also referred to as the exp10 channels, generally showed a more consistent internal lumen diameter close to the nominal value of 0.7 mm. In contrast, the E_+ configuration channels, channels 4–6, also referred to as the exp20 channels, showed more local narrowing. This was especially visible for channels 5 and 6.

Representative examples are shown in Figure 22, while the images of all six channels are provided in Appendix D. Channels 3 and 5 were selected as representative examples because they clearly illustrate the difference between the two configurations. Channel 3 shows a relatively consistent lumen diameter along the channel length, whereas channel 5 shows more local narrowing. The green ink improves the visibility of the lumen, and the red markers indicate the locations where the local lumen

Table 9: Young's modulus values (in MPa) obtained from the linear fits of the tensile-test specimens.

Configuration	Specimen 1	Specimen 2	Specimen 3	Mean ± SD	R^2 range
10 s + 5 min water	1.040	1.135	0.999	1.058 ± 0.070	0.9927–0.9952
15 s + 5 min water + 25 min air	1.197	1.034	1.165	1.132 ± 0.086	0.9909–0.9950
20 s + 5 min water + 60 min air	1.245	1.253	1.236	1.245 ± 0.008	0.9954–0.9962

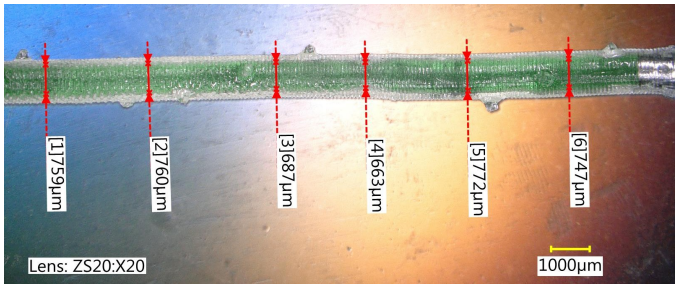

(a) Channel 3, E_- configuration

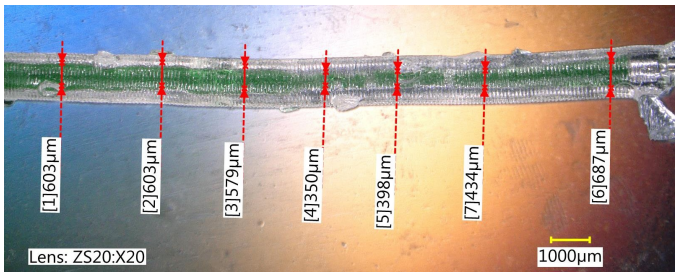

(b) Channel 5, E_+ configuration

Figure 22: Representative microscope images of ink-filled channels used to inspect the internal lumen geometry. Channel 3 shows a relatively consistent lumen diameter, while channel 5 shows more local narrowing. The red markers indicate the locations where the local lumen diameter was measured.

diameter was measured.

Based on these measurements, representative initial diameters D_0 were selected for the pressure-flow analysis. A value of approximately 0.7 mm was used for channels 1–3, approximately 0.6 mm for channel 4, and approximately 0.5 mm for channels 5 and 6. These values should be interpreted as estimates rather than exact mean diameters. Local narrowing was taken into account because narrower sections have a relatively large influence on the total hydraulic resistance due to the fourth-power dependence on diameter. The selected values were used as constant reference diameters for comparison with the pressure-dependent effective diameters calculated from the hydraulic resistance.

Overall, the geometrical accuracy results show that channels with a nominal lumen diameter of 0.7 mm and a wall thickness of 0.25 mm met the geometrical-deviation target at the channel openings and were suitable for the pressure-flow experiments. However, the internal lumen diameter could differ from the nominal value and from the edge measurements, especially for the E_+ channels.

5.3. Mechanical properties

The mechanical characterization was performed to determine the Young's modulus of the printed Elastomer-X material after printing and post-curing. This is important because the pressure-induced expansion of a flexible channel depends strongly on the stiffness of the channel wall. Elastomer-X was selected because it is a flexible elastomeric resin that can deform under pressure, while its stiffness can be adjusted by changing the printer exposure time and UV post-curing duration. Its reported Young's modulus of approximately 1.5 MPa [91] is within the same order of magnitude as human arteries, where healthy arteries typically have Young's moduli of approximately 0.2–1.0 MPa [11], while severely diseased vessels can reach values up to approximately 3.8 MPa [6]. Therefore, tuning the stiffness of the printed material is relevant for the development of compliant vascular phantoms.

Before selecting the final stiffness configurations, the influence of printer exposure time and UV post-curing time was investigated separately. These results are shown in Appendix C.3. Changing the printer exposure time from 10 s to 20 s per layer, while keeping the post-curing procedure constant, resulted in only a small difference in Young's modulus. In contrast, increasing the post-curing time resulted in a larger increase in mean Young's modulus. However, because the error bars still overlapped, the influence of each parameter separately could not be concluded with certainty. For this reason, the final E_-, E_{mid}, and E_+ configurations were selected by combining both printer exposure time and post-curing duration.

The Young's modulus values were obtained from the slope of the linear fits applied to the initial elastic region of the stress-strain curves, as described in Section 4.5. Table 9 summarizes the Young's modulus obtained for each specimen, together with the mean value, standard deviation, and coefficient of determination R^2.

Figure 23 shows the results of the Young's modulus values with their error bars. The lower-modulus E_- configuration, corresponding to 10 s printer exposure and 5 min post-curing in water, resulted in a mean Young's modulus of 1.058 ± 0.070 MPa. The medium-modulus E_{mid} configuration, with 15 s printer exposure and 5 min curing in water followed by 25 min in air, resulted in 1.132 ± 0.086 MPa. The higher-modulus E_+ configuration, with 20 s printer exposure and 5 min curing in water followed by 60 min in air, resulted in 1.245 ± 0.008 MPa. The R^2 values were high for all specimens, ranging from 0.9909 to 0.9962, indicating that the selected fitting regions were close to linear. This supports the use of the fitted slopes to determine

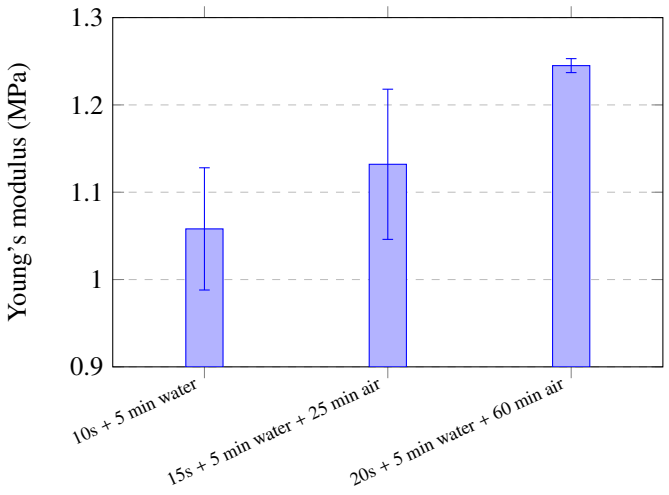

Figure 23: Young's modulus of Elastomer-X for three selected printing and post-curing conditions. The E_-, E_{mid}, and E_+ configurations were obtained by changing the printer exposure time and UV post-curing duration. Error bars indicate the standard deviation between specimens.

the Young's modulus of the printed Elastomer-X specimens.

The results show that increasing the total UV exposure generally increased the Young's modulus of the printed material. This is consistent with the expected effect of additional polymerization and crosslinking during exposure and post-curing. However, the E_{mid} configuration overlapped with the E_- configuration within the standard deviation. Therefore, the E_{mid} condition was not used for the final pressure-flow comparison. Instead, the E_- and E_+ configurations were selected because they represented the lower and upper stiffness range obtained in this study. The channels fabricated using these two processing conditions are referred to as the E_- and E_+ channels, respectively.

5.4. Pressure-flow behaviour

The pressure-flow measurements were first evaluated to check whether the experimental data behaved consistently before converting the results to hydraulic resistance and effective diameter. Water was used as the working fluid because the aim of the experiments was to evaluate the functionality and pressure-induced compliance of the printed channels. Mimicking the full rheological behaviour of blood was therefore not required at this stage. In addition, no optical matching or particle seeding was required, because the experiments were based on pressure and flow measurements rather than particle image velocimetry.

The Reynolds number was calculated for the applied flow rates to verify that the experiments remained in the laminar regime. For the Fluigent measurements, the Reynolds number was approximately $Re \approx 250$, which is well below the commonly used critical value of $Re = 2300$ discussed in Section 3. This confirms that the laminar-flow assumption used for the hydraulic resistance and effective diameter calculations was appropriate. The Reynolds number calculation is shown in Appendix F.

For each channel, both baseline measurements and channel measurements were performed. The baseline measurement represented the pressure loss of the setup without the flexible channel, while the channel measurement represented the pressure loss of the same setup with the flexible channel connected between the rigid connectors. By subtracting the baseline pressure drop at matched flow rates, the pressure drop contribution of the flexible channel could be isolated.

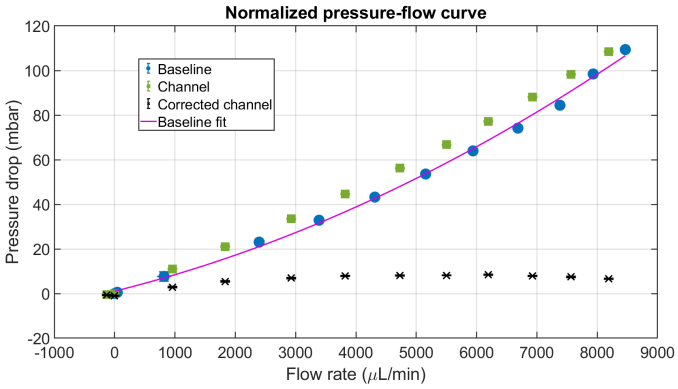

Figure 24: Example pressure-flow response measured with the Fluigent setup. The baseline measurement (blue dots) represents the pressure loss of the setup without the flexible channel, while the channel measurement (green squares) represents the pressure loss with the flexible channel included. The corrected channel data (black cross) show the pressure-drop contribution of the flexible channel after baseline correction.

An example pressure-flow measurement is shown in Figure 24. The baseline pressure drop increased with flow rate, as expected for the stiff tubing and rigid connectors in the setup. The measurement with the flexible channel showed a larger total pressure drop than the baseline at the same flow rate, because the channel introduced additional hydraulic resistance. After baseline correction, the corrected channel data represent the pressure drop over the flexible channel only. This corrected pressure drop was used as input for the hydraulic resistance and effective diameter calculations.

The pressure-flow response was not perfectly linear over the full range. This can be explained by a combination of measurement noise, minor remaining air bubbles, connector losses, and pressure-induced deformation of the flexible channel. For a purely rigid channel, a more linear pressure-flow relation would be expected. For a flexible channel, however, the effective diameter can increase with pressure, which changes the hydraulic resistance and can make the pressure-flow response nonlinear.

As described in Section 4.6, the main pressure-flow analysis focuses on the Fluigent measurements. The preliminary ElveFlow results are included in Appendix E.

5.5. Hydraulic resistance and effective diameter change

The corrected pressure-flow data were used to calculate the channel-only hydraulic resistance. According to the theory in Section 3, the hydraulic resistance is strongly dependent on the channel diameter, since R_{h} scales with D^{-4}. Therefore, if the

flexible channel expands under pressure, the hydraulic resistance is expected to decrease. This makes the hydraulic resistance a useful intermediate result before calculating the effective diameter.

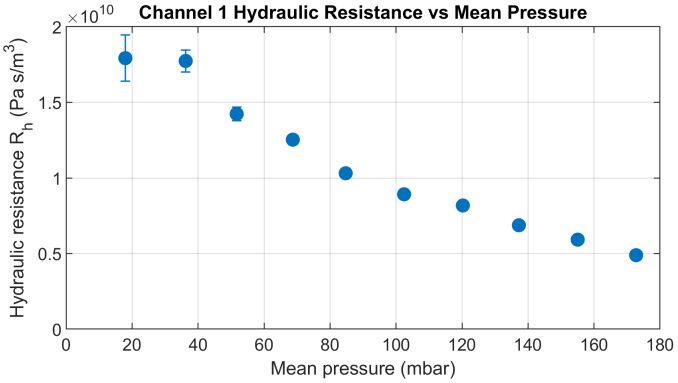

Figure 25: Hydraulic resistance R_h as a function of mean pressure for channel 1. The decrease in hydraulic resistance with increasing mean pressure indicates an increase in effective channel diameter.

Figure 25 shows the hydraulic resistance of channel 1 as a function of mean pressure. The hydraulic resistance decreases with increasing mean pressure, which is consistent with pressure-induced expansion of the channel. The same trend was observed for several other channels, as shown in Appendix G. Channels 2, 3, and 4 also showed a decreasing hydraulic resistance with pressure, although the magnitude differed between channels. Channel 6 showed only a small decrease and became almost constant at higher pressures. Channel 5 showed an increasing hydraulic resistance, which is not expected for an expanding channel and may indicate local narrowing or another channel-specific defect.

The E_- channels generally showed a stronger decrease in hydraulic resistance than the E_+ channels. This is consistent with the mechanical characterization results, where the E_- configuration had a lower Young's modulus. A lower stiffness allows the channel wall to deform more under the same pressure, which should increase the effective lumen diameter and reduce the hydraulic resistance. However, the channel-to-channel variation was considerable, showing that the final pressure-flow response was also influenced by the printed geometry and local internal channel shape.

The hydraulic resistance was then converted to effective diameter using the Hagen–Poiseuille relation. The term effective diameter is used because the diameter was not measured directly during pressurization. Instead, it was calculated from the measured pressure drop and flow rate using the mean pressure along the channel. Therefore, the extracted value represents an equivalent diameter that would give the same hydraulic resistance under the assumptions of the model, rather than the exact local diameter at each position along the channel. The effective diameter results for the individual channels are shown in Appendix H.

To compare channels with different initial effective diameters, the diameter was normalized by the initial value D_0. This gives the relative effective diameter D/D_0. A value of $D/D_0 = 1$ represents no diameter change, while values above 1 indicate expansion relative to the initial effective diameter.

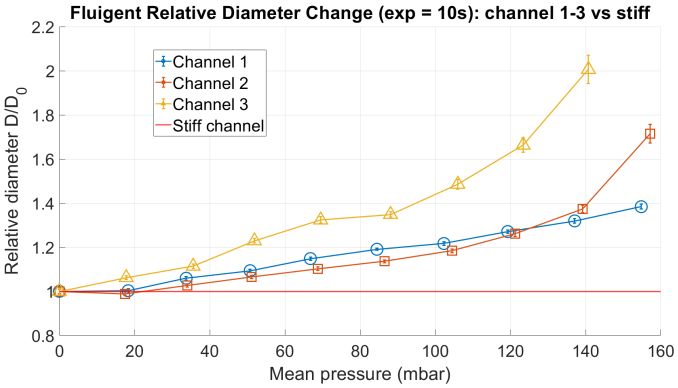

Figure 26: Relative effective diameter change of the E_- channels measured with the Fluigent setup. The relative effective diameter D/D_0 is shown as a function of mean pressure for three channels. The rigid-channel reference (red horizontal line) is included for comparison.

Figure 26 shows the relative effective diameter of the three E_- channels as a function of mean pressure. The rigid-channel reference remains at $D/D_0 = 1$, while the measured flexible channels increase above this value. All three channels show an increasing trend, indicating that the effective diameter increased with pressure. This supports the hypothesis that the printed flexible channels expand under pressure-flow conditions. The magnitude of the expansion differed between channels. Channel 1 showed a gradual increase, while channels 2 and 3 showed a stronger increase at higher pressures. This spread can be explained by small differences in printed geometry, local narrowing, internal surface irregularities, post-processing differences, or uncertainty introduced by the baseline correction. Because the effective diameter was calculated indirectly from hydraulic resistance, small variations in pressure drop or flow rate can result in relatively large changes in the calculated diameter. In addition, the ink-filled-channel images showed that the lumen was not perfectly uniform along the channel length. Since locally narrowed sections contribute strongly to the total hydraulic resistance, small fabrication-induced irregularities may partly explain the differences in effective diameter between channels.

For the main comparison between the E_- and E_+ configurations, the E_+ channel with the clearest decreasing hydraulic-resistance trend was used. The other E_+ channels showed stronger internal narrowing or an almost constant effective diameter, as shown in Appendix H. These channels were therefore not considered representative of the intended pressure-induced expansion behaviour.

Figure 27 compares the mean relative effective diameter of the E_- channels with the E_+ channel. The E_- channels showed a larger increase in relative effective diameter than the E_+ channel. This agrees with the tensile-test results, where the E_- specimens had a lower Young's modulus than the E_+ specimens. The lower stiffness allows larger pressure-induced deformation,

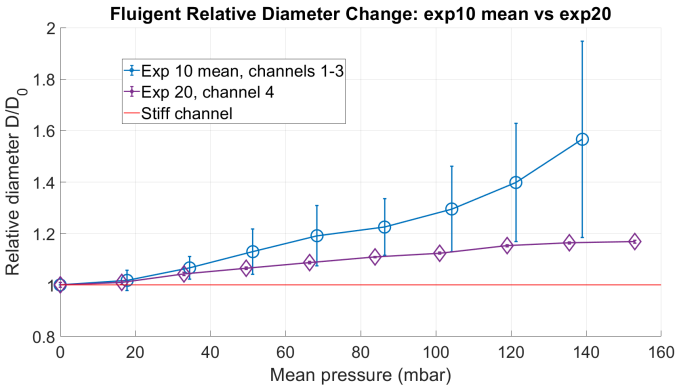

Figure 27: Comparison between the mean relative effective diameter change of the E_- channels and the E_+ channel. The E_- (exp10) channels (in blue) represent the softer configuration, while the E_+ (exp20) channel (in purple) represents the stiffer configuration. The rigid-channel reference (red horizontal line) is included for comparison.

while the stiffer channel shows a smaller and more gradual increase.

Additional repeated measurements are shown in Appendix I. These repeated runs show that the increasing relative effective diameter trend is present in several measurements, but the exact magnitude differs between runs. This means that the pressure-induced expansion trend is reproducible in a qualitative sense, but the quantitative value of the effective diameter change still has considerable uncertainty. This uncertainty is likely caused by channel-to-channel differences, local defects, measurement noise, remaining air bubbles, and the sensitivity of the hydraulic-resistance-based diameter calculation.

Overall, the relative effective diameter plots form the main functional result of this study. They show that small flexible channels printed from Elastomer-X can exhibit pressure-induced expansion under flow conditions. The comparison between E_- and E_+ further shows that the material stiffness influences the measured response, with the softer configuration showing a larger increase in relative effective diameter than the stiffer configuration.

6. Conclusion

This study investigated the fabrication and experimental characterisation of small-scale flexible vascular phantoms using mSLA 3D printing. The aim was to develop a method for printing small open flexible channels with adjustable stiffness and to evaluate whether their pressure-dependent behaviour could be measured under flow conditions.

The printability experiments showed that the smallest consistently open and practically usable channel geometry had a lumen diameter of 0.7 mm, a wall thickness of 0.25 mm, and a channel length of 20 mm. This shows that the requirement of fabricating open sub-millimetre channels was met. Smaller channels with a lumen diameter of 0.5 mm could not be printed open with the selected printer, resin, and process settings. The geometrical accuracy measurements showed that the median deviations at the channel openings remained below 10% relative to the nominal CAD dimensions. However, inspection with ink-filled channels showed that the internal lumen diameter could be smaller along the channel length. This was especially visible for the E_+ channels, where the internal lumen showed more narrowing. In contrast, the E_- channels were easier to fabricate reliably and showed a more consistent internal lumen diameter along the channel length. This indicates that increasing the printer exposure time and post-curing duration can increase stiffness, but may also make it more difficult to obtain geometrically consistent flexible channels.

The mechanical characterisation showed that the stiffness of the printed Elastomer-X material could be adjusted by changing the printer exposure time and UV post-curing duration. The selected E_-, E_{mid}, and E_+ configurations resulted in Young's moduli of 1.058 ± 0.070 MPa, 1.132 ± 0.086 MPa, and 1.245 ± 0.008 MPa, respectively. All three values fall within the vascular-relevant stiffness range. Although the differences between the configurations were relatively small, the E_- and E_+ configurations allowed a preliminary comparison of the influence of stiffness on the pressure-flow response.

The pressure-flow experiments showed that the hydraulic resistance decreased with increasing mean pressure for several channels. This trend corresponds to an increase in effective diameter, as calculated from the Hagen–Poiseuille relation. The E_- channels generally showed a larger relative effective diameter increase than the selected E_+ channel, which is consistent with the lower measured Young's modulus of the E_- configuration. However, the results differed between channels, and only one E_+ channel was suitable for comparison in this specific case. Therefore, the difference between the E_- and E_+ channels should be considered an initial observation rather than a final conclusion.

These results indicate that the printed flexible channels can deform under pressure-driven flow and that this deformation can be detected indirectly from pressure and flow measurements.

However, the calculated diameter should be interpreted as an effective diameter rather than the actual local channel diameter. The diameter was obtained indirectly from hydraulic resistance using the mean pressure along the channel, and is therefore sensitive to measurement noise, baseline correction, local lumen narrowing, remaining air bubbles, and small channel-to-channel differences. Repeated measurements showed that the increasing relative effective diameter trend was visible in several runs, but the exact magnitude varied. Therefore, the results provide qualitative and partly quantitative evidence of pressure-induced expansion, but not yet a precise measurement of the local diameter change.

Overall, this work demonstrates that mSLA 3D printing can be used to fabricate open sub-millimetre flexible channels with adjustable stiffness and measurable pressure-dependent behaviour. The main contribution is the development of an experimental fabrication and characterization workflow that combines printability testing, geometrical inspection, tensile characterization,

and pressure-flow measurements for small compliant vascular phantoms. The results also reveal an important trade-off: increasing the stiffness through the fabrication and post-curing conditions may reduce the consistency of the internal lumen geometry.

This provides a step towards vascular phantoms that reproduce not only vessel geometry, but also pressure-dependent wall deformation. Such compliant models are relevant for controlled in vitro studies of vascular pressure-flow behaviour and, after further development towards more complex geometries, could support medical-device evaluation and procedural training [33, 28, 7]. This research should be interpreted as an initial validation step, since the effective diameter change was estimated indirectly and considerable channel-to-channel variation remains.

Future work should focus on improving the internal lumen consistency and directly validating the pressure-induced diameter change using optical measurements at multiple positions along the channel length. This would provide insight into local deformation and allow a direct pressure–diameter relation and compliance value to be determined. The optically measured diameter change should be compared with the effective diameter obtained from the hydraulic resistance and with predictions from a suitable analytical or numerical model. This would show whether the measured channel expansion is of the theoretically expected order of magnitude. The method could subsequently be extended towards more complex and patient-specific vascular geometries.

References

[1] R. Tino, A. Yeo, M. Leary, M. Brandt, and T. Kron, "A Systematic Review on 3D-Printed Imaging and Dosimetry Phantoms in Radiation Therapy," *Technology in Cancer Research & Treatment*, vol. 18, p. 1533033819870208, Jan. 2019. [Online]. Available: https://journals.sagepub.com/doi/10.1177/1533033819870208

[2] R. Gharleghi, C. A. Dessalles, R. Lal, S. McCraith, K. Sarathy, N. Jepson, J. Otton, A. I. Barakat, and S. Beier, "3D Printing for Cardiovascular Applications: From End-to-End Processes to Emerging Developments," *Annals of Biomedical Engineering*, vol. 49, no. 7, pp. 1598–1618, Jul. 2021. [Online]. Available: https://link.springer.com/10.1007/s10439-021-02784-1

[3] M. Wegner and D. Krause, "3D printed phantoms for medical imaging: recent developments and challenges," *Journal of Mechanical Science and Technology*, vol. 38, no. 9, pp. 4537–4543, Sep. 2024. [Online]. Available: https://link.springer.com/10.1007/s12206-024-2407-8

[4] Z. Jin, Y. Li, K. Yu, L. Liu, J. Fu, X. Yao, A. Zhang, and Y. He, "3D Printing of Physical Organ Models: Recent Developments and Challenges," *Advanced Science*, vol. 8, no. 17, p. 2101394, Sep. 2021. [Online]. Available: https://onlinelibrary.wiley.com/doi/10.1002/advs.202101394

[5] V. Filippou and C. Tsoumpas, "Recent advances on the development of phantoms using 3D printing for imaging with CT, MRI, PET, SPECT, and ultrasound," *Medical Physics*, vol. 45, no. 9, Sep. 2018. [Online]. Available: https://aapm.onlinelibrary.wiley.com/doi/10.1002/mp.13058

[6] K. Jędrzejczak, A. Antonowicz, B. Butruk-Raszeja, W. Orciuch, K. Wojtas, P. Piasecki, J. Narloch, M. Wierzbicki, and Makowski, "Three-Dimensionally Printed Elastic Cardiovascular Phantoms for Carotid Angioplasty Training and Personalized Healthcare," *Journal of Clinical Medicine*, vol. 13, no. 17, p. 5115, Aug. 2024. [Online]. Available: https://www.mdpi.com/2077-0383/13/17/5115

[7] K. N. Sommer, M. M. S. Bhurwani, V. Tutino, A. Siddiqui, J. Davies, K. Snyder, E. Levy, M. Mokin, and C. N. Ionita, "Use of patient specific 3D printed neurovascular phantoms to simulate mechanical thrombectomy," *3D Printing in Medicine*, vol. 7, no. 1, p. 32, Dec. 2021. [Online]. Available: https://threedmedprint.biomedcentral.com/articles/10.1186/s41205-021-00122-8

[8] W. H. Orginization, "Cardiovascular diseases (CVDs)," Jul. 2025. [Online]. Available: https://www.who.int/news-room/fact-sheets/detail/cardiovascular-diseases-%28cvds%29?utm_

[9] S. Martin, "2025 Heart Disease & Stroke Statistics Update Fact Sheet Global Burden of Disease," 2025. [Online]. Available: https://professional.heart.org/-/media/phd-files-2/science-news/2/2025-heart-and-stroke-stat-update/factsheets/2025-stats-update-fact-sheet-global-burden-of-disease.pdf?utm_

[10] W. Hong, V. Tewari, H. Yu, J. Chen, and A. P. Sawchuk, "Evaluating compliance in three-dimensional-printed polymeric vascular grafts compared to human arteries and commercial grafts in a mock circulation loop compliance in three-dimensional-printed polymeric vascular grafts," *JVS-Vascular Science*, vol. 6, p. 100291, 2025. [Online]. Available: https://linkinghub.elsevier.com/retrieve/pii/S2666350325000124

[11] D. Camasão and D. Mantovani, "The mechanical characterization of blood vessels and their substitutes in the continuous quest for physiological-relevant performances. A critical review," *Materials Today Bio*, vol. 10, p. 100106, Mar. 2021. [Online]. Available: https://linkinghub.elsevier.com/retrieve/pii/S2590006421000144

[12] S. A. Oh, M. J. Kim, J. S. Kang, H. S. Hwang, Y. J. Kim, S. H. Kim, J. W. Park, J. W. Yea, and S. K. Kim, "Feasibility of Fabricating Variable Density Phantoms Using 3D Printing for Quality Assurance (QA) in Radiotherapy," *Progress in Medical Physics*, vol. 28, no. 3, p. 106, 2017. [Online]. Available: https://synapse.koreamed.org/DOIx.php?id=10.14316/pmp.2017.28.3.106

[13] L. M. Kinnard, M. A. Gavrielides, K. J. Myers, R. Zeng, J. Peregoy, W. Pritchard, J. W. Karanian, and N. Petrick, "Volume error analysis for lung nodules attached to pulmonary vessels in an anthropomorphic thoracic phantom," M. L. Giger and N. Karssemeijer, Eds., San Diego, CA, Mar. 2008, p. 69152Q. [Online]. Available: http://proceedings.spiedigitallibrary.org/proceeding.aspx?doi=10.1117/12.773039

[14] A. S. Lemine, Z. Ahmad, N. J. Al-Thani, A. Hasan, and J. Bhadra, "Mechanical properties of human hepatic tissues to develop liver-mimicking phantoms for medical applications," *Biomechanics and Modeling in Mechanobiology*, vol. 23, no. 2, pp. 373–396, Apr. 2024. [Online]. Available: https://link.springer.com/10.1007/s10237-023-01785-4

[15] J. Coles-Black, D. Bolton, and J. Chuen, "Accessing 3D Printed Vascular Phantoms for Procedural Simulation," *Frontiers in Surgery*, vol. 7, p. 626212, Jan. 2021. [Online]. Available: https://www.frontiersin.org/articles/10.3389/fsurg.2020.626212/full

[16] J. Illi, B. Bernhard, C. Nguyen, T. Pilgrim, F. Praz, M. Gloeckler, S. Windecker, A. Haeberlin, and C. Gräni, "Translating Imaging Into 3D Printed Cardiovascular

Phantoms," *JACC: Basic to Translational Science*, vol. 7, no. 10, pp. 1050–1062, Oct. 2022. [Online]. Available: https://linkinghub.elsevier.com/retrieve/pii/S2452302X22000055

[17] A. Altermatt, F. Santini, X. Deligianni, S. Magon, T. Sprenger, L. Kappos, P. Cattin, J. Wuerfel, and L. Gaetano, "Design and construction of an innovative brain phantom prototype for MRI," *Magnetic Resonance in Medicine*, vol. 81, no. 2, pp. 1165–1171, Feb. 2019. [Online]. Available: https://onlinelibrary.wiley.com/doi/10.1002/mrm.27464

[18] N. Kiarashi, A. C. Nolte, G. M. Sturgeon, W. P. Segars, S. V. Ghate, L. W. Nolte, E. Samei, and J. Y. Lo, "Development of realistic physical breast phantoms matched to virtual breast phantoms based on human subject data," *Medical Physics*, vol. 42, no. 7, pp. 4116–4126, Jul. 2015. [Online]. Available: https://aapm.onlinelibrary.wiley.com/doi/10.1118/1.4919771

[19] X. Tan, D. Li, M. Jeong, T. Yu, Z. Ma, S. Afat, K.-E. Grund, and T. Qiu, "Soft Liver Phantom with a Hollow Biliary System," *Annals of Biomedical Engineering*, vol. 49, no. 9, pp. 2139–2149, Sep. 2021. [Online]. Available: https://link.springer.com/10.1007/s10439-021-02726-x

[20] H. Mirgolbabaee, J. R. Nagel, J. Plomp, A. Ghanbarzadeh-Dagheyan, J. A. Simmering, M. Versluis, M. M. P. J. Reijnen, and E. Groot Jebbink, "Vascular Flow Phantom of A Cohort-Based Averaged Abdominal Aortic Aneurysm: Design, Fabrication and Characterization," *Annals of Biomedical Engineering*, vol. 53, no. 6, pp. 1439–1452, Jun. 2025. [Online]. Available: https://link.springer.com/10.1007/s10439-025-03717-y

[21] J. Xu, Y. Lin, S. Thakur, H. Nie, L. Wang, and Q. Zhu, "Low-cost microvascular phantom for photoacoustic imaging using loofah," *Journal of Biomedical Optics*, vol. 30, no. 01, Jan. 2025. [Online]. Available: https://www.spiedigitallibrary.org/journals/journal-of-biomedical-optics/volume-30/issue-01/016006/Low-cost-microvascular-phantom-for-photoacoustic-imaging-using-loofah/10.1117/1.JBO.30.1.016006.full

[22] S. Fortune, M. A. Jansen, T. Anderson, G. A. Gray, J. E. Schneider, P. R. Hoskins, and I. Marshall, "Development and characterization of rodent cardiac phantoms: comparison with in vivo cardiac imaging," *Magnetic Resonance Imaging*, vol. 30, no. 8, pp. 1186–1191, Oct. 2012. [Online]. Available: https://linkinghub.elsevier.com/retrieve/pii/S0730725X12001786

[23] J. Li, X. Hu, Y. Chen, D. Fan, C. Tan, S. Yang, H. Wu, Y. Wang, Q. An, Z. Xiao, J. Hu, J. He, Y. Qian, and Z. Qian, "Review of recent progress in vascular stents: From conventional to functional vascular stents," *Chinese Chemical Letters*, vol. 36, no. 7, p. 110492, Jul. 2025. [Online]. Available: https://linkinghub.elsevier.com/retrieve/pii/S1001841724010118

[24] R. Luengo-Fernandez, "Economic burden of cardiovascular diseases in the European Union: a population-based cost study," 2023.

[25] M. E. Laughlin, S. E. Stephens, J. A. Hestekin, and M. O. Jensen, "Development of Custom Wall-Less Cardiovascular Flow Phantoms with Tissue-Mimicking Gel," *Cardiovascular Engineering and Technology*, vol. 13, no. 1, pp. 1–13, Feb. 2022. [Online]. Available: https://link.springer.com/10.1007/s13239-021-00546-7

[26] M. E. Kamphuis, M. J. W. Greuter, R. H. J. A. Slart, and C. H. Slump, "Quantitative imaging: systematic review of perfusion/flow phantoms," *European Radiology Experimental*, vol. 4, no. 1, p. 15, Dec. 2020. [Online]. Available: https://eurradiolexp.springeropen.com/articles/10.1186/s41747-019-0133-2

[27] J. P. Raad, D. Lock, Y.-Y. Liu, M. Solomon, L. Peralta, and K. Christensen-Jeffries, "Optically-Validated Microvascular Phantom for Super-Resolution Ultrasound Imaging," Sep. 2024, arXiv:2409.09031 [physics]. [Online]. Available: http://arxiv.org/abs/2409.09031

[28] G. Biglino, P. Verschueren, R. Zegels, A. M. Taylor, and S. Schievano, "Rapid prototyping compliant arterial phantoms for in-vitro studies and device testing," *Journal of Cardiovascular Magnetic Resonance*, vol. 15, no. 1, p. 2, Jan. 2013. [Online]. Available: https://linkinghub.elsevier.com/retrieve/pii/S1097664723007184

[29] Edexcel, "Structure of blood and vessels," 2023. [Online]. Available: https://www.bbc.co.uk/bitesize/guides/z9n6sg8/revision/2

[30] S. G. Yazdi, P. H. Geoghegan, P. D. Docherty, M. Jermy, and A. Khanafer, "A Review of Arterial Phantom Fabrication Methods for Flow Measurement Using PIV Techniques," *Annals of Biomedical Engineering*, vol. 46, no. 11, pp. 1697–1721, Nov. 2018. [Online]. Available: http://link.springer.com/10.1007/s10439-018-2085-8

[31] C. N. Ionita, M. Mokin, N. Varble, D. R. Bednarek, J. Xiang, K. V. Snyder, A. H. Siddiqui, E. I. Levy, H. Meng, and S. Rudin, "Challenges and limitations of patient-specific vascular phantom fabrication using 3D Polyjet printing," R. C. Molthen and J. B. Weaver, Eds., San Diego, California, USA, Mar. 2014, p. 90380M. [Online]. Available: http://proceedings.spiedigitallibrary.org/proceeding.aspx?doi=10.1117/12.2042266

[32] S. Z. Li, *Capillary Blood Vessel*. Encyclopedia of Biometrics, 2009. [Online]. Available: https://doi.org/10.1007/978-0-387-73003-5_133

[33] S. G. Yazdi, L. Huetter, P. D. Docherty, P. N. Williamson, D. Clucas, M. Jermy, and P. H. Geoghegan, "A Novel Fabrication Method for Compliant Silicone Phantoms of Arterial Geometry for Use in Particle Image Velocimetry of Haemodynamics," *Applied Sciences*, vol. 9, no. 18, p. 3811, Sep. 2019. [Online]. Available: https://www.mdpi.com/2076-3417/9/18/3811

[34] J. H. Kim, P. Chhai, and K. Rhee, "Development and characterization of viscoelastic polydimethylsiloxane phantoms for simulating arterial wall motion," *Medical Engineering & Physics*, vol. 91, pp. 12–18, May 2021. [Online]. Available: https://linkinghub.elsevier.com/retrieve/pii/S1350453321000278

[35] Wikipedia, "Artery Wikipedia," 2025. [Online]. Available: https://en.wikipedia.org/wiki/Artery

[36] Professional, "Arteries," 2025. [Online]. Available: https://my.clevelandclinic.org/health/body/22896-arteries

[37] J. Illi, M. Bergamin, M. Ilic, A. W. Stark, S. Bracher, M. Hofmann, J. Burger, I. Shiri, A. Haeberlin, and C. Gräni, "Mechanical properties of 3D voxel-printed materials for cardiovascular tissue imitation," *Frontiers in Bioengineering and Biotechnology*, vol. 13, p. 1569553, May 2025. [Online]. Available: https://www.frontiersin.org/articles/10.3389/fbioe.2025.1569553/full

[38] K. N. Sommer, M. M. S. Bhurwani, V. Iyer, and C. N. Ionita, "Comparison of fluid dynamics changes due to physical activity in 3D printed patient specific coronary phantoms with the Windkessel equivalent model of coronary flow," *3D Printing in Medicine*, vol. 8, no. 1, p. 10, Dec. 2022. [Online]. Available: https://threedmedprint.biomedcentral.com/articles/10.1186/s41205-022-00138-8

[39] E. Hosseinzadeh, H. Mirgolbabaee, L. Van De Velde, M. Versluis, E. Groot Jebbink, A. Aguirre-Soto, and M. M. P. J. Reijnen, "Soft stereolithographic 3D printed phantoms for dual-modality particle image velocimetry (PIV)," *Experiments in Fluids*, vol. 66, no. 1, p. 20, Jan. 2025. [Online]. Available: https://link.springer.com/10.1007/s00348-024-03938-2

[40] A. Amini, R. M. Guijt, T. Themelis, J. De Vos, and S. Eeltink, "Recent developments in digital light processing 3D-printing techniques for microfluidic analytical devices," *Journal of Chromatography A*, vol. 1692, p. 463842, Mar. 2023. [Online]. Available: https://linkinghub.elsevier.com/retrieve/pii/S0021967323000705

[41] K. H. Schneider, G. Oberoi, E. Unger, K. Janjic, S. Rohringer, S. Heber, H. Agis, A. Schedle, H. Kiss, B. K. Podesser, R. Windhager, S. Toegel, and F. Moscato, "Medical 3D printing with polyjet technology: effect of material type and printing orientation on printability, surface structure and cytotoxicity," *3D Printing in Medicine*, vol. 9, no. 1, p. 27, Sep. 2023. [Online]. Available: https://threedmedprint.biomedcentral.com/articles/10.1186/s41205-023-00190-y

[42] Stratasys, "MED601 datasheet," 2015. [Online]. Available: http://stratasys.com/en/materials/materials-catalog/polyjet-materials/biocompatible-clear-med610/

[43] ——, "VeroClear datasheet," 2015. [Online]. Available: https://www.stratasys.com/en/materials/materials-catalog/polyjet-materials/veroclear/

[44] Y. Soni, P. Rothweiler, and A. G. Erdman, "Mechanical Characterization and Feasibility Analysis of PolyJet™ Materials in Tissue-Mimicking Applications," *Machines*, vol. 13, no. 3, p. 234, Mar. 2025. [Online]. Available: https://www.mdpi.com/2075-1702/13/3/234

[45] J.-W. Choi, H.-C. Kim, and R. Wicker, "Multi-material stereolithography," *Journal of Materials Processing Technology*, vol. 211, no. 3, pp. 318–328, Mar. 2011. [Online]. Available: https://linkinghub.elsevier.com/retrieve/pii/S0924013610003043

[46] A. Zhakeyev, M. Abdulrhman, Y. Zhang, F. Li, G. Chen, and J. Marques-Hueso, "Upconversion 3D printing enables single-immersion multi-material stereolithography," *Applied Materials Today*, vol. 32, p. 101854, Jun. 2023. [Online]. Available: https://linkinghub.elsevier.com/retrieve/pii/S2352940723001245

[47] B. Khatri, M. Frey, A. Raouf-Fahmy, M.-V. Scharla, and T. Hanemann, "Development of a Multi-Material Stereolithography 3D Printing Device," *Micromachines*, vol. 11, no. 5, p. 532, May 2020. [Online]. Available: https://www.mdpi.com/2072-666X/11/5/532

[48] P. Madeleine, "What is the Difference Between SLA and MSLA 3D Printing?" 2022. [Online]. Available: https://www.3dnatives.com/en/difference-between-sla-and-msla-020820224/#!

[49] C. Alparslan and Bayraktar, "Advances in Digital Light Processing (DLP) Bioprinting: A Review of Biomaterials and Its Applications, Innovations, Challenges, and Future Perspectives," *Polymers*, vol. 17, no. 9, p. 1287, May 2025. [Online]. Available: https://www.mdpi.com/2073-4360/17/9/1287

[50] I. Ahmed, K. Sullivan, and A. Priye, "Multi-Resin Masked Stereolithography (MSLA) 3D Printing for Rapid and Inexpensive Prototyping of Microfluidic Chips with Integrated Functional Components," *Biosensors*, vol. 12, no. 8, p. 652, Aug. 2022. [Online]. Available: https://www.mdpi.com/2079-6374/12/8/652

[51] B. Ngatane, J. A. Dicks, W. H. Ho, and M. Ngoepe, "Masked stereolithography as an accessible additive manufacturing technology to fabricate soft polymeric flow phantoms," *MATEC Web of Conferences*, vol. 406,

p. 07014, 2024. [Online]. Available: https://www.matec-conferences.org/10.1051/matecconf/202440607014

[52] A. Milovanović, M. Montanari, Z. Golubović, M. P. Mărghitaş, A. Spagnoli, R. Brighenti, and A. Sedmak, "Compressive and flexural mechanical responses of components obtained through mSLA vat photopolymerization technology," *Theoretical and Applied Fracture Mechanics*, vol. 131, p. 104406, Jun. 2024. [Online]. Available: https://linkinghub.elsevier.com/retrieve/pii/S0167844224001551

[53] J. O'Connell, "MSLA vs SLA: The Main Differences," 2024. [Online]. Available: https://www.3dsourced.com/3d-printing-technologies/msla-vs-sla/?utm_source=chatgpt.com

[54] Formlabs, "Clear Resin datasheet," 2016. [Online]. Available: chrome-extension://efaidnbmnnnibpcajpcglclefindmkaj/https://formlabs-media.formlabs.com/datasheets/1801089-TDS-ENUS-0P.pdf

[55] ——, "Flexible 80A datasheet," 2020. [Online]. Available: chrome-extension://efaidnbmnnnibpcajpcglclefindmkaj/https://formlabs-media.formlabs.com/datasheets/2001418-TDS-ENUS-0.pdf?utm_

[56] P. Netwrok, "FDM 3d printing materials compared." [Online]. Available: https://www.hubs.com/knowledge-base/fdm-3d-printing-materials-compared/?utm_

[57] Iemai, "PLA datasheet." [Online]. Available: chrome-extension://efaidnbmnnnibpcajpcglclefindmkaj/https://www.iemai3d.com/wp-content/uploads/2021/03/PLA_TDS__EN.pdf?utm_

[58] Stratasys, "TPU 92A datasheet," 2008. [Online]. Available: chrome-extension://efaidnbmnnnibpcajpcglclefindmkaj/https://www.stratasys.com/siteassets/materials/materials-catalog/fdm-materials/tpu-92a/fdm-tpu-92a-3d-printing-material-data-sheet_a.pdf?utm_

[59] R. F. Quero, G. Domingos Da Silveira, J. A. Fracassi Da Silva, and D. P. D. Jesus, "Understanding and improving FDM 3D printing to fabricate high-resolution and optically transparent microfluidic devices," *Lab on a Chip*, vol. 21, no. 19, pp. 3715–3729, 2021. [Online]. Available: https://xlink.rsc.org/?DOI=D1LC00518A

[60] G. Annio, G. Franzetti, M. Bonfanti, A. Gallarello, A. Palombi, E. De Momi, S. Homer-Vanniasinkam, H. A. Wurdemann, V. Tsang, V. Diáz-Zuccarini, R. Torii, S. Balabani, and G. Burriesci, "Low-Cost Fabrication of Polyvinyl Alcohol-Based Personalized Vascular Phantoms for In Vitro Hemodynamic Studies: Three Applications," *Journal of Engineering and Science in Medical Diagnostics and Therapy*, vol. 3, no. 3, p. 034501, Aug. 2020. [Online]. Available: https://asmedigitalcollection.asme.org/medicaldiagnostics/article/doi/10.1115/1.4045760/1072109/LowCost-Fabrication-of-Polyvinyl-AlcoholBased

[61] Zongheng, "DLP 3D Printing: A Comprehensive Guide," 2024. [Online]. Available: https://www.zongheng3d.com/dlp-3d-printing-comprehensive-guide/

[62] C.-L. Lin, J.-T. Liu, and C.-S. Shin, "High-Resolution DLP 3D Printing for Complex Curved and Thin-Walled Structures at Practical Scale: Archimedes Microscrew," *Micromachines*, vol. 16, no. 7, p. 762, Jun. 2025. [Online]. Available: https://www.mdpi.com/2072-666X/16/7/762

[63] J. Qiu, J. Li, Z. Guo, Y. Zhang, B. Nie, G. Qi, X. Zhang, J. Zhang, and R. Wei, "3D Printing of Individualized Microfluidic Chips with DLP-Based Printer," *Materials*, vol. 16, no. 21, p. 6984, Oct. 2023. [Online]. Available: https://www.mdpi.com/1996-1944/16/21/6984

[64] microsla Inc., "Microsla materials," 2019. [Online]. Available: https://www.microsla.com/ultra-high-resolution-uv-resins/

[65] TDS-UV-Flex, "Datasheet microsla flex resin," 2019. [Online]. Available: https://www.microsla.com/ultra-high-resolution-uv-resins/

[66] TDS-UV-Clear, "Datasheet microsla clear resin," 2019. [Online]. Available: https://www.microsla.com/ultra-high-resolution-uv-resins/

[67] M. Levin, Y. Tang, C. D. Eisenbach, M. T. Valentine, and N. Cohen, "Understanding the Response of Poly(ethylene glycol) diacrylate (PEGDA) Hydrogel Networks: A Statistical Mechanics-Based Framework," *Macromolecules*, vol. 57, no. 15, pp. 7074–7086, Aug. 2024. [Online]. Available: https://pubs.acs.org/doi/10.1021/acs.macromol.3c02635

[68] M. Hakim Khalili, R. Zhang, S. Wilson, S. Goel, S. A. Impey, and A. I. Aria, "Additive Manufacturing and Physicomechanical Characteristics of PEGDA Hydrogels: Recent Advances and Perspective for Tissue Engineering," *Polymers*, vol. 15, no. 10, p. 2341, May 2023. [Online]. Available: https://www.mdpi.com/2073-4360/15/10/2341

[69] E. Ferchichi, S. Stealey, P. Bogert, and S. P. Zustiak, "Tunable gelatin methacrylate polyethylene glycol diacrylate hydrogels for cell mechanosensing applications," *Frontiers in Biomaterials Science*, vol. 3, p. 1408748, Jul. 2024. [Online]. Available: https://www.frontiersin.org/articles/10.3389/fbiom.2024.1408748/full

[70] M. Zanon, D. Baruffaldi, M. Sangermano, C. F. Pirri, F. Frascella, and A. Chiappone, "Visible light-induced crosslinking of unmodified gelatin with PEGDA for DLP-3D printable hydrogels," *European Polymer Journal*, vol. 160, p. 110813, Nov. 2021. [Online]. Available: https://linkinghub.elsevier.com/retrieve/pii/S0014305721005474

[71] M. Fowler, A. Moreno Lozano, J. Krause, P. Bednarz, S. Pandey, M. Ghayour, Q. Zhang, and O. Veiseh, "Guiding vascular infiltration through architected GelMA/PEGDA hydrogels: an *in vivo* study of channel diameter, length, and complexity," *Biomaterials Science*, vol. 13, no. 11, pp. 2951–2960, 2025. [Online]. Available: https://xlink.rsc.org/?DOI=D5BM00193E

[72] M. N. Antonuccio, E. Gasparotti, F. Bardi, A. Monteleone, A. This, L. Rouet, S. Avril, and S. Celi, "Fabrication of deformable patient-specific AAA models by material casting techniques," *Frontiers in Cardiovascular Medicine*, vol. 10, p. 1141623, Sep. 2023. [Online]. Available: https://www.frontiersin.org/articles/10.3389/fcvm.2023.1141623/full

[73] Q.-Z. Chi, L.-Z. Mu, Y. He, Y. Luan, and Y.-C. Jing, "A Brush–Spin–Coating Method for Fabricating In Vitro Patient-Specific Vascular Models by Coupling 3D-Printing," *Cardiovascular Engineering and Technology*, vol. 12, no. 2, pp. 200–214, Apr. 2021. [Online]. Available: https://link.springer.com/10.1007/s13239-020-00504-9

[74] B. Bisighini, P. Di Giovanni, A. Scerrati, F. Trovalusci, and S. Vesco, "Fabrication of Compliant and Transparent Hollow Cerebral Vascular Phantoms for In Vitro Studies Using 3D Printing and Spin–Dip Coating," *Materials*, vol. 16, no. 1, p. 166, Dec. 2022. [Online]. Available: https://www.mdpi.com/1996-1944/16/1/166

[75] P. Nguyen, I. Stanislaus, C. McGahon, K. Pattabathula, S. Bryant, N. Pinto, J. Jenkins, and C. Meinert, "Quality assurance in 3D-printing: A dimensional accuracy study of patient-specific 3D-printed vascular anatomical models," *Frontiers in Medical Technology*, vol. 5, p. 1097850, Feb. 2023. [Online]. Available: https://www.frontiersin.org/articles/10.3389/fmedt.2023.1097850/full

[76] S. N. Anindita, R. Conti, D. Zauchner, N. Paunović, W. Qiu, M. G. Buzhor, A. Krivitsky, Z. Luo, R. Müller, H. Grützmacher, X. Qin, J. Leroux, and Y. Bao, "Tough PEG-only hydrogels with complex 3D structure enabled by digital light processing of "all-PEG" resins," *Aggregate*, vol. 4, no. 6, p. e368, Dec. 2023. [Online]. Available: https://onlinelibrary.wiley.com/doi/10.1002/agt2.368

[77] Matprops, "PDMS datasheet," 2020. [Online]. Available: https://www.mit.edu/~6.777/matprops/pdms.htm

[78] A. Ahmadianyazdi, I. J. Miller, and A. Folch, "Tunable resins with PDMS-like elastic modulus for stereolithographic 3D-printing of multimaterial microfluidic actuators," *Lab on a Chip*, vol. 23, no. 18, pp. 4019–4032, 2023. [Online]. Available: https://xlink.rsc.org/?DOI=D3LC00529A

[79] S. Hatamikia, L. Jaksa, G. Kronreif, W. Birkfellner, J. Kettenbach, M. Buschmann, and A. Lorenz, "Silicone phantoms fabricated with multi-material extrusion 3D printing technology mimicking imaging properties of soft tissues in CT," *Zeitschrift für Medizinische Physik*, vol. 35, no. 2, pp. 138–151, May 2025. [Online]. Available: https://linkinghub.elsevier.com/retrieve/pii/S0939388923000764

[80] P. R. Costa, G. R. Boiset, E. B. Pimenta, R. M. V. Rocha, R. A. S. Moura, W. H. Marques, L. J. Oostveen, B. Geurts, M. V. Y. Sawamura, D. Y. Nersissian, E. M. Yoshimura, and I. Sechopoulos, "Hybrid phantom for lung CT: Design and validation," *Medical Physics*, vol. 52, no. 8, p. e17990, Aug. 2025. [Online]. Available: https://aapm.onlinelibrary.wiley.com/doi/10.1002/mp.17990

[81] H. Nisar, J. Moore, R. Piazza, E. Maneas, E. C. S. Chen, and T. M. Peters, "A simple, realistic walled phantom for intravascular and intracardiac applications," *International Journal of Computer Assisted Radiology and Surgery*, vol. 15, no. 9, pp. 1513–1523, Sep. 2020. [Online]. Available: https://link.springer.com/10.1007/s11548-020-02201-3

[82] P. Karimpour, R. Ferizoli, J. M. May, and P. A. Kyriacou, "Customisable Silicone Vessels and Tissue Phantoms for In Vitro Photoplethysmography Investigations into Cardiovascular Disease," *Sensors*, vol. 24, no. 5, p. 1681, Mar. 2024. [Online]. Available: https://www.mdpi.com/1424-8220/24/5/1681

[83] M. N. Hagedorn, M. Mächerle, R. Karl, C. Bergt, D. Böckler, S. Engelhardt, and K. Meisenbacher, "3D-Printed In Vitro Models of Stanford Type B Aortic Dissection: A Scoping Review," *Journal of Vascular Surgery Cases, Innovations and Techniques*, p. 101987, Sep. 2025. [Online]. Available: https://linkinghub.elsevier.com/retrieve/pii/S2468428725002692

[84] C. Dikyol, M. Altunbek, P. Bartolo, and B. Koc, "Multimaterial bioprinting approaches and their implementations for vascular and vascularized tissues," *Bioprinting*, vol. 24, p. e00159, Dec. 2021. [Online]. Available: https://linkinghub.elsevier.com/retrieve/pii/S2405886621000324

[85] H. Fallahi, J. Zhang, H.-P. Phan, and N.-T. Nguyen, "Flexible Microfluidics: Fundamentals, Recent Developments, and Applications," *Micromachines*, vol. 10, no. 12, p. 830, Nov. 2019. [Online]. Available: https://www.mdpi.com/2072-666X/10/12/830

[86] M. Higgins, S. Leung, and N. Radacsi, "3D printing surgical phantoms and their role in the visualization of medical procedures," *Annals of 3D Printed Medicine*, vol. 6, p. 100057, Jun. 2022. [Online]. Available: https://linkinghub.elsevier.com/retrieve/pii/S2666964122000133

[87] E. Hosseinzadeh, B. Bosques-Palomo, F. Carmona-Arriaga, M. A. Fabiani, and A. Aguirre-Soto, "Fabrication of Soft Transparent Patient-Specific Vascular Models with Stereolithographic 3D printing and Thiol-Based Photopolymerizable Coatings," *Macromolecular Rapid Communications*, vol. 45, no. 6, p. 2300611, Mar. 2024. [Online]. Available: https://onlinelibrary.wiley.com/doi/10.1002/marc.202300611

[88] A. Gallarello, "Patient-specific aortic phantom with tuneable compliance," 2019. [Online]. Available: https://asmedigitalcollection.asme.org/medicaldiagnostics/article-abstract/2/4/041005/975464/Patient-Specific-Aortic-Phantom-With-Tunable?redirectedFrom=fulltext

[89] H. Bruus, *Theoretical microfluidics*, ser. Oxford master series in physics. Oxford: Oxford University Press, 2023, no. 18.

[90] S. Pakravan, "The Differences Between Laminar and Turbulent Flow," 2025. [Online]. Available: https://cfdland.com/the-differences-between-laminar-and-turbulent-flow/

[91] Liqreate, "Liqcreate Elastomer-X." [Online]. Available: https://www.liqcreate.com/nl/product/elastomer-x/

[92] E. EU, "Elegoo Mars 5 Ultra." [Online]. Available: https://eu.elegoo.com/collections/mars-series/products/mars-5-ultra-9k-7inch-monochrome-lcd-resin-3d-printer?gad_source=1&gad_campaignid=20546305356&gbraid=0AAAAAqAZSFzCB5oidylCa0thCJijdDqS0&gclid=Cj0KCQjw_IXQBhCkARIsADqELbLlwJfzy-2_gDf1zPZLSW7TiWZ0MlRRSaguNHHtnBVFKugw40TF2SAaAk5IEALw_wcB

[93] J. Hoeben, "Hoe Elastomeer 3D-printhars verwerken?" 2025. [Online]. Available: https://www.liqcreate.com/nl/ondersteuningsartikelen/proces-3dprinted-elastomeer-hars/

[94] T. Twente, "3D Printing Manual Guide," 2020. [Online]. Available: chrome-extension://efaidnbmnnnibpcajpcglclefindmkaj/https://www.utwente.nl/en/rpl/Data%20sheets/Manuals/am-userguide.pdf

[95] Formlabs, "Moving from FDM to SLA," 2021. [Online]. Available: https://formlabs.com/blog/how-to-orient-sla-parts/

[96] C. Riccio, M. Civera, O. Grimaldo Ruiz, P. Pedullà, M. Rodriguez Reinoso, G. Tommasi, M. Vollaro, V. Burgio, and C. Surace, "Effects of Curing on Photosensitive Resins in SLA Additive Manufacturing," *Applied Mechanics*, vol. 2, no. 4, pp. 942–955, Nov. 2021. [Online]. Available: https://www.mdpi.com/2673-3161/2/4/55

[97] D. Hopman, "High-Resolution Multi-Material 3D Printing for Microfluidic Applications," 2024. [Online]. Available: https://repository.tudelft.nl/record/uuid:3a009808-5eca-4f3b-8a8d-e49307f7d793

[98] N. B. Cramer, C. P. O'Brien, and C. N. Bowman, "Mechanisms, polymerization rate scaling, and oxygen inhibition with an ultra-rapid monovinyl urethane acrylate," *Polymer*, vol. 49, no. 22, pp. 4756–4761, Oct. 2008. [Online]. Available: https://linkinghub.elsevier.com/retrieve/pii/S0032386108007453

[99] Fluigent, "Fluigent - Smart Microfluidics." 2026. [Online]. Available: https://www.fluigent.com/research/instruments/sensors/flow-unit/

[100] Metcal, "Syringe needles," 2022. [Online]. Available: https://store.metcal.com/en-eu/shop/fluid-dispensing/dispensing-tips/

[101] A. Possolo, "Simple Guide for Evaluating and Expressing the Uncertainty of NIST Measurement Results," National Institute of Standards and Technology, Tech. Rep. NIST TN 1900, Oct. 2015. [Online]. Available: https://nvlpubs.nist.gov/nistpubs/TechnicalNotes/NIST.TN.1900.pdf

[102] Elveflow, "Elveflow microfluidics," 2026. [Online]. Available: https://elveflow.com/microfluidic-products/microfluidics-flow-control-systems/ob1-pressure-controller/

Appendix A. CAD models of different channel sizes

Figure A.28 shows examples of the CAD models used for the printed flexible channels. The complete printability study included multiple lumen diameters and wall thicknesses, as described in the Materials and methods section. The models shown here are representative examples with different lumen diameters and wall thicknesses.

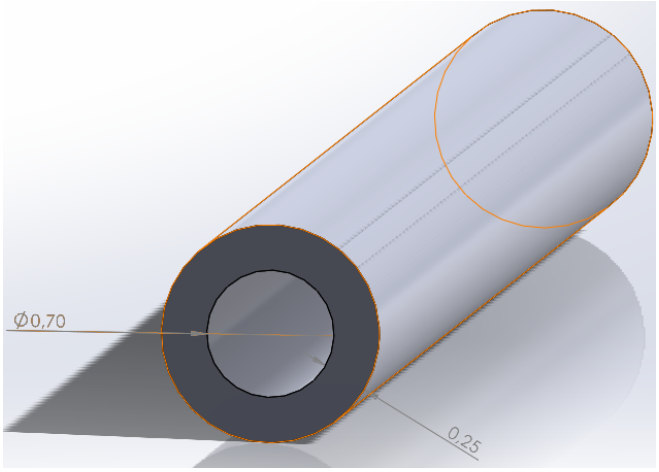

(a) D = 0.7 mm, t = 0.25 mm

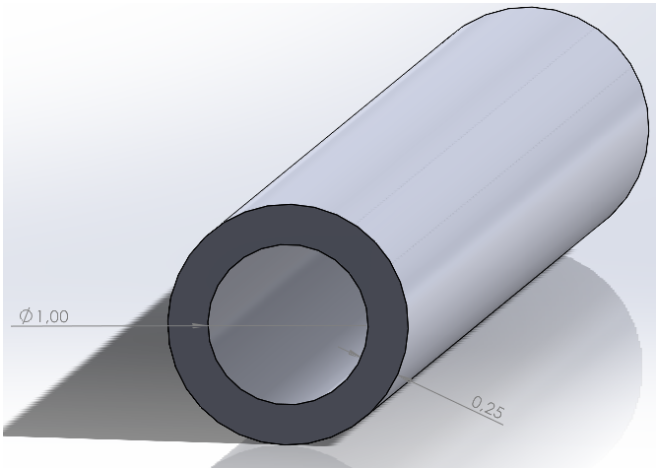

(b) D = 1.0 mm, t = 0.25 mm

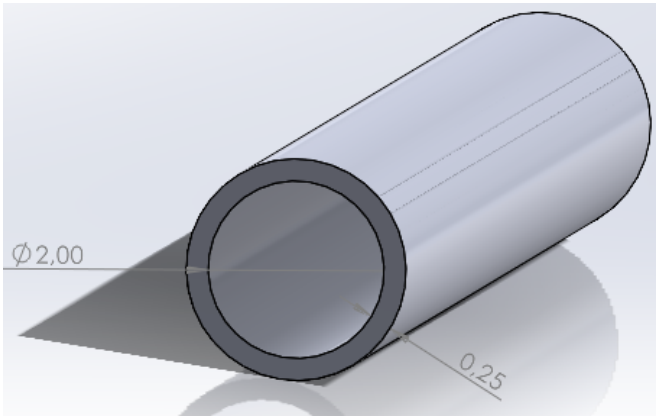

(c) D = 2.0 mm, t = 0.25 mm

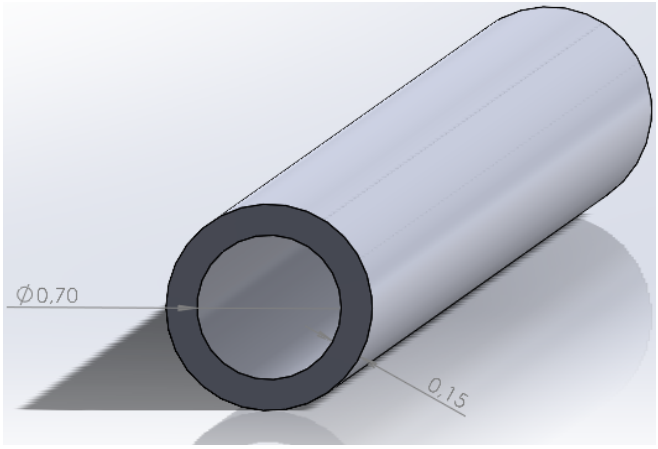

(d) D = 0.7 mm, t = 0.15 mm

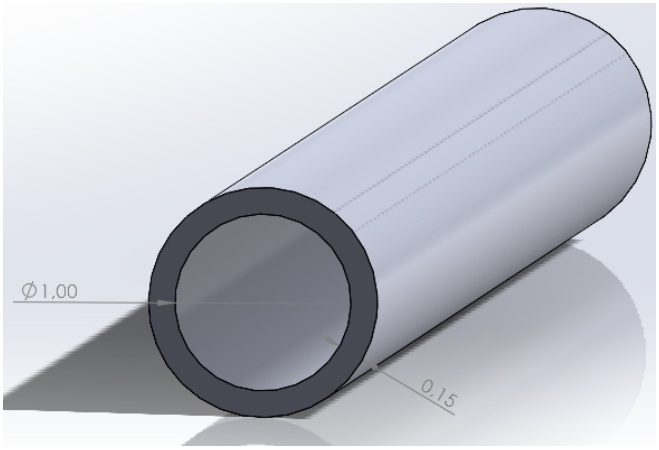

(e) D = 1.0 mm, t = 0.15 mm

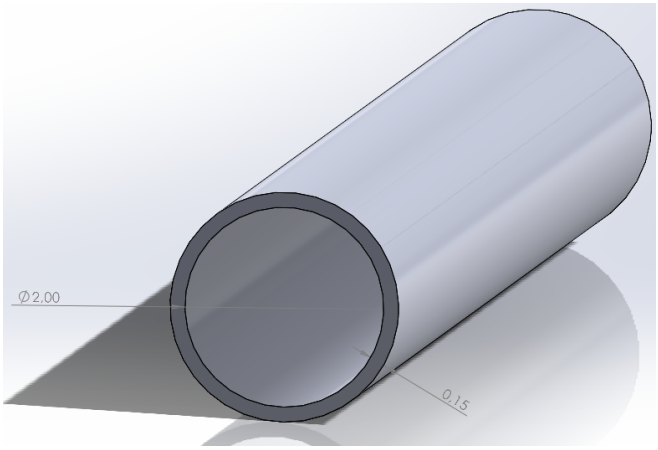

(f) D = 2.0 mm, t = 0.15 mm

Figure A.28: Examples of CAD models used for the flexible channel designs. The models show straight cylindrical channels with different lumen diameters D and wall thicknesses t. These examples illustrate the variation in channel geometry used to investigate the printability limits of the mSLA printer and elastomeric resin.

Appendix B. Chitubox slicing and support structures

Figure B.29 shows an example of the channel models after importing the STL files into Chitubox Basic V2.3. The channels were oriented vertically on the build plate, after which support structures were added around the channels. These supports were required to keep the flexible channels stable during printing and to reduce movement of the channels between printed layers.

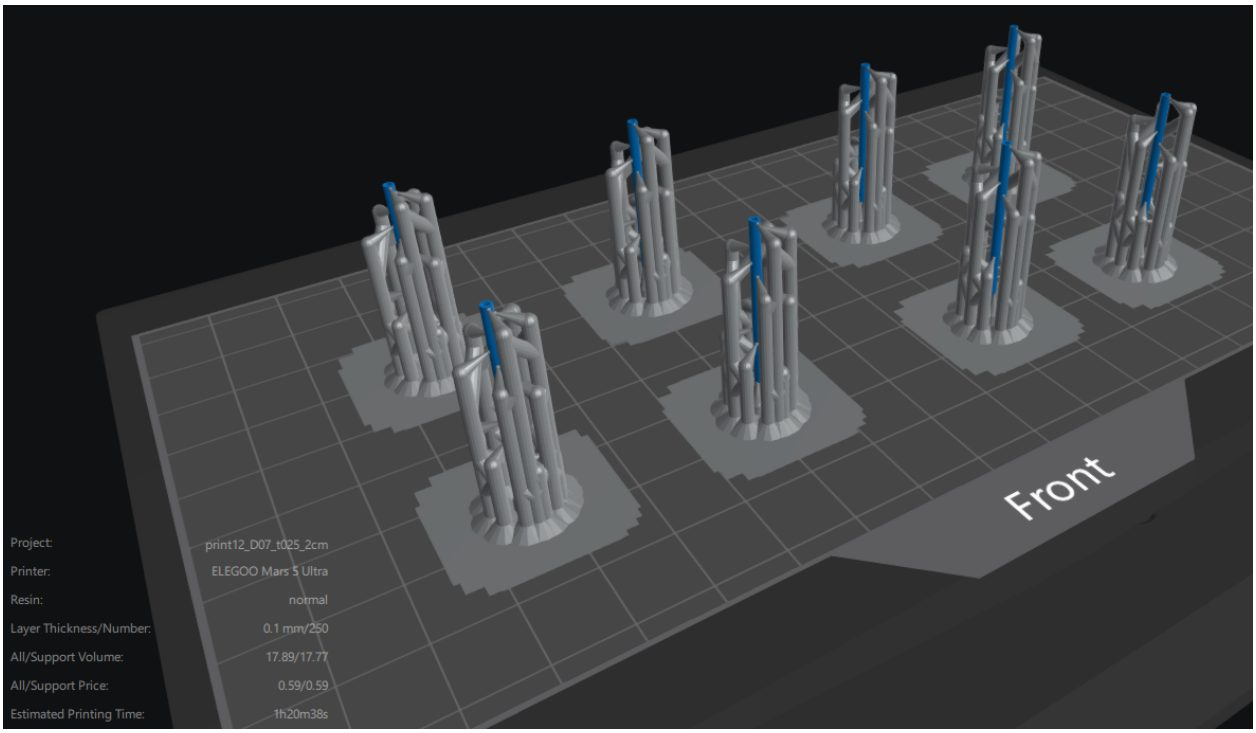

Figure B.29: Example of the channel models in Chitubox after orientation and support generation. The blue structures indicate the printed channel models, in this case with $D = 0.7$ mm and $t = 0.25$ mm, while the grey structures represent the added supports and support bases on the build plate.

The heavy-support configuration in Chitubox was used for all support structures. The support geometry consisted of a top section, a middle section, and a bottom section connected to a raft. The top section connected the support structure to the printed channel. A conical connection shape was used, with a contact diameter of 0.70 mm, a contact depth of 0.35 mm, a tip upper diameter of 0.30 mm, and a tip lower diameter of 1.50 mm. The middle section had a cylindrical shape with a diameter of 1.50 mm. The bottom section was connected to a raft with a height of 1.80 mm. These dimensions were selected to provide sufficient stability during printing while limiting direct contact with the flexible channel wall.

The most relevant support parameters are summarized in Table B.10. The remaining support parameters were kept at the default values of the heavy-support configuration.

Table B.10: Main Chitubox support parameters used for the flexible channel models.

Parameter	Value
Support type	Heavy
Top connection shape	Cone
Contact diameter	0.70 mm
Contact depth	0.35 mm
Tip upper diameter	0.30 mm
Tip lower diameter	1.50 mm
Middle support shape	Cylinder
Middle support diameter	1.50 mm
Raft height	1.80 mm

Appendix C. Tensile tests

Appendix C.1. Effect of printer exposure time and post-curing duration

Before selecting the final processing conditions, two initial sets of specimens were fabricated for the tensile tests. These tests were performed to determine which processing parameter had the strongest influence on the final stiffness of the printed material.

In the first set, the printer exposure time was varied while keeping the post-curing procedure constant. Printer exposure times of 10, 15, and 20 s per layer were tested. The post-curing procedure for these specimens consisted of 5 min in water followed by 25 min in air inside the UV-curing box.

In the second set, the printer exposure time was kept constant at 15 s per layer, while the post-curing duration was varied. The tested post-curing conditions were 5 min in water, 5 min in water followed by 25 min in air, and 5 min in water followed by 60 min in air. The tested conditions are summarized in Table C.11.

Table C.11: Printing and post-curing conditions used for the initial tensile tests. Comma-separated values indicate the separate conditions tested within each specimen set.

Parameter varied	Printer exposure [s per layer]	UV curing in water [min]	UV curing in air [min]
Printer exposure time	10, 15, 20	5	25
Post-curing duration	15	5	0, 25, 60

Appendix C.2. Stress-strain curves with linear fit

The stress-strain curves in Figure C.30 show the remaining two selected processing conditions that were not shown in the main text. These curves illustrate how the Young's modulus was determined for the E_{mid} and E_{+} configurations. For each specimen, a linear fit was applied to the initial part of the stress-strain curve, where the material response was assumed to be approximately elastic. The slope of this fitted region was used to calculate the Young's modulus.

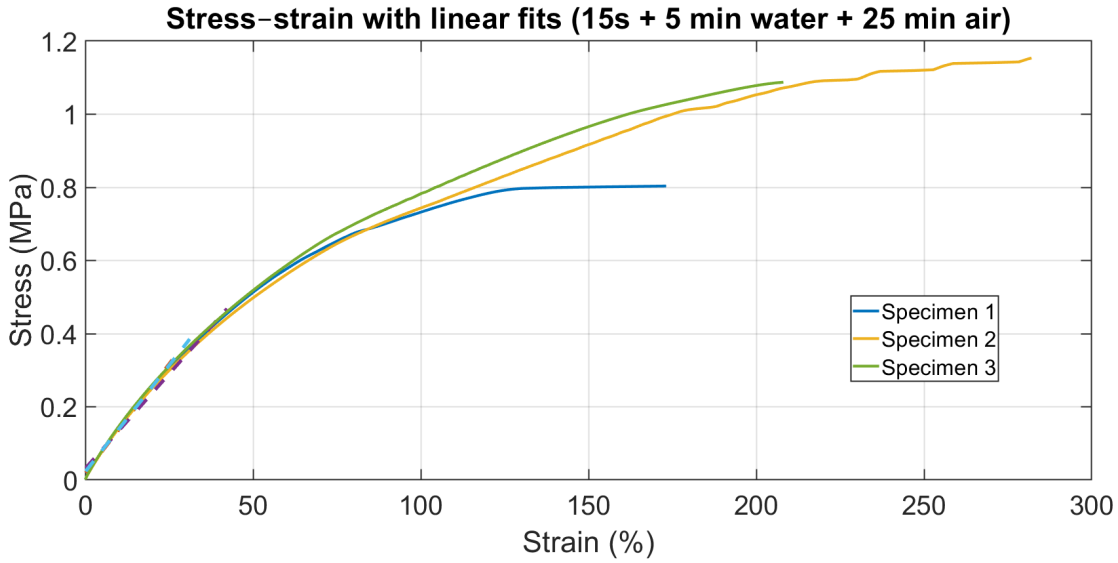

(a) 15 s printer exposure per layer with UV post-curing for 5 min in water followed by 25 min in air.

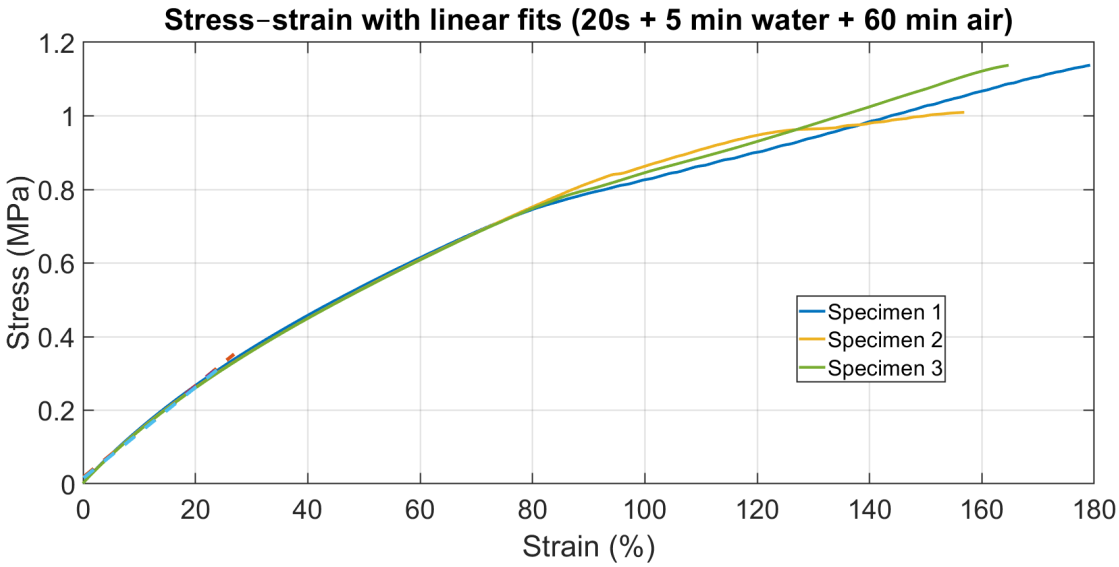

(b) 20 s printer exposure per layer with UV post-curing for 5 min in water followed by 60 min in air.

Figure C.30: Additional stress-strain curves of the printed Elastomer-X strip specimens. The linear fits in the initial elastic region were used to determine the Young's modulus of each specimen.

Appendix C.3. Effect of printer exposure time and post-curing time

To investigate which processing parameter had the largest influence on the final stiffness of the printed Elastomer-X material, the printer exposure time and the UV post-curing time were first varied separately. For the printer exposure-time comparison, the post-curing procedure was kept constant at 5 min in water followed by 25 min in air. For the post-curing comparison, the printer exposure time was kept constant at 15 s per layer.

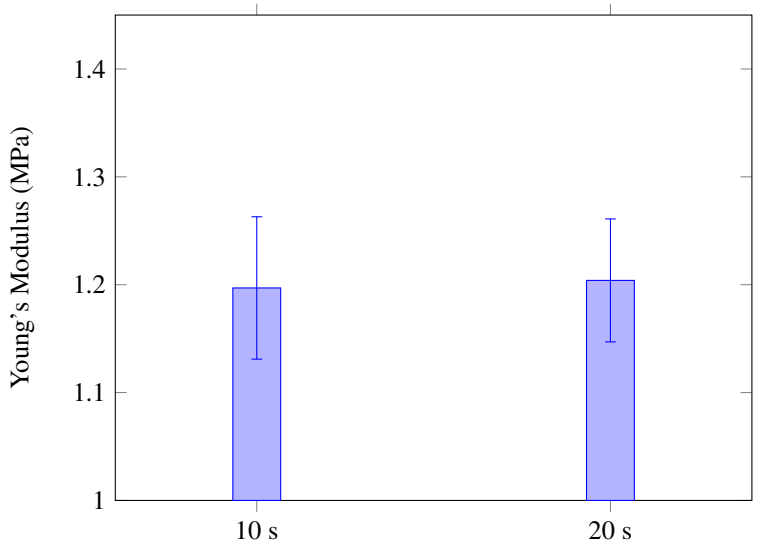

Figure C.31: Mean Young's modulus for different printer exposure times with the same post-curing procedure of 5 min in water followed by 25 min in air.

Figure C.31 shows that changing the printer exposure time from 10 s to 20 s per layer resulted in only a small difference in Young's modulus when the post-curing procedure was kept constant. The error bars overlap, indicating that no clear difference can be concluded from these specimens alone.

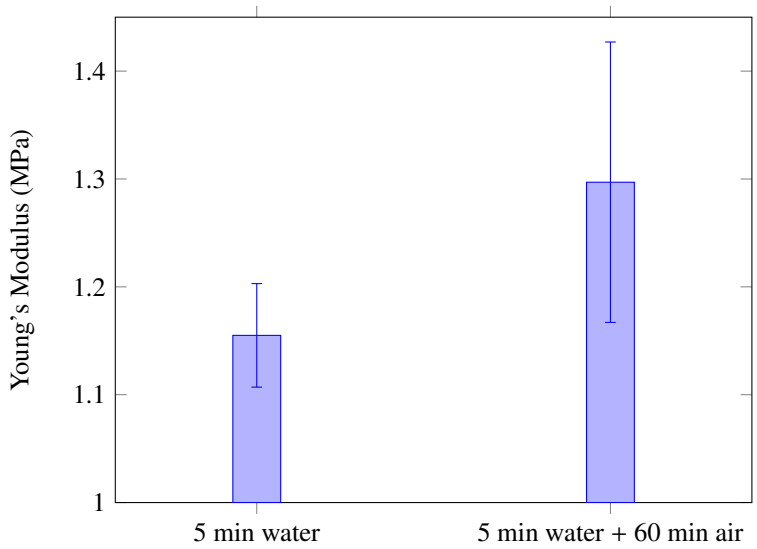

Figure C.32: Mean Young's modulus for different post-curing times with a fixed printer exposure time of 15 s per layer.

Figure C.32 shows a larger difference between the two post-curing conditions. The longer post-curing condition resulted in a higher mean Young's modulus, suggesting that post-curing time had a stronger effect on stiffness than printer exposure time. However, because the error bars still overlap, this trend could not be concluded with certainty.

Appendix D. Ink filled channels

The internal lumen geometry of the six channels used for the pressure-flow experiments was inspected using green ink diluted in water. The ink was manually injected into the channels to improve the visibility of the internal lumen under the microscope. Several local diameter measurements were taken along the channel length. These measurements were used to estimate representative initial diameters D_{ink} for the pressure-flow analysis.

The measured values should be interpreted as estimates. Because the channel walls were rounded and semi-transparent, the lumen boundary was not always sharply visible. In addition, the diameter was not constant along the entire channel length. Local narrow sections were considered when selecting D_{ink}, because they contribute strongly to the hydraulic resistance through the relation $R_h \propto D^{-4}$.

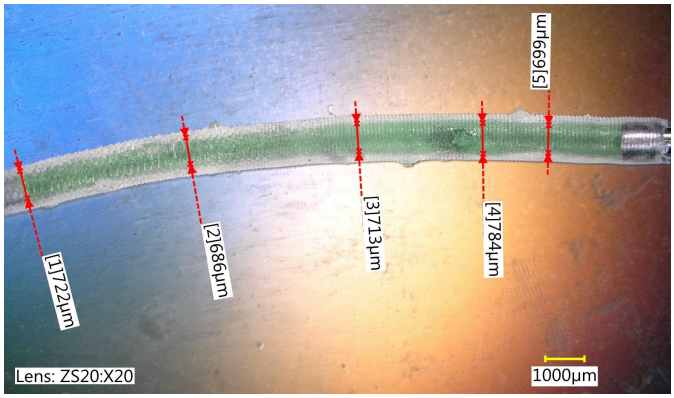

(a) Channel 1, E_- configuration

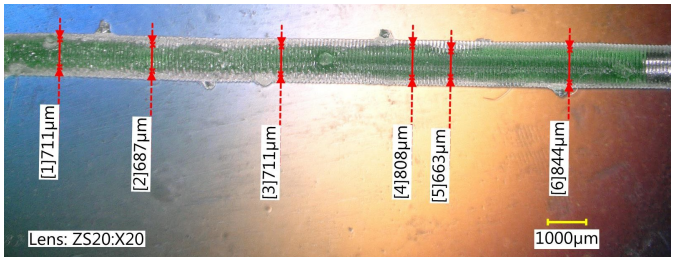

(b) Channel 2, E_- configuration

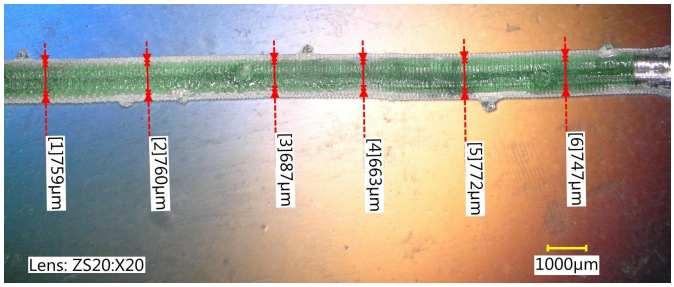

(c) Channel 3, E_- configuration

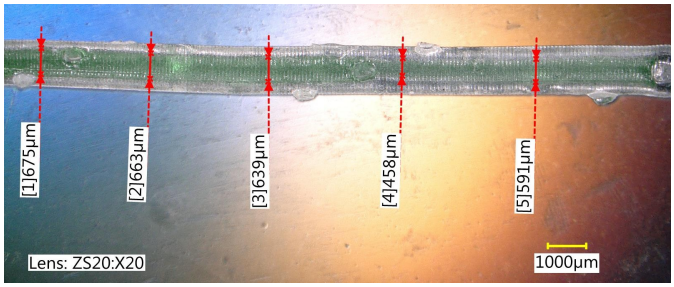

(d) Channel 4, E_+ configuration

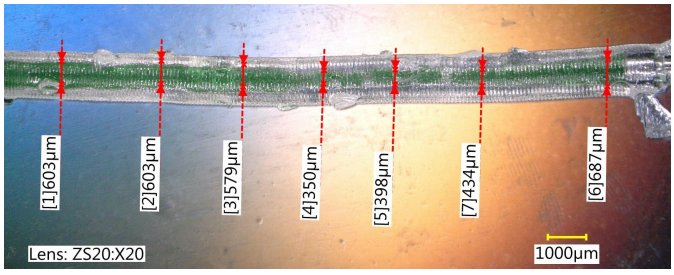

(e) Channel 5, E_+ configuration

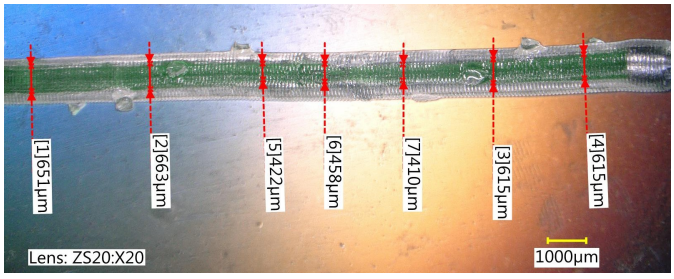

(f) Channel 6, E_+ configuration

Figure D.33: Microscope images of the six ink-filled channels used for the pressure-flow experiments. Channels 1–3 correspond to the E_- configuration with a printer exposure time of 10 s per layer, while channels 4–6 correspond to the E_+ configuration with a printer exposure time of 20 s per layer. The red markers indicate the locations where the local lumen diameter was measured.

Based on the local measurements and the observed lumen variations, the following representative initial diameters were selected:

Table D.12: Representative initial diameters used for the pressure-flow calculations.

Channel	Configuration	Selected D_{ink}
Channel 1	E_-, exp10	Approximately 0.7 mm
Channel 2	E_-, exp10	Approximately 0.7 mm
Channel 3	E_-, exp10	Approximately 0.7 mm
Channel 4	E_+, exp20	Approximately 0.6 mm
Channel 5	E_+, exp20	Approximately 0.5 mm
Channel 6	E_+, exp20	Approximately 0.5 mm

Appendix E. Preliminary ElveFlow pressure-flow measurements

Preliminary pressure-flow experiments were performed using ElveFlow equipment before the Fluigent setup was used. These measurements were useful for developing the experimental protocol, checking the connection method, and testing the baseline-correction procedure. However, the pressure range of these measurements was lower than in the Fluigent experiments, which reduced the measurable deformation range of the flexible channels. As a result, the uncertainty in the calculated effective diameter was too large to draw a reliable conclusion about channel expansion or narrowing. Therefore, the ElveFlow results were not used for the main pressure-flow analysis.

The ElveFlow setup used an OB1 MK4 microfluidic flow controller, pressure sensors, and a flow sensor [102]. The OB1 MK4 was used to control the applied pressure instead of directly controlling the flow rate. The pressure was measured using ElveFlow MPS 0 pressure sensors, which have a pressure range of 0–70 mbar. The flow rate was measured using an ElveFlow MFS 5+ flow sensor for water, with a flow range of 0–5 mL/min.

The pressure drop was measured over the same test section as in the Fluigent setup, between the two pressure sensors P_1 and P_2. The stiff tubing had an inner diameter of 0.800 mm, with a total tubing length of 90 mm between P_1 and P_2. The flexible channel was connected using 20 gauge dispensing tips with an inner diameter of 0.610 mm. The tested channel had a lumen diameter of 0.7 mm, wall thickness of 0.25 mm, and length of 20 mm.

The applied inlet pressure was increased stepwise from 0 to 110 mbar in steps of 10 mbar. Each pressure step was applied for approximately 10 s, allowing the pressure and flow signals to reach a steady state before the data were averaged. The measured quantities were the upstream pressure P_1, downstream pressure P_2, and flow rate Q. The same data-processing method as described in the main text was used: the final 4 s of each pressure step were averaged, baseline correction was applied at matched flow rates, and the channel-only hydraulic resistance was converted to an effective diameter using the Hagen–Poiseuille relation.

The main components and measurement settings of the preliminary ElveFlow setup are summarized in Table E.13.

Table E.13: Main components and settings of the preliminary ElveFlow pressure-flow setup.

Component	Specification
Pressure source	External compressed air supply
Pressure controller	ElveFlow OB1 MK4
Pressure sensors	ElveFlow MPS 0
Flow sensor	ElveFlow MFS 5+
Working fluid	Water
Applied pressure range	0–110 mbar
Pressure step size	10 mbar
Step duration	Approximately 10 s

Figure E.34 shows an example of the effective diameter obtained from the ElveFlow setup for channel 1. The error bars overlap over most of the pressure range, which indicates that the measurement uncertainty was large compared with the observed diameter trend. Therefore, no reliable pressure-dependent increase or decrease in effective diameter could be identified from these data.

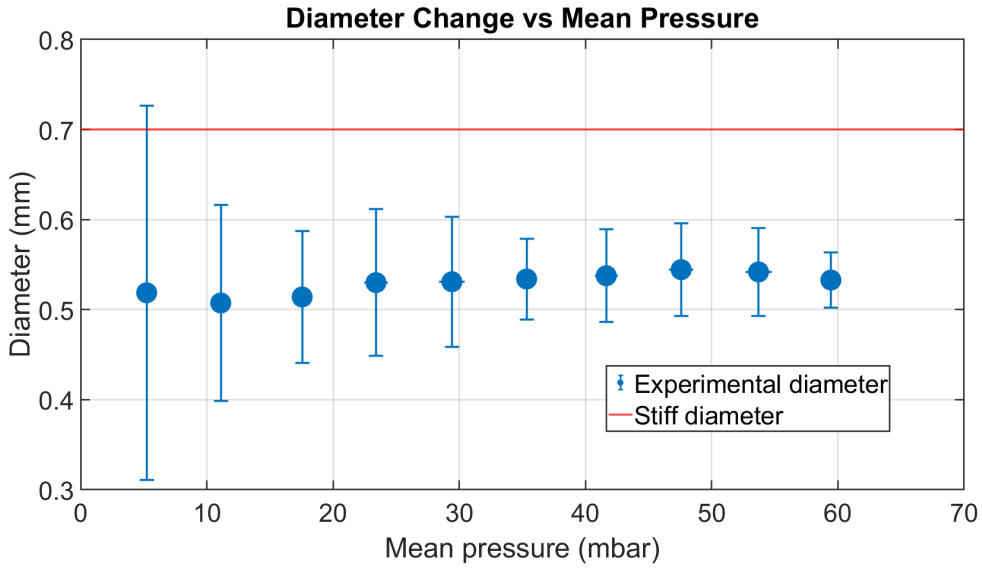

Figure E.34: Example effective diameter of channel 1 obtained from the preliminary ElveFlow measurements. The uncertainty is large compared with the measured trend, making it difficult to draw a reliable conclusion about pressure-induced channel expansion or narrowing.

Appendix F. Reynolds number validation

The Reynolds number was calculated to verify that the pressure-flow experiments were performed in the laminar-flow regime. As shown in Figure F.35, the Reynolds number remained approximately $Re \approx 250$, which is well below the critical value of $Re = 2300$. This supports the use of the laminar-flow assumptions in the hydraulic resistance and effective diameter analysis.

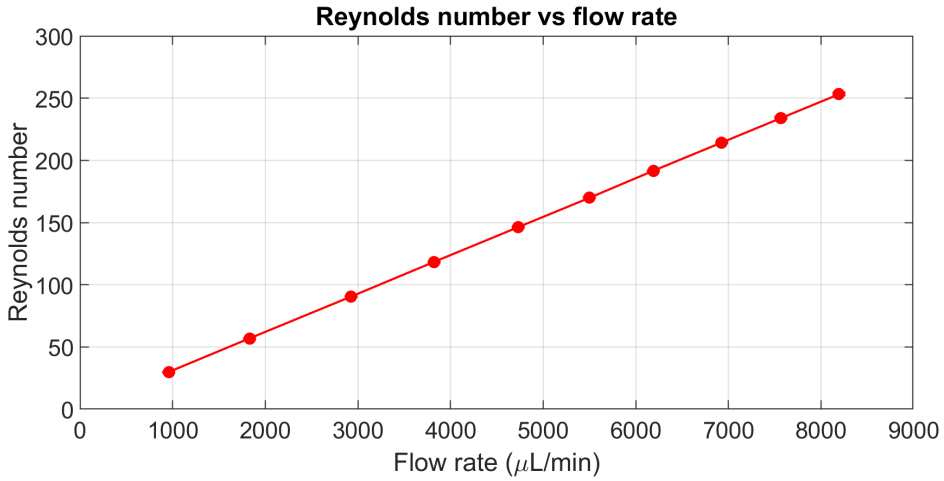

Figure F.35: Reynolds number calculated for the applied flow rates. The Reynolds number remained well below the critical value of $Re = 2300$, confirming that the experiments were performed in the laminar-flow regime.

Appendix G. Hydraulic resistance graphs

Figure G.36 shows the hydraulic resistance trends for channels 2–6. Channels 2, 3, and 4 show a decreasing hydraulic resistance with increasing mean pressure, which is consistent with pressure-induced channel expansion. Channel 6 shows only a small decrease and becomes almost constant at higher pressures. In contrast, channel 5 shows an increasing hydraulic resistance, which is not expected for an expanding flexible channel, indicating local narrowing.

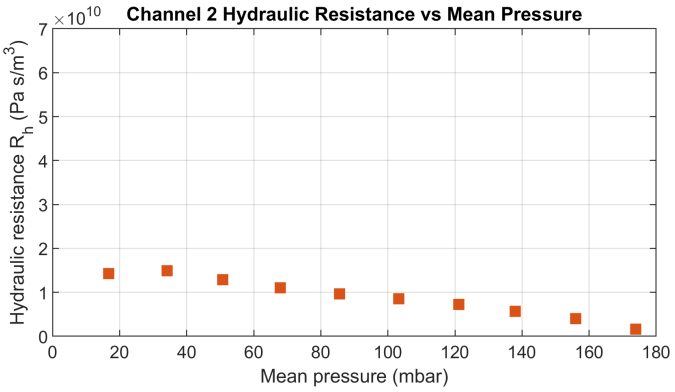

(a) Channel 2

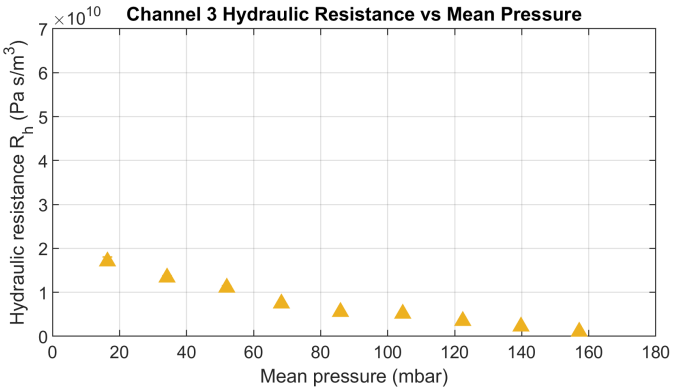

(b) Channel 3

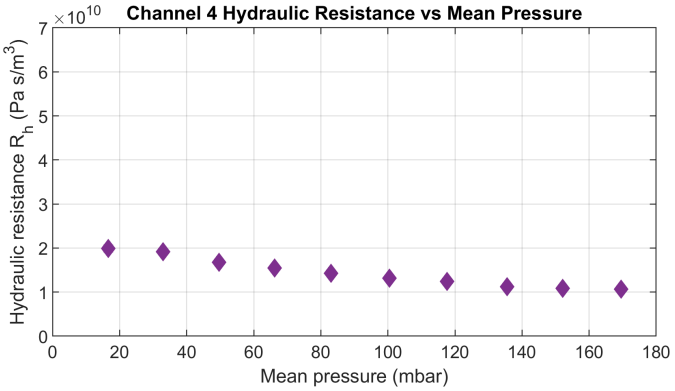

(c) Channel 4

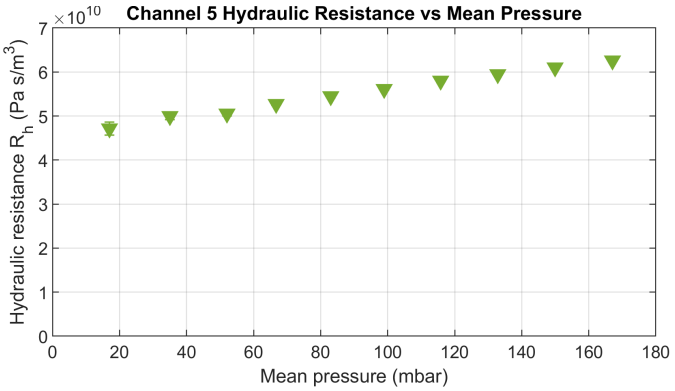

(d) Channel 5

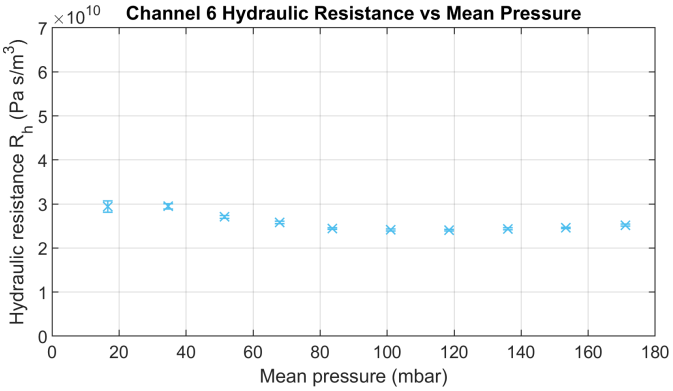

(e) Channel 6

Figure G.36: Hydraulic resistance R_h as a function of mean pressure for the additional tested channels. The plots show the channel-specific resistance trends after baseline correction. A decreasing hydraulic resistance with increasing mean pressure indicates an increase in effective channel diameter, while an increasing trend suggests that other effects, such as local narrowing, may dominate.

Appendix H. Diameter vs mean pressure graphs

Figure H.37 shows the effective diameter as a function of mean pressure for the individual tested channels. Channels 1–3 correspond to the E_- configuration (exp10), while channels 4–6 correspond to the E_+ configuration (exp20). The E_- channels generally show a stronger increase in effective diameter with increasing mean pressure, although the magnitude differs between channels. For the E_+ channels, the diameter change is smaller and more gradual. Channels 5 and 6 show either a decrease or an almost constant effective diameter with increasing mean pressure, which may indicate local narrowing of the channel.

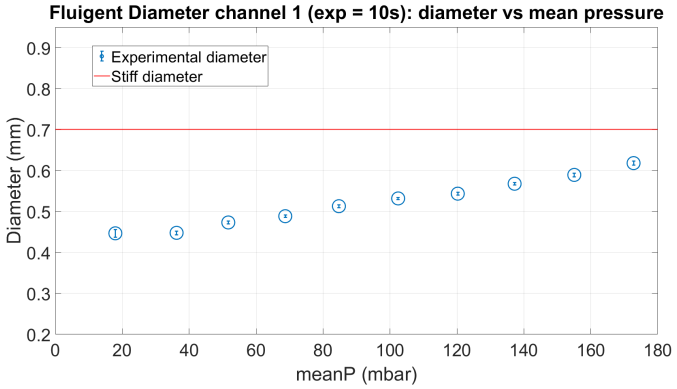

(a) Channel 1, E_- configuration

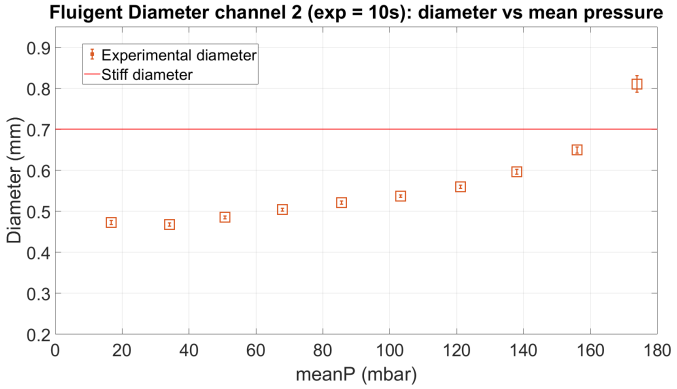

(b) Channel 2, E_- configuration

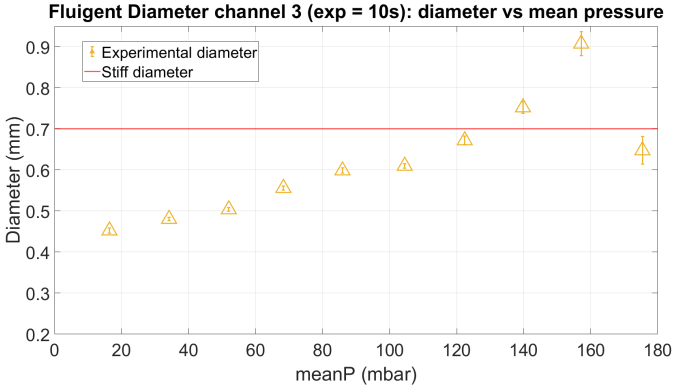

(c) Channel 3, E_- configuration

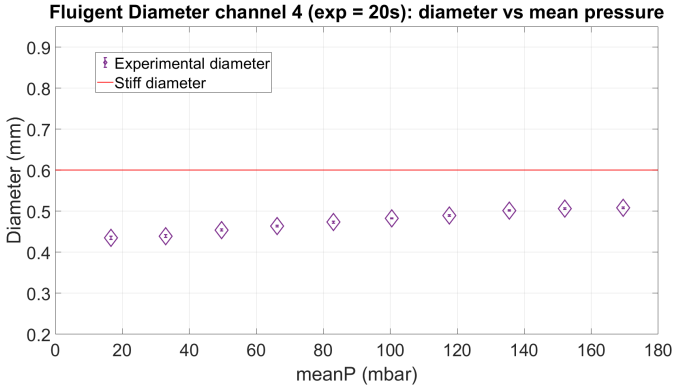

(d) Channel 4, E_+ configuration

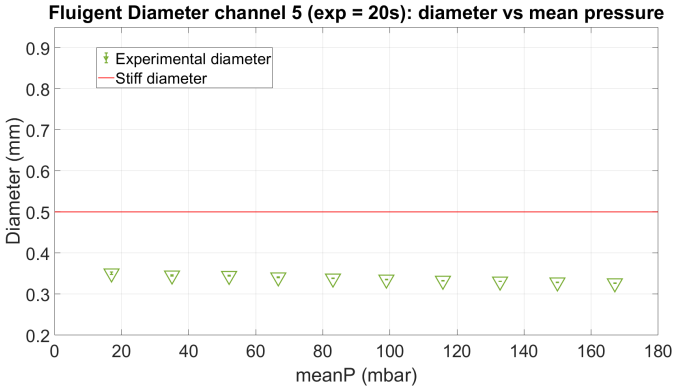

(e) Channel 5, E_+ configuration

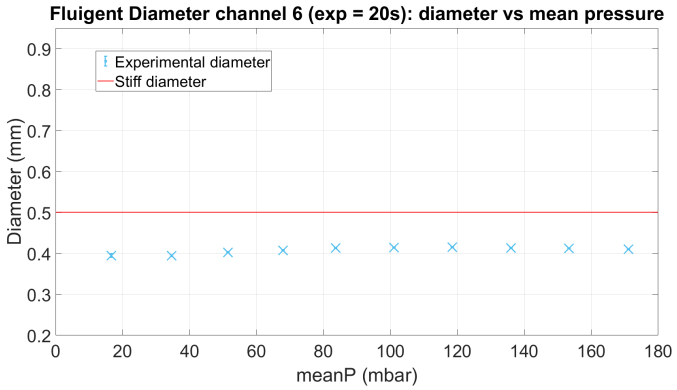

(f) Channel 6, E_+ configuration

Figure H.37: Effective diameter as a function of mean pressure for the individual tested channels. Channels 1–3 correspond to the E_- configuration with a printer exposure time of 10 s per layer, while channels 4–6 correspond to the E_+ configuration with a printer exposure time of 20 s per layer. The red line indicates the reference stiff diameter used for comparison.

Appendix I. Repeatability of relative diameter measurements

To evaluate whether the observed diameter-change trends were repeatable, additional runs of the same pressure-flow experiments were analysed. Figure I.38 shows the relative diameter change for repeated measurements. Figures I.38a and I.38b show the results for the E_- configuration, using channels 1–3 with a printer exposure time of 10 s per layer. Figures I.38c and I.38d compare the E_- configuration, based on the mean of channels 1–3, with the E_+ configuration.

The repeated measurements show that the general trend of increasing relative diameter with increasing mean pressure is present in several runs, especially for channels 1 and 3 in the E_- configuration. However, the exact magnitude of the diameter increase differs between runs and between channels. For example, channel 3 shows a strong increase in one run, while the trend is less consistent in another run. This difference may be caused by small variations in the pressure-flow response, sensor noise, remaining air bubbles, local narrowing of the channel, or uncertainty introduced by the baseline correction and diameter calculation. Because the diameter was calculated indirectly from hydraulic resistance, small changes in pressure drop or flow rate can strongly influence the extracted diameter.

The comparison between the E_- and E_+ configurations shows that the E_- configuration generally gives a larger relative diameter increase than the E_+ configuration. This supports the expectation that a lower Young's modulus leads to larger pressure-induced expansion. However, in the third run the error bars are large and overlap over a wide pressure range, which makes this comparison less conclusive. This large uncertainty is likely caused by the variability between the three E_- channels used to calculate the mean, combined with the sensitivity of the hydraulic-resistance-based diameter calculation.

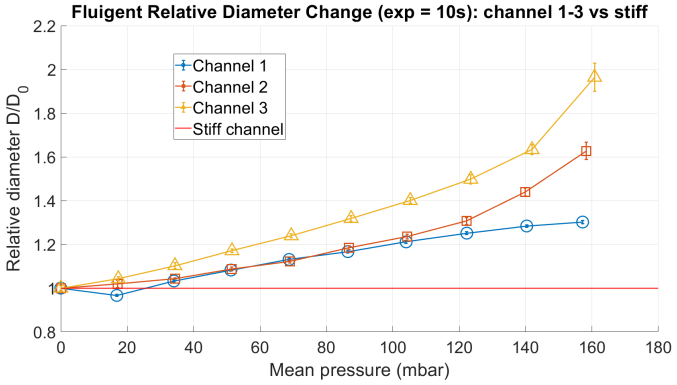

(a) E_- configuration, run 2

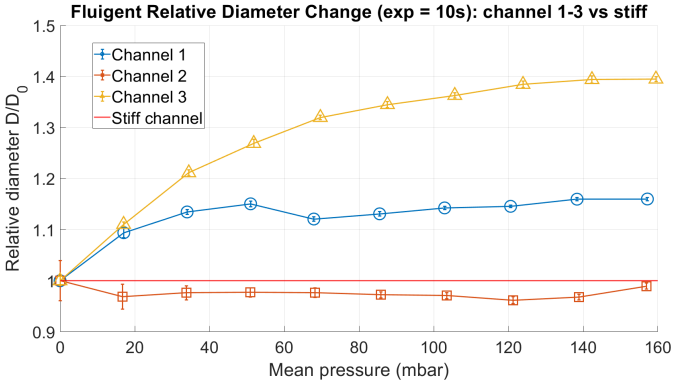

(b) E_- configuration, run 3

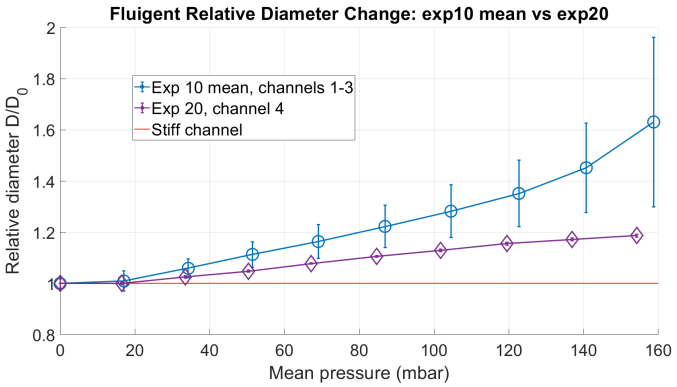

(c) E_- (exp10) versus E_+ (exp20) configuration, run 2

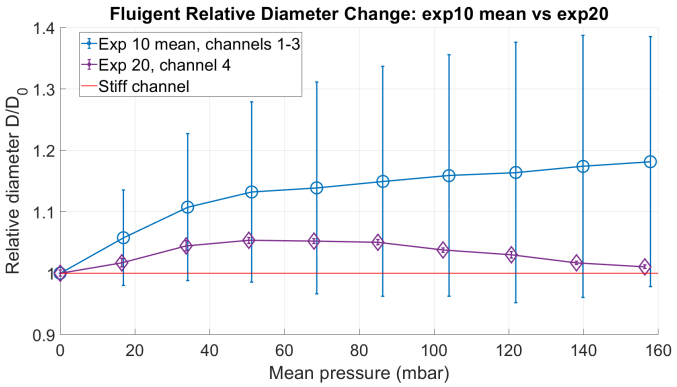

(d) E_- (exp10) versus E_+ (exp20) configuration, run 3

Figure I.38: Repeatability of the relative diameter change measurements. The upper two graphs (a and b) show repeated measurements for the E_- configuration, using channels 1–3. The lower two graphs (c and d) compare the E_- configuration, based on the mean of channels 1–3, with the E_+ configuration. The repeated runs show that the increasing relative diameter trend is present in several measurements, although the magnitude and uncertainty differ between runs.

Appendix J. MATLAB code

Appendix J.1. Pressure-flow data processing

```
clc
clear all
close all

d=readtable("C:\Users\lucas\Delft University of Technology\Paola Fanzio - Lucas Zijlstra\FLow Experiments\Fluigent\Fluigent_baseline_1.csv");
dc=readtable("C:\Users\lucas\Delft University of Technology\Paola Fanzio - Lucas Zijlstra\FLow Experiments\Fluigent\Fluigent_exp10_channel1_1.csv");

% Baseline data
time = d{:,1};
P1 = d{:,7};
P2 = d{:,9};
setP = d{:,3};
Q = d{:,4};

% Channel data
timeC = dc{:,1};
P1C = dc{:,7};
P2C = dc{:,9};
setPC = dc{:,3};
QC = dc{:,4};

%% plot example of the raw data

figure; % Create a new figure

plot(timeC, P1C, 'r', 'LineWidth', 4); % Plot P1 against Time, 'r' gives a red color

xlabel('Time [s]'); % Label for the x-axis
ylabel('P1 [mbar]'); % Label for the y-axis
title('P1 vs. Time'); % Title for the plot

grid on; % Add a grid for better visualization
set(gca,'FontSize',32)

%%

steady_window = 4;   % take last 4 seconds of each pressure step (stable and at steady-state)

% without the channel (baseline data)
change_idx = [1; find(diff(setP) ~= 0) + 1; length(setP)];

P1_mean = [];
P2_mean = [];
Q_mean = [];

P1_std = [];
P2_std = [];
Q_std = [];

for i = 1:length(change_idx)-1

    % Start and end row of this pressure step
    idx_start = change_idx(i);
    idx_end = change_idx(i+1)-1;

    % Time at the end of this pressure step
    step_end_time = time(idx_end);

    % Start time of steady-state window
    window_start_time = step_end_time - steady_window;

    % Select only the last 4 seconds of this pressure step
    idx = time >= window_start_time & time <= step_end_time;

    % Make sure to only select data inside this pressure step
    idx(1:idx_start-1) = false;
```

```
    idx(idx_end+1:end) = false;

    % Calculate mean values in steady-state window
    P1_mean(i,1) = mean(P1(idx));
    P2_mean(i,1) = mean(P2(idx));
    Q_mean(i,1) = mean(Q(idx));

    % Calculate standard deviation in steady-state window
    P1_std(i,1) = std(P1(idx));
    P2_std(i,1) = std(P2(idx));
    Q_std(i,1) = std(Q(idx));

end


% move P1, P2 and Q to zero
P1_mean_shifted = P1_mean - P1_mean(1);
P2_mean_shifted = P2_mean - P2_mean(1);
Q_mean_shifted = Q_mean - Q_mean(1);

deltaP_mean = P1_mean_shifted - P2_mean_shifted;

% Standard deviation of deltaP = P1 - P2
deltaP_std = sqrt(P1_std.^2 + P2_std.^2);


%% figure baseline

%figure;
%errorbar(Q_mean_shifted, deltaP_mean, deltaP_std, 'bo', 'MarkerFaceColor', 'b');
%hold on

p = polyfit(Q_mean_shifted, deltaP_mean, 2);

x_fit = linspace(min(Q_mean_shifted), max(Q_mean_shifted), 100);
y_fit = polyval(p, x_fit);

%plot(x_fit, y_fit, 'r-', 'LineWidth', 2);

%xlabel('Flow (ul/min)');
%ylabel('Pressure Drop (mbar)');
%legend('Baseline mean values', 'Polynomial fit');
%grid on;


% with the channel
change_idxC = [1; find(diff(setPC) ~= 0) + 1; length(setPC)];

P1C_mean = [];
P2C_mean = [];
QC_mean = [];

P1C_std = [];
P2C_std = [];
QC_std = [];

for i = 1:length(change_idxC)-1

    % Start and end row of this pressure step
    idx_start = change_idxC(i);
    idx_end = change_idxC(i+1)-1;

    % Time at the end of this pressure step
    step_end_time = timeC(idx_end);

    % Start time of steady-state window
    window_start_time = step_end_time - steady_window;

    % Select only the last 4 seconds of this pressure step
    idx = timeC >= window_start_time & timeC <= step_end_time;

```

```
    % Make sure we only select data inside this pressure step
    idx(1:idx_start-1) = false;
    idx(idx_end+1:end) = false;

    % Calculate mean values in steady-state window
    P1C_mean(i,1) = mean(P1C(idx));
    P2C_mean(i,1) = mean(P2C(idx));
    QC_mean(i,1) = mean(QC(idx));

    % Calculate standard deviation in steady-state window
    P1C_std(i,1) = std(P1C(idx));
    P2C_std(i,1) = std(P2C(idx));
    QC_std(i,1) = std(QC(idx));

end

% move P1 and P2 to zero
P1C_mean_shifted = P1C_mean - P1C_mean(1);
P2C_mean_shifted = P2C_mean - P2C_mean(1);
QC_mean_shifted = QC_mean - QC_mean(1);

deltaPC_mean = P1C_mean_shifted - P2C_mean_shifted;
meanP_mean = (P1C_mean_shifted + P2C_mean_shifted)./2;

% Standard deviation of deltaP and mean pressure
deltaPC_std = sqrt(P1C_std.^2 + P2C_std.^2);
meanP_std = sqrt(P1C_std.^2 + P2C_std.^2)./2;


%% figure channel, comparing baseline and channel data before correction

%figure;
%errorbar(Q_mean_shifted, deltaP_mean, deltaP_std, 'bo', 'MarkerFaceColor', 'b');
%hold on
%plot(x_fit, y_fit, 'r-', 'LineWidth', 2);
%errorbar(QC_mean_shifted, deltaPC_mean, deltaPC_std, 'go', 'MarkerFaceColor', 'g');

%xlabel('Flow (ul/min)');
%ylabel('Pressure Drop (mbar)');
%legend('Baseline mean values', 'Baseline polynomial fit', 'Channel mean values');
%grid on;


%% correction

correction = polyval(p, QC_mean_shifted);
deltaPC_corrected = deltaPC_mean - correction;

% Simple error estimate: using the standard deviation of the channel pressure drop
deltaPC_corrected_std = deltaPC_std;

%% Pressure-flow graph: mean and normalized values with standard deviations

% Raw/mean pressure drops before zero-shifting
deltaP_raw_mean = P1_mean - P2_mean;
deltaPC_raw_mean = P1C_mean - P2C_mean;

deltaP_raw_std = sqrt(P1_std.^2 + P2_std.^2);
deltaPC_raw_std = sqrt(P1C_std.^2 + P2C_std.^2);

%% Pressure-flow graph: normalized values with standard deviations

figure('Color','w','Position',[100 100 1200 900]);
hold on;

baseline_color = [0 0.4470 0.7410];
channel_color = [0.4660 0.6740 0.1880];
corrected_color = [0 0 0];

errorbarxy_local(Q_mean_shifted, deltaP_mean, Q_std, deltaP_std, ...
    'o', baseline_color, 'Baseline');
```

```
209
210 errorbarxy_local(QC_mean_shifted, deltaPC_mean, QC_std, deltaPC_std, ...
211     's', channel_color, 'Channel');
212
213 errorbarxy_local(QC_mean_shifted, deltaPC_corrected, QC_std, deltaPC_corrected_std, ...
214     'x', corrected_color, 'Corrected channel');
215
216 plot(x_fit, y_fit, '-', ...
217     'Color', [0.85 0 0.85], ...
218     'LineWidth', 2.5, ...
219     'DisplayName', 'Baseline fit');
220
221 xlabel('Flow rate (\muL/min)', 'FontSize', 32);
222 ylabel('Pressure drop (mbar)', 'FontSize', 32);
223 title('Normalized pressure-flow curve', 'FontSize', 34);
224
225 legend('Location','best','FontSize',26);
226 grid on;
227 box on;
228 set(gca,'FontSize',29,'LineWidth',1.8);
229
230 % Optional save command:
231 % exportgraphics(gcf, 'normalized_pressure_flow_curve.png', 'Resolution', 300);
232
233 %figure;
234 %errorbar(QC_mean_shifted, deltaPC_corrected, deltaPC_corrected_std, 'ko', 'MarkerFaceColor', 'k');
235 %xlabel('Flow (ul/min)');
236 %ylabel('Corrected Pressure Drop (mbar)');
237 %grid on;
238
239
240 %% Constants
241
242 viscosity = 0.001;       % Pa*s
243 diameter = 0.0007;       % m (0.6 mm)
244 Length = 0.0175;         % m
245
246
247 %% Channel diameter, compared with expected
248
249 % Remove zero or negative flow values to avoid division by zero
250 valid = QC_mean_shifted > 0;
251
252 flow_valid = QC_mean_shifted(valid);
253 flow_std_valid = QC_std(valid);
254
255 deltaPC_corrected_valid = deltaPC_corrected(valid);
256 deltaPC_corrected_std_valid = deltaPC_corrected_std(valid);
257
258 meanP_valid = meanP_mean(valid);
259 meanP_std_valid = meanP_std(valid);
260
261 % Convert pressure and flow to SI units
262 deltaP = deltaPC_corrected_valid * 100;              % mbar to Pa
263 deltaP_std_SI = deltaPC_corrected_std_valid * 100;   % mbar to Pa
264
265 flow = flow_valid * 1.6667*10^(-11);                 % ul/min to m^3/s
266 flow_std_SI = flow_std_valid * 1.6667*10^(-11);      % ul/min to m^3/s
267
268 % Hydraulic resistance
269 Rh_exp = deltaP ./ flow;
270
271 % Standard deviation of hydraulic resistance
272 % Rh = deltaP / Q
273 Rh_exp_std = abs(Rh_exp) .* sqrt((deltaP_std_SI ./ abs(deltaP)).^2 + ...
274                                  (flow_std_SI ./ abs(flow)).^2);
275
276 %% Channel hydraulic resistance as function of mean pressure
277
278 figure('Color','w','Position',[100 100 1200 900]);
279 hold on
```

```
channel1color = [0 0.4470 0.7410];          % blue channel 1
channel2color = [0.8500 0.3250 0.0980];     % orange channel 2
channel3color = [0.9290 0.6940 0.1250];     % yellow channel 3
channel4color = [0.4940 0.1840 0.5560];     % purple channel 4
channel5color = [0.4660 0.6740 0.1880];     % green channel 5
channel6color = [0.3010 0.7450 0.9330];     % light blue / cyan channel 6

Rh_color = channel1color;

% Marker per channel:
% channel 1 = o
% channel 2 = s
% channel 3 = ^
% channel 4 = d
% channel 5 = v
% channel 6 = x
Rh_marker = 'o';

% Vertical error bars for Rh
errorbar(meanP_valid, Rh_exp, Rh_exp_std, Rh_marker, ...
    'Color', Rh_color, ...
    'MarkerFaceColor', Rh_color, ...
    'MarkerSize', 24, ...
    'LineWidth', 2.6, ...
    'CapSize', 18, ...
    'DisplayName', 'Channel resistance');

% Horizontal error bars for mean pressure
for k = 1:numel(meanP_valid)
    line([meanP_valid(k)-meanP_std_valid(k), meanP_valid(k)+meanP_std_valid(k)], ...
         [Rh_exp(k), Rh_exp(k)], ...
         'Color', Rh_color, ...
         'LineWidth', 2.6, ...
         'HandleVisibility', 'off');
end

xlabel('Mean pressure (mbar)', 'FontSize', 32);
ylabel('Hydraulic resistance R_h (Pa s/m^3)', 'FontSize', 32);
title('Channel 1 Hydraulic Resistance vs Mean Pressure', 'FontSize', 32);

xlim([0,180])
ylim([0,20000000000])

%legend('Location','best','FontSize',32);
grid on;
box on;
set(gca,'FontSize',32,'LineWidth',1.8);

%% diameter

% Experimental diameter from Hagen-Poiseuille
diam_exp = ((128 * viscosity * Length) ./ (pi * Rh_exp)).^(1/4);

% Standard deviation of experimental diameter
% D is proportional to Rh^(-1/4), so relative error in D is 1/4 of relative error in Rh
diam_exp_std = abs(diam_exp) .* (1/4) .* abs(Rh_exp_std ./ Rh_exp);

%figure;
%errorbar(flow_valid, diam_exp*1000, diam_exp_std*1000, 'ko', 'MarkerFaceColor', 'k');
%xlabel('Flow (ul/min)');
%ylabel('Diameter (mm)');
%grid on;


%% Diameter as function of mean pressure

channel1_color = [0 0.4470 0.7410]; % blue channel 1
%channel1_color = [0.8500 0.3250 0.0980]; % orange channel 2
%channel1_color = [0.9290 0.6940 0.1250]; % yellow channel 3
%channel1_color = [0.4940 0.1840 0.5560]; % purple channel 4
```

```
%channel1_color = [0.4660 0.6740 0.1880]; % green channel 5
%channel1_color = [0.3010 0.7450 0.9330]; % light blue / cyan channel 6

% marker o , s , ^, d, v, x

figure;
errorbar(meanP_valid, diam_exp*1000, diam_exp_std*1000, 'o', 'Color', channel1_color, 'MarkerSize',
    24, 'LineWidth', 2);
hold on

E = 1.058 * 10^6;        % Young's modulus Pa exp10
%E = 1.245 * 10^6;        % Young's modulus Pa exp20
t = 0.25*10^(-3);        % wall thickness m

yline(diameter*1000, 'r-', 'LineWidth', 2);

xlabel('meanP (mbar)');
ylabel('Diameter (mm)');
title('Fluigent Diameter channel 4 (exp = 20s): diameter vs mean pressure')

xlim([0,180])
ylim([0.2,0.95])

legend('Experimental diameter', 'Stiff diameter');
grid on;
set(gca,'FontSize',32)


%% Reynolds number

figure('Units','centimeters','Position',[2 2 24 13],'Color','w');
hold on; box on;

rho = 1000;   % kg/m^3

Re = (4 * rho .* flow_valid .* 1.7e-11) ./ ...
     (pi * diameter .* viscosity);

% Standard deviation of Reynolds number
% Re is proportional to Q, so the relative error in Re is the same as the relative error in Q
Re_std = abs(Re) .* abs(flow_std_valid ./ flow_valid);

errorbar(flow_valid, Re, Re_std, 'ro-', ...
    'MarkerFaceColor', 'r', ...
    'MarkerSize', 14, ...
    'LineWidth', 3.0, ...
    'CapSize', 18);

xlabel('Flow rate (\muL/min)', 'FontSize', 32);
ylabel('Reynolds number', 'FontSize', 32);
title('Reynolds number vs flow rate', 'FontSize', 34);

set(gca, 'FontSize', 32, 'LineWidth', 1.5);
set(gca, 'Position', [0.14 0.17 0.80 0.72]);
grid on;

exportgraphics(gca, 'Reynolds_number.png', 'Resolution', 300);


function h = errorbarxy_local(x, y, xerr, yerr, markerStyle, color, displayName)

x = x(:);
y = y(:);
xerr = xerr(:);
yerr = yerr(:);

h = errorbar(x, y, yerr, yerr, markerStyle, ...
    'Color', color, ...
    'MarkerFaceColor', color, ...
    'MarkerSize', 24, ...
    'LineWidth', 2.6, ...
```

```
    'CapSize', 18, ...
    'DisplayName', displayName);

hold on;

for k = 1:length(x)
    line([x(k)-xerr(k), x(k)+xerr(k)], [y(k), y(k)], ...
        'Color', color, ...
        'LineWidth', 2.6, ...
        'HandleVisibility', 'off');
end

end
```

Listing 1: MATLAB code used for processing the pressure-flow data.

Appendix J.2. Relative diameter data processing - exp10 channels

```
clc
clear all
close all

%% Load baseline file

d = readtable("C:\Users\lucas\Delft University of Technology\Paola Fanzio - Lucas Zijlstra\FLow Experiments\Fluigent\Fluigent_baseline_1.csv");

%% Channel files

channel_files = {
    "C:\Users\lucas\Delft University of Technology\Paola Fanzio - Lucas Zijlstra\FLow Experiments\Fluigent\Fluigent_exp10_channel1_1.csv"
    "C:\Users\lucas\Delft University of Technology\Paola Fanzio - Lucas Zijlstra\FLow Experiments\Fluigent\Fluigent_exp10_channel2_1.csv"
    "C:\Users\lucas\Delft University of Technology\Paola Fanzio - Lucas Zijlstra\FLow Experiments\Fluigent\Fluigent_exp10_channel3_1.csv"
};

channel_names = {
    'Channel 1'
    'Channel 2'
    'Channel 3'
};

%% Baseline data

time = d{:,1};
P1 = d{:,7};
P2 = d{:,9};
setP = d{:,3};
Q = d{:,4};

steady_window = 4;   % take last 4 seconds of each pressure step (stable and at steady-state)

%% Constants

viscosity = 0.001;        % Pa*s
diameter = 0.0006;        % m (0.6 mm), reference diameter D0
Length = 0.0175;          % m

%% Without the channel, baseline data

change_idx = [1; find(diff(setP) ~= 0) + 1; length(setP)];

P1_mean = [];
P2_mean = [];
Q_mean = [];

P1_std = [];
P2_std = [];
Q_std = [];

for i = 1:length(change_idx)-1

    % Start and end row of this pressure step
    idx_start = change_idx(i);
    idx_end = change_idx(i+1)-1;

    % Time at the end of this pressure step
    step_end_time = time(idx_end);

    % Start time of steady-state window
    window_start_time = step_end_time - steady_window;

    % Select only the last 4 seconds of this pressure step
    idx = time >= window_start_time & time <= step_end_time;

    % Make sure to only select data inside this pressure step
```

```
    idx(1:idx_start-1) = false;
    idx(idx_end+1:end) = false;

    % Calculate mean values in steady-state window
    P1_mean(i,1) = mean(P1(idx));
    P2_mean(i,1) = mean(P2(idx));
    Q_mean(i,1) = mean(Q(idx));

    % Calculate standard deviation in steady-state window
    P1_std(i,1) = std(P1(idx));
    P2_std(i,1) = std(P2(idx));
    Q_std(i,1) = std(Q(idx));

end

%% Move P1, P2 and Q to zero

P1_mean_shifted = P1_mean - P1_mean(1);
P2_mean_shifted = P2_mean - P2_mean(1);
Q_mean_shifted = Q_mean - Q_mean(1);

deltaP_mean = P1_mean_shifted - P2_mean_shifted;

% Standard deviation of deltaP = P1 - P2
deltaP_std = sqrt(P1_std.^2 + P2_std.^2);

%% Baseline polynomial fit

p = polyfit(Q_mean_shifted, deltaP_mean, 2);

x_fit = linspace(min(Q_mean_shifted), max(Q_mean_shifted), 100);
y_fit = polyval(p, x_fit);

%% Store results for the 3 channels

meanP_all = cell(3,1);
relativeD_all = cell(3,1);
relativeD_std_all = cell(3,1);

max_meanP = 0;

%% Process all 3 channels

for c = 1:3

    dc = readtable(channel_files{c});

    %% Channel data

    timeC = dc{:,1};
    P1C = dc{:,7};
    P2C = dc{:,9};
    setPC = dc{:,3};
    QC = dc{:,4};

    %% With the channel

    change_idxC = [1; find(diff(setPC) ~= 0) + 1; length(setPC)];

    P1C_mean = [];
    P2C_mean = [];
    QC_mean = [];

    P1C_std = [];
    P2C_std = [];
    QC_std = [];

    for i = 1:length(change_idxC)-1

        % Start and end row of this pressure step
        idx_start = change_idxC(i);
```

```
        idx_end = change_idxC(i+1)-1;

        % Time at the end of this pressure step
        step_end_time = timeC(idx_end);

        % Start time of steady-state window
        window_start_time = step_end_time - steady_window;

        % Select only the last 4 seconds of this pressure step
        idx = timeC >= window_start_time & timeC <= step_end_time;

        % Make sure we only select data inside this pressure step
        idx(1:idx_start-1) = false;
        idx(idx_end+1:end) = false;

        % Calculate mean values in steady-state window
        P1C_mean(i,1) = mean(P1C(idx));
        P2C_mean(i,1) = mean(P2C(idx));
        QC_mean(i,1) = mean(QC(idx));

        % Calculate standard deviation in steady-state window
        P1C_std(i,1) = std(P1C(idx));
        P2C_std(i,1) = std(P2C(idx));
        QC_std(i,1) = std(QC(idx));

    end

    %% Move P1, P2 and Q to zero

    P1C_mean_shifted = P1C_mean - P1C_mean(1);
    P2C_mean_shifted = P2C_mean - P2C_mean(1);
    QC_mean_shifted = QC_mean - QC_mean(1);

    deltaPC_mean = P1C_mean_shifted - P2C_mean_shifted;
    meanP_mean = (P1C_mean_shifted + P2C_mean_shifted)./2;

    % Standard deviation of deltaP and mean pressure
    deltaPC_std = sqrt(P1C_std.^2 + P2C_std.^2);
    meanP_std = sqrt(P1C_std.^2 + P2C_std.^2)./2;

    %% Correction

    correction = polyval(p, QC_mean_shifted);
    deltaPC_corrected = deltaPC_mean - correction;

    % Simple error estimate: using the standard deviation of the channel pressure drop
    deltaPC_corrected_std = deltaPC_std;

    %% Channel diameter

    % Remove zero or negative flow values to avoid division by zero
    % Also remove negative corrected pressure drop values to avoid complex diameters
    valid = QC_mean_shifted > 0 & deltaPC_corrected > 0;

    flow_valid = QC_mean_shifted(valid);
    flow_std_valid = QC_std(valid);

    deltaPC_corrected_valid = deltaPC_corrected(valid);
    deltaPC_corrected_std_valid = deltaPC_corrected_std(valid);

    meanP_valid = meanP_mean(valid);
    meanP_std_valid = meanP_std(valid);

    % Convert pressure and flow to SI units
    deltaP = deltaPC_corrected_valid * 100;              % mbar to Pa
    deltaP_std_SI = deltaPC_corrected_std_valid * 100;   % mbar to Pa

    flow = flow_valid * 1.6667*10^(-11);                 % ul/min to m^3/s
    flow_std_SI = flow_std_valid * 1.6667*10^(-11);      % ul/min to m^3/s

    % Hydraulic resistance
```

```
    Rh_exp = deltaP ./ flow;

    % Standard deviation of hydraulic resistance
    % Rh = deltaP / Q
    Rh_exp_std = abs(Rh_exp) .* sqrt((deltaP_std_SI ./ abs(deltaP)).^2 + ...
                                     (flow_std_SI ./ abs(flow)).^2);

    % Experimental diameter from Hagen-Poiseuille
    diam_exp = ((128 * viscosity * Length) ./ (pi * Rh_exp)).^(1/4);

    % Standard deviation of experimental diameter
    % D is proportional to Rh^(-1/4), so relative error in D is 1/4 of relative error in Rh
    diam_exp_std = abs(diam_exp) .* (1/4) .* abs(Rh_exp_std ./ Rh_exp);

    %% Relative diameter D/D0

    % Use the first valid diameter as the reference diameter for this channel
    % This means the first plotted point becomes D/D0 = 1 at meanP = 0
    D0_channel = diam_exp(1);

    relativeD = diam_exp ./ D0_channel;
    relativeD_std = diam_exp_std ./ D0_channel;

    % Shift mean pressure so the first valid point starts at meanP = 0
    meanP_plot = meanP_valid - meanP_valid(1);

    relativeD_plot = relativeD;
    relativeD_std_plot = relativeD_std;

    %% Store data for final plot

    meanP_all{c} = meanP_plot;
    relativeD_all{c} = relativeD_plot;
    relativeD_std_all{c} = relativeD_std_plot;

    max_meanP = max(max_meanP, max(meanP_plot));

end

%% Relative diameter plot

figure;
hold on

errorbar(meanP_all{1}, relativeD_all{1}, relativeD_std_all{1}, 'o-', 'LineWidth', 1.5, 'MarkerSize',
    22);
errorbar(meanP_all{2}, relativeD_all{2}, relativeD_std_all{2}, 's-', 'LineWidth', 1.5, 'MarkerSize',
    22);
errorbar(meanP_all{3}, relativeD_all{3}, relativeD_std_all{3}, '^-', 'LineWidth', 1.5, 'MarkerSize',
    22);

yline(1, 'r-', 'LineWidth', 2);

xlabel('Mean pressure (mbar)');
ylabel('Relative diameter D/D_0');
title('Fluigent Relative Diameter Change (exp = 10s): channel 1-3 vs stiff')

legend(channel_names{1}, channel_names{2}, channel_names{3}, ...
       'Stiff channel', ...
       'Location', 'best');
lgd.FontSize = 24;

grid on;
set(gca,'FontSize',24)
```

Listing 2: MATLAB code used for processing the relative diameter of the exp10 channels data.

Appendix J.3. Tensile test data processing

```
% Stress strain (3 repeats) + Young's modulus for each repeat
% Exposure time: 10 s
% For TA DMA Q800 "Stress/Strain" export (UTF-16LE, tab-delimited)

clear; clc;

%% -------- Fixed settings --------
skipFirstN = 1;
fitEndFrac = 0.15;
% --------------------------------

files = {
    "Tensile_10_uv5w.txt"
    "Tensile_10_uv5w_2.txt"
    "Tensile_10_uv5w_3.txt"
};

sampleNames = {
    "Specimen 1"
    "Specimen 2"
    "Specimen 3"
};

% Check files exist
for i = 1:numel(files)
    if ~isfile(files{i})
        error("File not found: %s. Put all 3 .txt files in the current folder.", files{i});
    end
end

% Store results
E_MPa = nan(numel(files),1);
E_Pa  = nan(numel(files),1);
R2    = nan(numel(files),1);
fitInfo = strings(numel(files),1);

% For plotting
allStrainPct = cell(numel(files),1);
allStressMPa = cell(numel(files),1);
fitLineXPct  = cell(numel(files),1);
fitLineYMPa  = cell(numel(files),1);

%% Process each file
for i = 1:numel(files)
    [stress_MPa, strain_pct] = readDMAStressStrain(files{i});

    % Clean
    valid = isfinite(strain_pct) & isfinite(stress_MPa);
    strain_pct = strain_pct(valid);
    stress_MPa = stress_MPa(valid);

    % Sort by strain
    [strain_pct, sidx] = sort(strain_pct);
    stress_MPa = stress_MPa(sidx);

    % Keep nonnegative strain
    keep = strain_pct >= 0;
    strain_pct = strain_pct(keep);
    stress_MPa = stress_MPa(keep);

    allStrainPct{i} = strain_pct;
    allStressMPa{i} = stress_MPa;

    % Fit region
    maxStrainPct = max(strain_pct);
    strainEndPct = fitEndFrac * maxStrainPct;

    startIdx = min(max(skipFirstN + 1, 1), numel(strain_pct));
    idxFit = ((1:numel(strain_pct))' >= startIdx) & (strain_pct <= strainEndPct);

```

```
    if nnz(idxFit) < 10
        warning("Too few points in fit region for %s. Expanding to first 50 points after skipFirstN.",
             files{i});
        idxFit = false(size(strain_pct));
        i0 = startIdx;
        i1 = min(i0 + 49, numel(strain_pct));
        idxFit(i0:i1) = true;
    end

    x_pct = strain_pct(idxFit);
    y_MPa = stress_MPa(idxFit);

    % Convert to dimensionless strain for modulus
    x = x_pct / 100;

    % Linear fit: stress = E*strain + b
    p = polyfit(x, y_MPa, 1);
    E_MPa(i) = p(1);
    E_Pa(i)  = p(1) * 1e6;

    % R^2
    yhat = polyval(p, x);
    SSres = sum((y_MPa - yhat).^2);
    SStot = sum((y_MPa - mean(y_MPa)).^2);
    R2(i) = 1 - SSres/SStot;

    fitInfo(i) = sprintf("E = %.3f MPa, R^2 = %.4f", E_MPa(i), R2(i));

    % Fit line for plotting, only over fit window
    xx_pct = linspace(min(x_pct), max(x_pct), 50);
    xx = xx_pct / 100;
    yy = polyval(p, xx);

    fitLineXPct{i} = xx_pct;
    fitLineYMPa{i} = yy;
end

%% Mean + Std
E_mean_MPa = mean(E_MPa, 'omitnan');
E_std_MPa  = std(E_MPa, 'omitnan');

%% Figure 1: all  s t r e s s strain  curves
figure('Units','centimeters','Position',[2 2 24 13],'Color','w');
hold on; box on;

for i = 1:numel(files)
    plot(allStrainPct{i}, allStressMPa{i}, 'LineWidth', 3.0);
end

xlabel('Strain␣(%)', 'FontSize', 27);
ylabel('Stress␣(MPa)', 'FontSize', 27);
legend(sampleNames, 'Interpreter','none', 'Location','best', 'FontSize', 21);
title(' S t r e s s strain ␣curves␣(10s␣+␣5␣min␣water)', 'FontSize', 23);

set(gca, 'FontSize', 25, 'LineWidth', 1.3);
set(gca, 'Position', [0.12 0.16 0.82 0.72]);
set(gca, 'LooseInset', get(gca, 'TightInset'));
grid on;

exportgraphics(gca, 'Tensile_10s_5minwater_curves.png', 'Resolution', 300);

%% Figure 2: all curves + fit segments
figure('Units','centimeters','Position',[2 2 24 13],'Color','w');
hold on; box on;

hCurve = gobjects(numel(files),1);
hFit   = gobjects(numel(files),1);

for i = 1:numel(files)
    hCurve(i) = plot(allStrainPct{i}, allStressMPa{i}, 'LineWidth', 3.2);
    hFit(i)   = plot(fitLineXPct{i}, fitLineYMPa{i}, '--', 'LineWidth', 4.0);
```

```
end

xlabel('Strain (%)', 'FontSize', 30);
ylabel('Stress (MPa)', 'FontSize', 30);
title(sprintf(" S t r e s s strain  with linear fits (10s + 5 min water)"), 'FontSize', 29);

% Cleaner legend: specimen entries only
legTxt = strings(numel(files),1);
for i = 1:numel(files)
    legTxt(i) = sprintf("%s", sampleNames{i});
end

legend(hCurve, legTxt, 'Interpreter','none', 'Location','best', 'FontSize', 25);
legend(hCurve, legTxt, 'Interpreter','none', 'Location','best', 'FontSize', 25);

set(gca, 'FontSize', 31, 'LineWidth', 1.5);
set(gca, 'Position', [0.13 0.17 0.80 0.70]);
set(gca, 'LooseInset', get(gca, 'TightInset'));
grid on;

exportgraphics(gca, 'Tensile_10s_5minwater.png', 'Resolution', 300);

%% Print summary
fprintf("\nYoung's modulus results (10s & 5 min in water):\n");
for i = 1:numel(files)
    fprintf("  %s: E = %.6f MPa (%.6e Pa), R^2 = %.6f\n", sampleNames{i}, E_MPa(i), E_Pa(i), R2(i));
end
fprintf("\nMean E = %.6f MPa, Std E = %.6f MPa (n=%d)\n", E_mean_MPa, E_std_MPa, numel(files));

%% -------------- Local function --------------
function [stress_MPa, strain_pct] = readDMAStressStrain(file)
    % Reads TA DMA Q800 Stress/Strain export:
    % Nsig=12 with Sig7 = Stress (MPa), Sig8 = Strain (%)
    % Data starts after a line exactly "StartOfData"

    fid = fopen(file, 'r', 'n', 'UTF-16LE');
    if fid < 0
        error("Could not open file: %s", file);
    end

    % Find "StartOfData"
    startFound = false;
    while ~feof(fid)
        line = fgetl(fid);
        if ischar(line) && strcmp(strtrim(line), 'StartOfData')
            startFound = true;
            break;
        end
    end

    if ~startFound
        fclose(fid);
        error("StartOfData not found in %s. Encoding/file format may differ.", file);
    end

    % Read numeric block: 12 columns, tab-delimited
    fmt = repmat('%f', 1, 12);
    data = textscan(fid, fmt, 'Delimiter', '\t', 'CollectOutput', true);
    fclose(fid);

    M = data{1};  % Nx12
    if size(M,2) < 8
        error("Parsed data in %s has fewer than 8 columns; cannot extract Stress (col 7) and Strain (
            col 8).", file);
    end

    stress_MPa = M(:,7);
    strain_pct = M(:,8);
end
```

Listing 3: MATLAB code used for processing the tensile test data.

Appendix J.4. Accuracy test data processing

```
clear; clc; close all

file = "Datapoints.xlsx";
C = readcell(file);

toNum = @(x) local_toNum(x);

% Find section starts
sectionRows = [];
nomDiam = [];

for r = 1:size(C,1)
    if ischar(C{r,1}) || isstring(C{r,1})
        s = string(C{r,1});
        if contains(lower(s), "mm diameter")
            sectionRows(end+1) = r;
            tok = regexp(s, "([\d\.]+)", "tokens", "once");
            nomDiam(end+1) = str2double(tok{1});
        end
    end
end

% Long-format vectors for plotting
W_vals = []; W_group = [];
L_vals = []; L_group = [];
T_vals = []; T_group = [];

for k = 1:numel(sectionRows)
    r0 = sectionRows(k);
    r1 = size(C,1);

    if k < numel(sectionRows)
        r1 = sectionRows(k+1) - 1;
    end

    cadW = toNum(C{r0,4});
    cadL = toNum(C{r0,8});
    cadT = toNum(C{r0,11});

    if cadW > 10, cadW = cadW/1000; end
    if cadL > 10, cadL = cadL/1000; end
    if cadT > 10, cadT = cadT/1000; end

    for r = r0+1:r1
        ch = toNum(C{r,3});

        if isnan(ch)
            continue;
        end

        w = [toNum(C{r,4}),  toNum(C{r,5}),  toNum(C{r,6})];
        l = [toNum(C{r,8}),  toNum(C{r,9})];
        t = [toNum(C{r,11}), toNum(C{r,12})];

        w(w > 10) = w(w > 10)/1000;
        l(l > 10) = l(l > 10)/1000;
        t(t > 10) = t(t > 10)/1000;

        w(w > 2*cadW) = NaN;
        l(l > 2*cadL) = NaN;
        t(t > 2*cadT) = NaN;

        w = w(~isnan(w));
        l = l(~isnan(l));
        t = t(~isnan(t));

        W_vals  = [W_vals;  w(:)];
        W_group = [W_group; repmat(nomDiam(k), numel(w), 1)];

        L_vals  = [L_vals;  l(:)];
```

```
        L_group = [L_group; repmat(nomDiam(k), numel(l), 1)];

        T_vals  = [T_vals;  t(:)];
        T_group = [T_group; repmat(nomDiam(k), numel(t), 1)];
    end
end


% Plot (3 separate figures)
diameters = [0.7 1.0 2.0];
xpos = 1:numel(diameters);

% ============================================================
% CORRECT CAD VALUES
% ============================================================
CAD_L = [0.7 1.0 2.0];
CAD_W = [1.2 1.5 2.5];
CAD_T = [0.25 0.25 0.25];

% ============================================================
% SHARED Y-AXIS LIMITS AND TICKS FOR ALL 3 FIGURES
% ============================================================
allY = [W_vals(:); L_vals(:); T_vals(:); CAD_W(:); CAD_L(:); CAD_T(:)];
allY = allY(~isnan(allY));

tickStep = 0.25;
ymin = 0;
ymax = ceil(max(allY)/tickStep)*tickStep;

sharedYLim   = [ymin ymax];
sharedYTicks = ymin:tickStep:ymax;

% ============================================================
% -------- Figure 1: Width --------
% ============================================================
figure('Position',[100 100 900 450]);
hold on; box on;

makeBoxOnly(W_group, W_vals, diameters);
plotCADLinesLeft(CAD_W, xpos);

xlim([0.5 numel(diameters)+0.5]);
ylim(sharedYLim);
yticks(sharedYTicks);

title("Width", 'FontSize', 34);
ylabel("Width (mm)", 'FontSize', 32);
xlabel("Nominal lumen diameter (mm)", 'FontSize', 32);
set(gca,'XTick',xpos,'XTickLabel',string(diameters), ...
    'FontSize',29, 'LineWidth',1.0);

addLegendLikeExample();

% ============================================================
% -------- Figure 2: Lumen diameter --------
% ============================================================
figure('Position',[100 100 900 450]);
hold on; box on;

makeBoxOnly(L_group, L_vals, diameters);
plotCADLinesLeft(CAD_L, xpos);

xlim([0.5 numel(diameters)+0.5]);
ylim(sharedYLim);
yticks(sharedYTicks);

title("Lumen diameter", 'FontSize', 34);
ylabel("Lumen diameter (mm)", 'FontSize', 32);
xlabel("Nominal lumen diameter (mm)", 'FontSize', 32);
set(gca,'XTick',xpos,'XTickLabel',string(diameters), ...
    'FontSize',29, 'LineWidth',1.0);
```

```
142
143 addLegendLikeExample();
144
145 % ============================================================
146 % -------- Figure 3: Wall thickness --------
147 % ============================================================
148 figure('Position',[100 100 900 450]);
149 hold on; box on;
150
151 makeBoxOnly(T_group, T_vals, diameters);
152 plotCADLinesLeft(CAD_T, xpos);
153
154 xlim([0.5 numel(diameters)+0.5]);
155 ylim([0 0.5]);
156 yticks(0:0.05:0.5);
157
158 title("Wall thickness", 'FontSize', 34);
159 ylabel("Wall thickness (mm)", 'FontSize', 32);
160 xlabel("Nominal lumen diameter (mm)", 'FontSize', 32);
161 set(gca,'XTick',xpos,'XTickLabel',string(diameters), ...
162     'FontSize',29, 'LineWidth',1.0);
163
164 addLegendLikeExample();
165
166 % ---------------- Local functions ----------------
167
168 function v = local_toNum(x)
169     if isempty(x) || (ischar(x) && isempty(strtrim(x))) || (isstring(x) && strlength(x)==0)
170         v = NaN; return;
171     end
172     if isnumeric(x)
173         v = double(x); return;
174     end
175     if isstring(x) || ischar(x)
176         s = string(x);
177         s = strtrim(s);
178         s = replace(s, ",", ".");
179         v = str2double(s);
180         return;
181     end
182     v = NaN;
183 end
184
185 function makeBoxOnly(groupVals, dataVals, diameters)
186     xpos = 1:numel(diameters);
187
188     % Map nominal diameter values to x positions
189     g = zeros(size(groupVals));
190     for i = 1:numel(diameters)
191         g(groupVals == diameters(i)) = xpos(i);
192     end
193
194     % Boxplot
195     boxplot(dataVals, g, 'Symbol','', 'Colors','b', 'Widths',0.4);
196
197     % Styling
198     set(findobj(gca,'Tag','Box'),     'Color','b',           'LineWidth',1.2);
199     set(findobj(gca,'Tag','Median'),  'Color','r',           'LineWidth',1.5);
200     set(findobj(gca,'Tag','Whisker'), 'Color',[0.4 0.4 0.4], 'LineStyle','--', 'LineWidth',1.0);
201     set(findobj(gca,'Tag','Cap'),     'Color',[0.4 0.4 0.4], 'LineWidth',1.0);
202
203     set(gca,'XTick',xpos,'XTickLabel',string(diameters), ...
204         'FontSize',29, 'LineWidth',1.0);
205
206     % Grid
207     grid on;
208     ax = gca;
209     ax.XGrid = 'off';
210     ax.YGrid = 'on';
211     ax.GridAlpha = 0.35;
212     ax.Layer = 'top';
```

```
end

function plotCADLinesLeft(cadVals, xpos)
    xLeft = 0.5;  % far left of axis
    for i = 1:numel(xpos)
        plot([xLeft xpos(i)+0.35], [cadVals(i) cadVals(i)], ...
            'k:', 'LineWidth', 2.2);
    end
end

function addLegendLikeExample()
    h1 = plot(nan, nan, 'k:', 'LineWidth',2.2);
    h2 = plot(nan, nan, 'r-', 'LineWidth',1.5);
    lgd = legend([h1 h2], {'CAD value','Median'}, 'Location','best');
    lgd.FontSize = 29;
end
```

Listing 4: MATLAB code used for processing the accuracy test data.